FORCING THE TIE-GCM MODEL WITH BIRKELAND CURRENTS FROM THE AMPERE MISSION

Doctoral thesis by
SANTIAGO MARSAL VINADÉ

OBSERVATORI DE L’EBRE (Roquetes), 2014

TESI DOCTORAL

Forcing the TIE-GCM Model with Birkeland Currents from the AMPERE Mission

Santiago Marsal Vinadé

Observatori de l'Ebre

Dept. Geofísica

Dirigida per: **Dr. Juan José Curto Subirats**

C. Claravall, 1-3
08022 Barcelona
Tel. 936 022 200
Fax 936 022 249
E-mail: info@url.edu
www.url.edu

Universitat Ramon Llull

Aquesta Tesi Doctoral ha estat defensada el dia ____ de _________________ de 2014

al Centre ____

de la Universitat Ramon Llull

davant el Tribunal format pels Doctors sotasignants, havent obtingut la qualificació:

President/a

____

Vocal

____

Vocal

____

Vocal

____

Secretari/ària

____

Doctorand/a

C.I.F. G: 59069740 Universitat Ramon Llull Fundació Privada. Rgtre. Fund. Generalitat de Catalunya núm. 472 (28-02-90)

C. Claravall, 1-3
08022 Barcelona
Tel. 936 022 200
Fax 936 022 249
E-mail: info@url.edu
www.url.edu

A l’Imma, la Marta i la Núria

Acknowledgments

I wish to thank the Ebre Observatory Institute for giving me the opportunity to carry out this doctoral thesis and the understanding for the time I have devoted to it. My thanks are extended to the sponsoring institutions, in particular: *Universitat Ramon Llull (URL), Consejo Superior de Investigaciones Científicas (CSIC), Departaments d'Economia i Coneixement, i de Territori i Sostenibilitat de la Generalitat de Catalunya*, *Servei Meteorològic de Catalunya (SMC), Agencia Estatal de Meteorología (AEMET), Instituto Geográfico Nacional (IGN)*, *Diputació de Tarragona, Ajuntaments de Roquetes i Tortosa,* and *Companyia de Jesús*.

I thank the *Agència de Gestió d'Ajuts Universitaris i de Recerca (AGAUR)* from the former *Departament d'Innovació, Universitats i Empresa (DIUE) de la Generalitat de Catalunya* for providing me with the grant for stays abroad (BE-DGR 2010), which allowed me a fruitful 5-month stay at the High Altitude Observatory of the National Center for Atmospheric Research (NCAR), in Boulder, CO, USA. I am also grateful to the several Spanish Research Projects in Antarctica, funded by the *Ministerio de Educación, Cultura y Deporte* (or equivalent), for allowing me to enjoy a contract of research in the Spanish Antarctic Station.

I sincerely thank the NCAR staff, and especially Dr. Art Richmond, to whom I am indebted, for his admirable knowledge on atmospheric sciences, his capability to transmit it in a clear manner, his work proposal to me, his huge patience, his availability anytime, and for all the good tips I received from him. I also thank Astrid Maute for helping me with the TIE-GCM code; Drs. B. Emery, Y. Zhang and W. Wang for fruitful discussions on the auroral specification; and Pete Schmidt and Ben Foster for the technical support provided during my stay.

I thank Dr. J. J. Curto for directing my thesis, for giving good advice and tips, and for providing me with fruitful contacts.

I thank Dr. J. Miquel Torta for believing in me anytime and for encouraging me to go ahead with my thesis after directing my *Diploma d'Estudis Avançats*. I'm also grateful to Òscar Cid, the computer scientist, who installed and adapted the TIE-GCM for parallel computing, and fixed the numerous upcoming problems (Òscar, I owe you a beer); also to Maria and M. José, who timely provided me with all the bibliography I needed; my past and present colleagues, most of them at Ebre Observatory, with whom I have collaborated in either way and at some extent have made this work to come true: Nia, Toni, M. Ibañez, Germán, D. Altadill, Fr. Alberca, Fr. Sanclement, Pere, Xavi, J. C. Riddick, ...

Vull agrair molt especialment als meus pares, Jaume i Berta, tot el suport i acompanyament que sempre m'han donat. Un altre cop al meu pare, que em va transmetre la virtut de la Curiositat. A la meva dona, l'Imma, sobretot, … no cal ni

començar. A les meves filles Marta i Núria, per existir. Als meus sogres, el Joan i la Josefina, per estar sempre al peu del canó i ser incansables; a la meva família: el meu germà Albert, els meus avis Joan i Maria, la Cristina, el Joan, la Montse, el Josep, l'Agnès, l'Antonieta, ... pels seus ànims i suport moral.

També als meus amics, per estar sempre allà: D. Arrazola, Ximo, Estanis, Beatriu, Àngels, Jordi, Núria, Josep M., ...

Finally, I thank Maria and Art for those walks in the Rockies during my stay at Boulder.

Thank you all very much. *Mil gràcies a tots.*

CONTENTS

Resum 1

Resumen 2

Abstract 3

List of Variables 5

List of Abbreviations 7

1. INTRODUCTION AND BACKGROUND **11**

1.1. THE SOLAR WIND AND THE MAGNETOSPHERE 11
1.2. THE IONOSPHERE 13
1.3. SPACE WEATHER, SPACE CLIMATE AND THEIR SOCIETAL IMPLICATIONS 16
1.4. MOTIVATION AND SCOPE OF THE PRESENT WORK 19
1.5. STATE OF THE ART 20

2. FUNDAMENTAL CONCEPTS **23**

2.1. FUNDAMENTALS OF EARTH’S MAGNETISM 23
2.2. MAGNETIC FIELD MODELS 25
2.3. FUNDAMENTAL EQUATIONS 27
2.4. THE IONOSPHERIC CURRENT SHEET APPROXIMATION 31
2.5. CONSIDERATIONS ABOUT THE GROUND MAGNETIC SIGNATURE OF CURRENTS FLOWING IN THE IONOSPHERE AND MAGNETOSPHERE 33

3. THE LARGE-SCALE SYSTEM OF FIELD-ALIGNED CURRENTS **37**

3.1. OVERVIEW 37
3.2. ENERGY AND MOMENTUM TRANSFER FROM THE SOLAR WIND TO THE UPPER ATMOSPHERE 42
3.3. THE AURORAL UPPER ATMOSPHERE IN CONNECTION WITH FIELD-ALIGNED CURRENTS 44

4. AMPERE AND TIE-GCM **47**

4.1. THE AMPERE MISSION 47
4.2. THE TIE-GCM 48
    4.2.1. THE CURRENT CONTINUITY EQUATION IN THE TIE-GCM 50
    4.2.2. THE STANDARD TIE-GCM 52
    4.2.3. CALCULATION OF GROUND MAGNETIC SIGNATURES 53

5. THE AMPERE-DRIVEN TIE-GCM 55

5.1. THE AMPERE INPUT 56
5.2. THE OPEN FIELD-LINE VERSION OF THE ELECTRODYNAMO EQUATION 58
5.3. THE AURORAL SPECIFICATION IN THE AMPERE-DRIVEN TIE-GCM 60

6. MODEL APPLICATION. RESULTS AND DISCUSSION 69

6.1. MODEL VALIDATION TOOLS 69
6.1.1. EVALUATING THE GENERAL PERFORMANCE 69
6.1.2. EVALUATING THE MODEL CONDUCTANCES 71
6.2. RESULTS 76
6.2.1. PREVIOUS REMARKS 76
6.2.2. MODELED ELECTRODYNAMIC VARIABLES 78
6.2.3. VALIDATION RESULTS 83
6.3. DISCUSSION 90

7. SUMMARY, CONCLUSIONS AND FUTURE GUIDELINES 99

7.1. SUMMARY AND CONCLUSIONS 99
7.2. FUTURE GUIDELINES 104

APPENDIX A 107

Flowcharts of the TIE-GCM electrodynamics

APPENDIX B 109

Physical constants

Conversion of energy units

APPENDIX C 111

Number flux, energy flux and mean energy of an accelerated Maxwellian distribution

APPENDIX D 117

Correction of fluxes and mean energy for conductivity purposes

APPENDIX E 119

World map of geomagnetic observatories used for validation purposes

REFERENCES 121

Unpublished Material 133

Resum

Donat que la nostra societat és cada cop més dependent de la tecnologia, i perquè la tecnologia és vulnerable als processos de l'alta atmosfera que tenen el seu origen en el Sol, la nostra mirada es dirigeix progressivament vers la comprensió dels mecanismes concrets que possibiliten la connexió Sol - Terra, tractant-se avui dia d'una disciplina on la recerca va clarament en augment. L'acoblament de l'alta atmosfera amb la magnetosfera és, doncs, important per tal d'entendre processos que afecten el nostre planeta a escala global. Aquesta darrera baula en la complexa cadena d'esdeveniments que comencen en la nostra estrella té com a principal destinatària la ionosfera d'altes latituds, on es dipositen quantitats considerables d'energia i moment del vent solar. El camp magnètic terrestre juga un paper clau en aquesta interacció, on els corrents elèctrics que circulen al llarg de les línies de camp magnètic, altament conductores, es poden assimilar als cables d'un circuit que es tanca a través de la càrrega elèctrica (en terminologia de circuits) que constitueix la ionosfera d'altes latituds. La missió satel·litària Active Magnetosphere and Planetary Electrodynamics Response Experiment *(AMPERE) ha proporcionat, per primera vegada, instantànies dels corrents alineats al camp amb una resolució espaial i temporal sense precedents, oferint així una oportunitat per alimentar un reconegut model físic de l'alta atmosfera de la Terra com el* National Center for Atmospheric Research Thermosphere-Ionosphere-Electrodynamics General Circulation Model *(NCAR TIE-GCM). En un primer pas, hem utilitzat les dades d'AMPERE en l'equació de continuïtat del corrent entre la magnetosfera i la ionosfera per tal de forçar l'electrodinàmica del TIE-GCM, i hem validat els resultats tot comparant l'output corresponent a les variacions magnètiques en superfície amb dades geomagnètiques d'observatoris a diferents latituds i per a diferents condicions geofísiques. En una segona fase, hem introduït conductivitats ionosfèriques compatibles amb sectors de corrents alineats ascendents elevats, corresponents a electrons que es desplomen com a resultat d'una acceleració descendent deguda a camps elèctrics paral·lels que s'acumulen al llarg de les línies de camp magnètic, tot fent ús de diferents models per a validar les nostres conductàncies de sortida. Els resultats mostren una millora general de la capacitat del model per explicar les variacions magnètiques observades, tot i que amb una major contribució arran de la nostra primera aproximació. Les distribucions de conductància obtingudes, d'altra banda, són prou consistents amb models independents que han intentat quantificar l'efecte ionitzant de partícules que precipiten sobre la ionosfera auroral. En conclusió, hem fet una contribució modesta, però tanmateix constructiva, a la modelització de l'alta atmosfera i la seva connexió amb l'entorn espacial; principalment perquè tenim entre mans un model físic, que en últim terme ha de servir per avaluar el nostre coneixement de la realitat, més que no pas per proveir un resultat purament funcional.*

Resumen

Dado que nuestra sociedad es cada vez más dependiente de la tecnología, y porque la tecnología es vulnerable a los procesos de la alta atmósfera que tienen su origen en el Sol, nuestra mirada se dirige progresivamente hacia la comprensión de los mecanismos precisos que posibilitan la conexión Sol - Tierra, tratándose hoy en día de una disciplina en claro avance en cuanto a investigación. El acoplamiento de la alta atmósfera con la magnetosfera es, pues, importante para la comprensión de procesos que afectan a nuestro planeta a escala global. Este último eslabón en la compleja cadena de sucesos que comienzan en nuestra estrella tiene como principal destinatario la ionosfera de altas latitudes, donde se depositan cantidades considerables de energía y momento del viento solar. El campo magnético terrestre juega un papel clave en esta interacción, donde las corrientes eléctricas que circulan a lo largo de las líneas de campo magnético, altamente conductoras, pueden asimilarse a los cables de un circuito que se cierra a través de la carga eléctrica (en terminología de circuitos) que constituye la ionosfera de altas latitudes. La misión satelital Active Magnetosphere and Planetary Electrodynamics Response Experiment *(AMPERE) ha proporcionado, por vez primera, instantáneas de las corrientes alineadas al campo con una resolución espacial y temporal sin precedentes, ofreciendo así una oportunidad para alimentar un reconocido modelo físico de la alta atmósfera de la Tierra como el* National Center for Atmospheric Research Thermosphere-Ionosphere-Electrodynamics General Circulation Model *(NCAR TIE-GCM). En un primer paso, hemos utilizado los datos de AMPERE en la ecuación de continuidad de corriente entre la magnetosfera y la ionosfera a fin de forzar la electrodinámica del TIE-GCM, validando los resultados a través de la comparación del output correspondiente a las variaciones magnéticas en superficie con datos geomagnéticos de observatorios a distintas latitudes y para diferentes condiciones geofísicas. En una segunda fase, hemos introducido conductividades ionosféricas compatibles con sectores de corrientes alineadas ascendentes elevadas, correspondientes a electrones que se desploman como resultado de una aceleración descendiente debida a campos eléctricos paralelos que se acumulan a lo largo de las líneas de campo magnético, haciendo uso de diferentes modelos para validar nuestras conductancias de salida. Los resultados muestran una mejora general de la capacidad del modelo para explicar las variaciones magnéticas observadas, aunque con una mayor contribución a raíz de nuestra primera aproximación. Las distribuciones de conductancia obtenidas, por otro lado, son razonablemente consistentes con modelos independientes que han intentado cuantificar el efecto ionizante de partículas que precipitan sobre la ionosfera auroral. En conclusión, hemos contribuido modesta, aunque constructivamente, a la modelización de la alta atmósfera y a su conexión con el entorno espacial; principalmente porque estamos tratando con un modelo físico, que en último término debe servir para evaluar nuestro conocimiento de la realidad, antes que proveer un resultado puramente funcional.*

Abstract

Because our society is ever more dependent on technology, and because technology is vulnerable to upper atmospheric processes having their origin in the Sun, our gaze is progressively turning towards the understanding of the exact mechanisms that enable the Sun-Earth connection, being today a matter of increasingly intensive research. Coupling of the upper atmosphere system with the magnetosphere is thus important for understanding processes that affect our planet in a global scale. This last link in the complex chain of events starting in our star has the high-latitude ionosphere as a main target, where considerable amounts of solar wind energy and momentum are deposited. The magnetic field of the Earth plays a key role in this interaction, with electric currents flowing along the highly conducting geomagnetic field lines that can be thought of as the wires in a circuit that is closed by the electrical load of the high-latitude ionosphere. The Active Magnetosphere and Planetary Electrodynamics Response Experiment (AMPERE) satellite mission has offered for the first time snapshots of the geomagnetic field-aligned currents with unprecedented space and time resolution, thus providing an opportunity to feed an acknowledged first-principles model of the Earth's upper atmosphere such as the National Center for Atmospheric Research Thermosphere-Ionosphere-Electrodynamics General Circulation Model (NCAR TIE-GCM). In a first step, we have made use of AMPERE data in the current continuity equation between the magnetosphere and the ionosphere to drive the TIE-GCM electrodynamics, and we have validated our results by comparing the output ground magnetic variations with geomagnetic observatory data at different latitudes and for different geophysical conditions. In a second stage, we have made ionospheric conductivities consistent with enhanced upward field-aligned current sectors corresponding to electrons plunging as a result of downward acceleration by parallel electric fields built up along the magnetic field lines, whereby we have used different models to validate our output conductances. Results show an overall improvement of the model ability to explain the observed magnetic variations, though with a greater contribution coming from our first approach. Our conductance distribution, on the other hand, is reasonably commensurate with independent models that have tried to quantify the ionizing effect of precipitating particles onto the auroral ionosphere. In conclusion, we have made a modest but constructive contribution to the modeling of the upper atmosphere and its connection with the space environment; especially because we are dealing with a physical model, which is ultimately meant to assess our knowledge of reality, rather than providing a purely functional result.

List of Variables

Note that we have omitted those instances of the same variable having different sub- (super-) scripts.

$\vec{\boldsymbol{A}}, a, b$	Dummy variables.
α	Characteristic energy of precipitating electrons [keV].
$\hat{\boldsymbol{b}}$	Unit vector in the magnetic field direction.
$\vec{\boldsymbol{B}}$	Magnetic flux density, here denoted as magnetic field [nT].
B	Magnitude of the magnetic field vector [nT].
$B_{X,Y,Z}$	Components of the interplanetary magnetic field [nT].
β	Ratio of the magnetic field strength at the ionosphere to plasma sheet bases.
c	Speed of light [m s^{-1}].
d_s	Maxwellian distribution function [m^{-6} s^{3}].
D	Magnetic declination [°].
e	Elementary charge [A s].
$\hat{\boldsymbol{e}}_{\boldsymbol{2}}$	Unit vector in the meridian plane.
$\bar{E}$	Mean energy of precipitating electrons [keV].
E	Kinetic energy of electrons [keV] when it has supscripts k, p, T; electric field component [V m^{-1}] when it has subscripts ϕ, λ, $\perp$.
$\vec{\boldsymbol{E}}$	Electric field [V m^{-1}].
ε_0	Permittivity of free space [A s V^{-1} m^{-1}].
f_s	Number flux density ([cm^{-2} s^{-1} keV^{-1}] when it is a function of energy; [m^{-5} s^{2}] when it is a function of velocity).
F	Electron flux [m^{-2} s^{-1}] when it has subscripts S, I, 0; geomagnetic field magnitude at the surface [nT] otherwise.
Φ	Electrostatic potential [V].
ϕ	Magnetic longitude [°].
φ	Angular coordinate [rad].
$\hat{\boldsymbol{\phi}}$	Unit vector towards magnetic east.
h	Height [m].
H	Horizontal component of the geomagnetic field [nT].
I	Magnetic inclination [°]; surface-integrated current [A] if it has subscripts.

J_r	Radial component of field-aligned currents [A m^{-2}].
$\vec{\boldsymbol{J}}$	Current density [A m^{-2}].
k	Boltzmann constant [J k^{-1}]; proportionality factor if it has superscripts [S m^{2} A^{-1}].
$\vec{\boldsymbol{K}}$	Height-integrated ionospheric current [A m^{-1}].
$\hat{\boldsymbol{\lambda}}$	Unit vector towards magnetic north.
λ	Magnetic latitude [°].
m_e	Electron mass [kg].
m_i	*i*-th component of model output [variable units; nT in our case].
$\overline{m}$	Mean of the model output [variable units; nT in our case].
μ_0	Permeability of free space [V s A^{-1} m^{-1}].
N	Number density [m^{-3}] when it has a subscript (e.g., N_S); total number of observations otherwise.
χ	Solar zenith angle [°].
o_i	*i*-th observation [variable units; nT in our case].
$\bar{o}$	Mean of the observations [variable units; nT in our case].
Ω	Solid angle [sr].
P	Performance parameter.
Q	Energy flux associated with electron precipitation [erg cm^{-2} s^{-1}].
q_J	Heat loss by Joule effect [W m^{-3}].
r	Radial distance [m].
$\hat{\boldsymbol{r}}$	Unit upward vector.
R	Reference radius [m].
R_E	Mean radius of the Earth [m].
ρ	Electric charge density [A s m^{-3}].
s	Geometric distance along the magnetic field line [m].
S	(with subscripts, e.g., S_v) Domains of integration in different spaces [variable units].
$\vec{\boldsymbol{S}}$	Poynting vector [W m^{-2}].
$\boldsymbol{\sigma}$	Electric conductivity tensor [S m^{-1}].
σ	Electric conductivity [S m^{-1}] when it has subscripts B, P, H; standard deviation [variable units; nT in our case] when it has subscripts o, m, om, r.
Σ	Electric conductance [S].

t	Time [s].
T	Temperature [K].
τ	Current potential [A].
θ	Angular coordinate [rad].
$\vec{\boldsymbol{u}}$	Neutral wind velocity [m s^{-1}].
v	Electron speed [m s^{-1}].
$\vec{\boldsymbol{v}}$	Electron velocity [m s^{-1}].
$\vec{\boldsymbol{v}}_{\boldsymbol{p}}$	Plasma velocity [m s^{-1}].
V	Potential difference between ionosphere and plasma sheet bases [V].
x, y	Dimensionless variables.
X, Y, Z	Geographic northward, eastward and downward components, respectively, of the geomagnetic field at the surface [nT].

List of Abbreviations

AACGM	Altitude Adjusted Corrected GeoMagnetic
AC	Alternating Current
AE	Auroral Electrojet
AE-C	Atmospheric Explorer-C
AFOSR	Air Force Office of Scientific Research
AMIE	Assimilative Mapping of Ionospheric Electrodynamics
AMP	AMPERE
AMPERE	Active Magnetosphere and Planetary Electrodynamics Response Experiment
CARISMA	Canadian Array for Real-time Investigations of Magnetic Activity
CM	Comprehensive Model
CME	Coronal Mass Ejection
CMIT	Coupled Magnetosphere Ionosphere Thermosphere
CMO	College
CPCP	Cross-Polar Cap Potential
DC	Direct Current

Ddyn	Disturbance dynamo
DP1, DP2	Disturbance Polar of the first/second type
DMSP	Defense Meteorological Satellite Program
e-m	Electromagnetic
eq.	Equation
EBR	Ebre
EUV	Extreme UltraViolet
FAC	Field-Aligned Current
FUV	Far UltraViolet
GCM	General Circulation Model
GCR	Galactic Cosmic Ray
GEM	Geospace Environment Modeling
GIC	Geomagnetically-Induced Current
GNSS	Global Navigation Satellite System
GSWM	Global Scale Wave Model
GUVI	Global UltraViolet Imager
HF	High Frequency
HP	Hemispheric Power
IAGA	International Association of Geomagnetism and Aeronomy
IGRF	International Geomagnetic Reference Field
IHFAC	Inter-Hemispheric Field-Aligned Current
IMAGE	International Monitor for Auroral Geomagnetic Effects
IMF	Interplanetary Magnetic Field
Iono.	Ionosphere
IRI	International Reference Ionosphere
IUGG	International Union of Geodesy and Geophysics
KRM	Kamide-Richmond-Matsushita
Lat.	Latitude
LEO	Low Earth Orbit
LFM	Lyon-Fedder-Mobarry
LIV	Livingston

M	*Marklund et al.* [1988]
MMA	Modified Magnetic Apex
MLT	Magnetic Local Time
NASA	National Aeronautics and Space Administration
NBZ	Northward B_Z
NCAR	National Center for Atmospheric Research
NH	Northern Hemisphere
NS	North-South
PCA	Polar Cap Absorption
POMME	POtsdam Magnetic Model of the Earth
QD	Quasi-Dipole
R	*Robinson et al.* [1987]
R1, R2	Region 1, Region 2
SC	Sudden Commencement
SH	Southern Hemisphere
SPE	Solar Proton Event
Sq	Solar quiet
SSC	Sudden Storm Commencement
Std	Standard
SuperDARN	Super Dual Auroral Radar Network
TEC	Total Electron Content
TIE-GCM	Thermosphere-Ionosphere-Electrodynamics General Circulation Model
TIMED	Thermosphere-Ionosphere-Mesosphere Energetics and Dynamics
TRO	Tromsø
UT	Universal Time
UV	UltraViolet
ZP	Zhang and Paxton

1. INTRODUCTION AND BACKGROUND

The aurora display is probably the most striking and oldest known phenomena that humankind has experienced in connection with the upper atmosphere processes. Beyond the mythology and beliefs of the coexisting cultures, they are known today to be manifestations of the electric processes and the conductive nature of our high-latitude gas envelope, revealing a close connection with the Earth's space environment and eventually with the Sun.

From a more scientific point of view, magnetic field measurements both at the Earth's surface and in space also provide an evidence of the electric phenomena occurring in the immediate vicinity of our planet. Superimposed onto the main magnetic field, which is dipolar in a first approximation and varies on timescales of centuries, there are a number of smaller scale features, both in the space and time domains. *Stewart* [1883] and *Schuster* [1889] for the first time, and prior to the discovery of the electron, attributed the observed daily magnetic variations recorded at the Earth's surface to dynamo action on the electrically conducting portion of the upper atmosphere, which we know today as the ionosphere. At high latitudes, the ionosphere provides a closure path for currents extending far out into the Earth's environment. It was Kristian Birkeland [*Birkeland,* 1908] who formally proposed currents guided by the Earth's main magnetic field connecting the space environment of our planet with the high-latitude upper atmosphere. In these zones, dynamo action of the ionospheric winds plays a secondary role in the generation of ground magnetic perturbations, being dominated by electric fields and currents penetrating from outer regions of space.

1.1. THE SOLAR WIND AND THE MAGNETOSPHERE

Plasma consisting primarily of H and He ions and electrons is continuously streaming out from the Sun at velocities of hundreds of kilometers per second, giving rise to the so-called solar wind. A small part of these charged particles, which travel in the interplanetary medium accompanied by the interplanetary magnetic field (IMF), eventually arrive at the Earth's orbit, where they interact with the terrestrial magnetic field. As a result of this interaction, the Chapman-Ferraro currents are created, originating a cavity where the magnetic field of the Earth is confined. This region of space, known as the magnetosphere, is bounded by the magnetopause, which effectively separates the IMF from the Earth's magnetic field (see Figure 1.1). The dipole-like nature of the geomagnetic field is thus changed and it is conferred a comet-like shape elongated in the anti-solar direction well beyond the lunar orbit, giving raise to the magnetotail. In the sunward direction, the magnetosphere extends between 6 and 10 Earth radii (R_E), decreasing with the solar wind pressure. The supersonic condition of the solar wind flow originates a shock in front of the magnetosphere designated as the terrestrial bow shock, where discontinuities in the solar wind parameters (e.g., velocity, plasma density and temperature) are observed. The region of space between the bow shock and the magnetopause is designated as the magnetosheath.

Besides the confinement of the Earth's magnetic field, the importance of the magnetosphere stems from its several particle populations; the radiation (or Van Allen) belts, the ring current and the plasma sheet are some examples, each of which being characterized by different locations, densities and temperatures, as well as by their origin, either solar or terrestrial. Due to the high conductivity of these plasma populations and/or to the existence of forces of diverse origin, several current systems are embedded in them: the Chapman-Ferraro and the ring current have already been mentioned; others are the cross-tail current, the plasma sheet boundary layer current, or the field-aligned current system connecting with the high-latitude ionosphere (Figure 1.1).

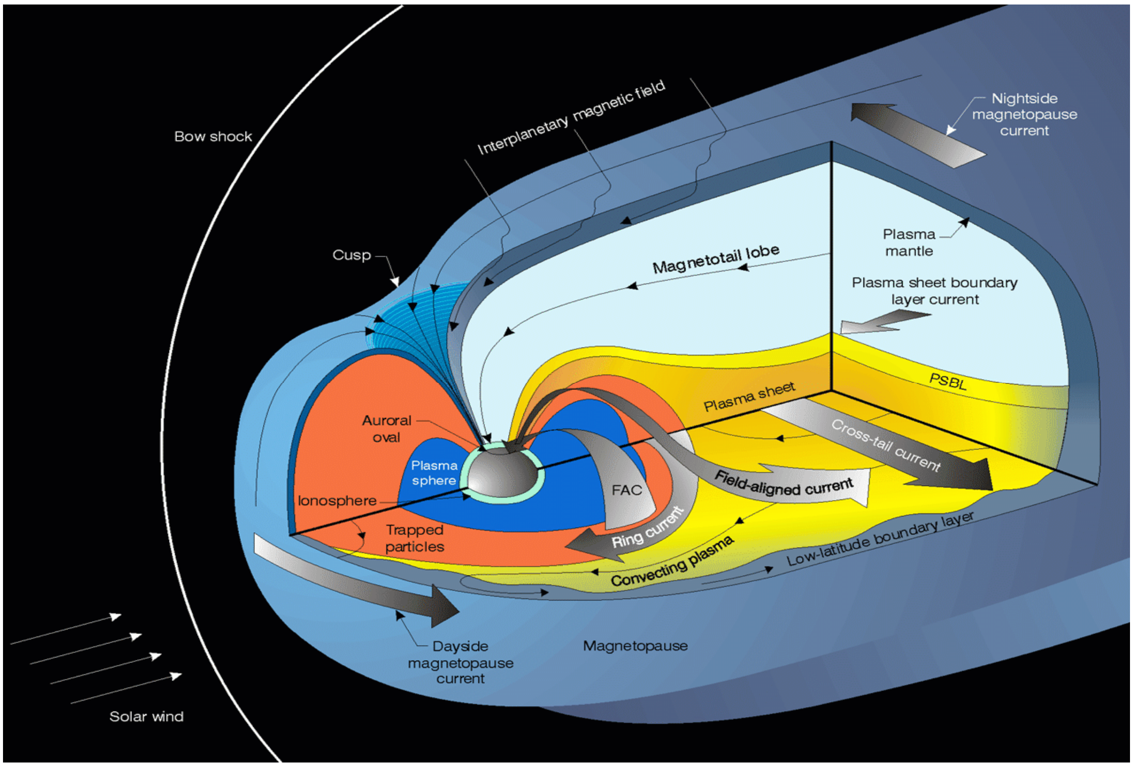

Figure 1.1. Artist's view of the Earth's magnetosphere with its most important particle populations and current systems. The Sun is approximately to the left. Source: website of the Swedish Institute of Space Physics.

Most of the solar wind particles are swept around the Earth's magnetosphere, while others are allowed to penetrate, favored by certain conditions of the IMF and the solar wind. An important source of the stress and energy deposited in the terrestrial environment is precisely provided by the penetrating solar wind particles, albeit it is thought that the deviated particles also play a certain role in the stress and energy balance by means of viscous interaction in the flanks of the magnetosphere [*Axford and Hines*, 1961]. The main mechanism by which solar wind particles penetrate the Earth's magnetosphere was proposed by *Dungey* [1961] in his open magnetosphere model, where magnetic reconnection between the IMF and the high-latitude terrestrial magnetic field takes place in the dayside magnetopause. When this occurs, charged solar wind particles blowing over the poles are subject to the higher intensity of the Earth's magnetic field, giving rise to a charge separation and a current caused by the solar wind dynamo effect. The electric potential difference produced by this charge separation has an associated electric field, with a typical polarization from dawn to dusk, which is mapped along the highly conducting magnetic field lines of the Earth into the high-latitude ionosphere, where the circuit is closed thanks to the relatively high conductivity of this medium in the direction perpendicular to the magnetic field [e.g., *Prölss*, 2004].

1.2. THE IONOSPHERE

Particle radiation is accompanied in its way out of the Sun by electromagnetic radiation. The Earth's ionosphere is the part of the upper atmosphere that is partially ionized by the effect of this electromagnetic radiation (extreme ultraviolet and X-ray radiation primarily), but also by energetic particle precipitation in polar latitudes [*Kelley*, 2009] and by cosmic rays, either from solar or galactic origin [e.g., *Richmond*, 1995a]. The existence of charge carriers in this layer confers certain conductivity on it, allowing for electric currents to flow, thereby leading to additional magnetic field perturbations and electrodynamic heating effects.

Due to the gradual variation in the electron density vertical profile (Figure 1.2, right panel), there exists no consensus as to the limits of the ionosphere, although plasma densities beyond 10^{10} m^{-3} (10^{4} cm^{-3}) are typically found between about 80 and 1000 km height, depending on many factors such as local time (mainly day or night time) and solar activity. This is the reason why the lower limit of the ionosphere is reported to be as low as 60 km in some textbooks. This region of space can be divided into different layers on the basis of the electron density and radio wave propagation properties. Thus, the D region is the part of the ionosphere below about 90 km with traces of heavy positive and negative ions; the E region is the part between about 90 and 170 km mainly dominated by electrons and the positive molecular ions O_2^+ and NO^+, while electrons and O^+ ions dominate in the F region, which extends roughly between 170 and 1000 km. The latter region usually contains the maximum plasma density (between 10^{11} and 3×10^{12} m^{-3}) at heights between 220 and 400 km. Such configuration is essentially valid at daytime. At nighttime, the D region vanishes, and so does the F1 region, which is the lower part of the F region; the E layer is strongly reduced, while the upper F region, termed F2 region, tends to persist. The temperature of the atmosphere above 90 km increases dramatically, and at heights above about 200 km it asymptotically approaches a limiting value of 600 to 2000 kelvin

(Figure 1.2, left panel), reason by which it is designated the thermosphere. The temperature increase in this region is due in part to the absorption of solar ultraviolet (UV) radiation producing ionization processes.

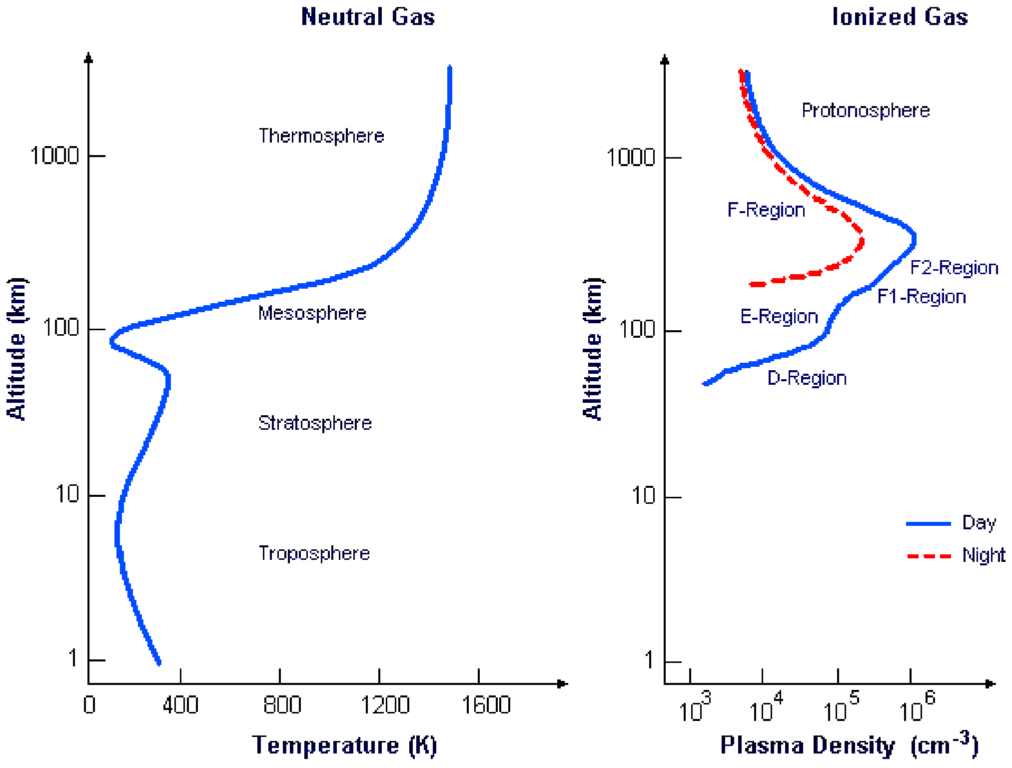

Figure 1.2. Typical temperature (left panel) and electron density (right panel) vertical profiles of the Earth's atmosphere and ionosphere, with their most relevant layers. Adapted from *Kelley* [2009].

Only a relatively narrow range of the ionosphere (typically within 10 km around 110 km height, i.e., within the E region) has a major importance from the point of view of its currents and associated magnetic effects. This is the so-called dynamo region, where conductivity is provided by differential motion of ions and electrons in response to driving electric fields [e.g., *Richmond and Thayer*, 2000]. Such electric fields are due to either electrostatic potentials or electromotive forces appearing as a result of the tidal movement, mainly of solar (but also of lunar) origin, of the (major) neutral component of the upper atmosphere, also known as the neutral wind. As a result of the latter, a current system is produced from the equatorial to the midlatitude dayside ionosphere (in both northern and southern hemispheres), which is usually termed the Sq (stemming from Solar Quiet) current system (Figure 1.3).

Besides these midlatitude currents, mainly produced by electromotive forces, electrostatic potential drops also exist. Examples of these are the potential differences existing at high latitudes as a result of the solar wind dynamo effect after reconnection of the IMF with the Earth's magnetic field. As mentioned above, the ionosphere often closes the circuit caused by potential differences between distant points in the

Figure 1.3. Sketch of the large-scale Sq current system flowing in the midlatitude dayside ionosphere. Arrowed lines indicate the sense of the current. Adapted from *Campbell* [2001].

magnetosphere, and hence a magnetosphere-ionosphere coupling is produced, where the latter region usually acts as an electric load, dissipating energy [e.g., *Strangeway et al.,* 2000]. The "wires" connecting both regions of the terrestrial environment are the magnetic field lines, and hence the Birkeland currents, also known as geomagnetic field-aligned currents, are an important means of energy transportation into the upper atmosphere. Figure 1.4 shows a compendium of the numerous ionospheric phenomena occurring at a global scale, which are ultimately driven by the Sun.

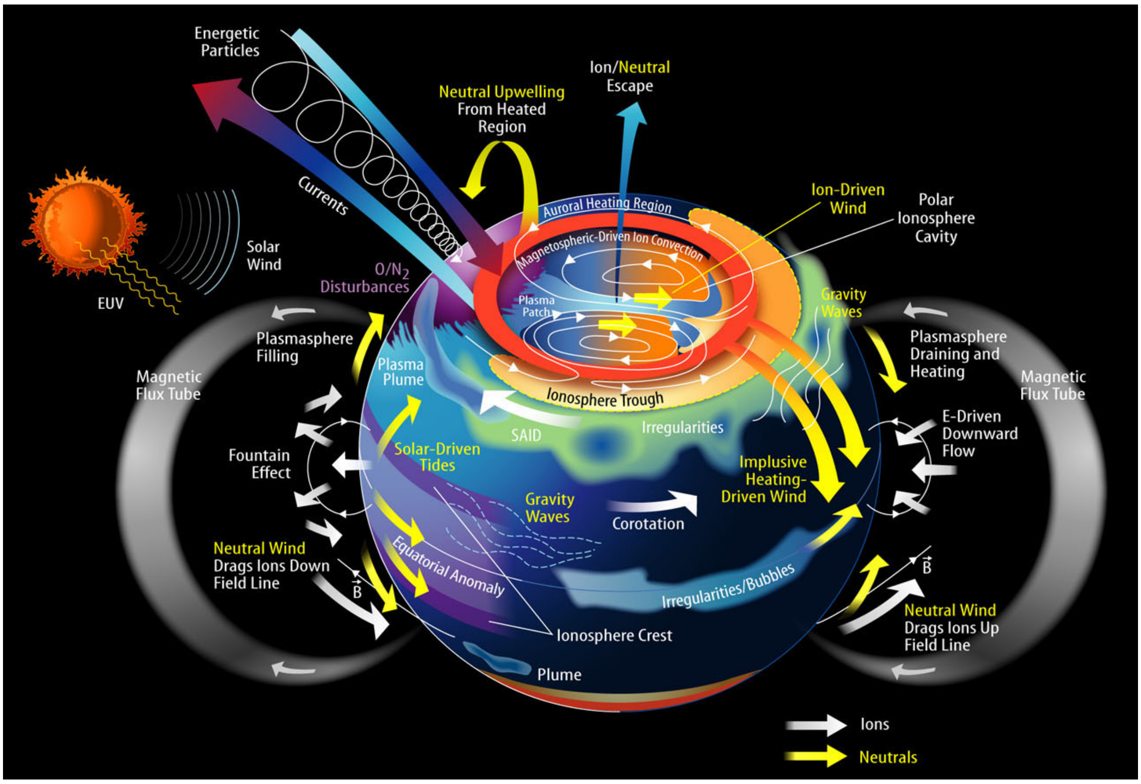

Figure 1.4. Schematics of the main neutral wind and current systems in the ionosphere, along with some related phenomena and its coupling with the magnetosphere. Source: National Aeronautics and Space Administration (NASA).

1.3. SPACE WEATHER, SPACE CLIMATE AND THEIR SOCIETAL IMPLICATIONS

It is worth emphasizing at this point that the Sun is not a static body, but the amount of energy emanating from it varies with time. Some violent phenomena in the solar corona, for example, expel huge amounts of energetic solar material into interplanetary space, substantially increasing the density and velocity of the solar wind, and potentially leading to geospheric storms if the appropriate conditions in the IMF are met when this energy eventually arrives at the Earth’s orbit. We can define geospheric storm as an event of strongly enhanced dissipation of solar wind energy in the near-Earth space environment, leading to a great variety of phenomena like geomagnetic storms, auroral and substorm activity, thermospheric and ionospheric storms, etc. [*Prölss*, 2004]. The concept of geospheric storm is closely connected to the discipline of Space Weather, which refers to conditions on the Sun and in the solar wind, magnetosphere, ionosphere and thermosphere that can influence the performance and reliability of spaceborne and ground-based technological systems (as defined by the United States National Space Weather Program). Because our society is becoming increasingly dependent on those technological systems, which can be affected by ionospheric phenomena during geospheric storms, the ionosphere, its electrodynamics, and its coupling with the neutral atmosphere and the magnetosphere are a matter of intensive research. This research seeks to characterize the variability of ionospheric density and electric currents during such storms, and to determine to what extent valid predictions of those phenomena and their effects can be made [*Richmond*, 1996].

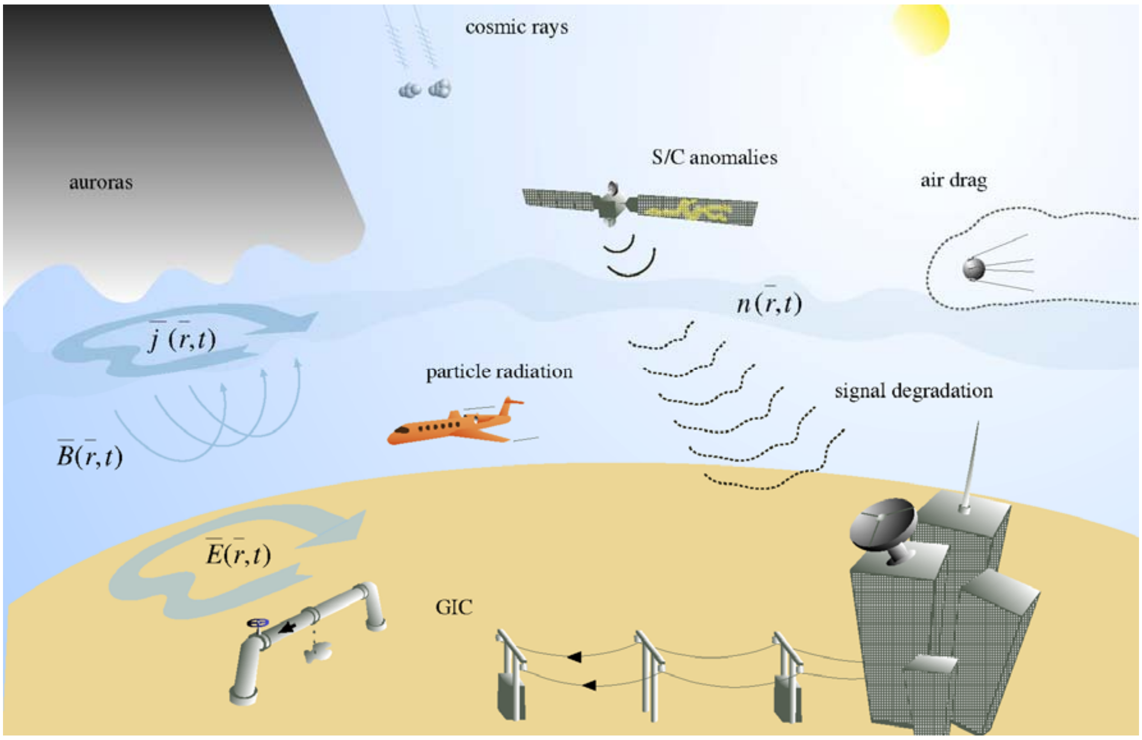

Figure 1.5. Illustration showing different aspects of space weather effects on human technology. Figure by Ari Viljanen (Finnish Meteorological Institute).

The implications of space weather on numerous aspects of life in our planet, and particularly on human society, are well-known and recognized by many authors [e.g., *Koskinen et al.*, 2001]. Some examples, depicted in Figure 1.5, are given in the following paragraphs.

The conducting nature of the ionosphere plays an important role in the field of electromagnetic wave propagation, enabling radio communications between distant points of the Earth, or refracting the signal emitted by the global navigation satellite system (GNSS), among other effects. The total electron content (TEC) of the ionosphere may increase substantially during strong ionospheric storms, causing variability in the propagation conditions. The so-called solar proton events (SPE), for instance, can cause episodes of enhanced absorption of radio waves in the Earth's polar caps known as polar cap absorption (PCA) events, thereby restricting (if not disabling) transpolar high-frequency (HF) radio communications. Commercial airlines are potentially affected by these disruptions when they overfly the polar zones, being obliged to deviate from their projected shortest routes towards lower latitudes. The accuracy of single frequency receivers of GNSS signals can also be affected by intense TEC enhancements and ionospheric scintillations produced by irregularly structured regions, as these signals suffer from unknown delays and scattering. Thus, knowledge of the ionospheric behavior leads to a better understanding and prediction of the processes involved in many technological systems of communication [*Daglis*, 2004].

High-energy SPEs and galactic cosmic rays (GCR) can also expose astronauts to radiation levels above the safety limits, especially those working in the exterior of their spacecraft or in unprotected areas, due to lack of atmospheric shielding. Particle solar radiation can also incur damages in satellite-borne equipment like solar panels; they can produce surface charging in spacecraft causing scrambled satellite signals, or they can induce small voltages in electronic equipment which can result in false commands being delivered. This especially applies to missions (either manned or not) passing through the Van Allen belts, where protons up to hundreds of MeV are confined. Although to a smaller extent, frequent flyers of airlines especially covering high latitudes are also subject to the cumulative effect of particle radiation, because they fly under a thinner layer of the atmosphere, which is thus more accessible to energetic radiation.

Temperature-induced inflation of the thermosphere during geospheric storms can cause low Earth orbit (LEO) satellites to reduce its speed and even fall prematurely due to enhanced drag with this part of the upper atmosphere (this turned out to be the case of the Skylab space station, which re-entered the atmosphere earlier than expected).

Strong currents developed at the ionosphere of relatively high magnetic latitudes during geomagnetic storms and substorms produce strong and highly variable magnetic fields at the Earth's surface. Because the interior of our planet has a finite conductivity, these incoming perturbations, which can be regarded as electromagnetic waves traveling downward, produce induced currents in the solid earth and oceans. Such currents in turn produce a secondary magnetic field measurable with ground-based magnetometers, which can be understood as a reflection of the incoming wave. These phenomena peak in the so-called auroral zones, at latitudes where the aurorae are typically observed and where the so-called auroral electrojets form in the ionosphere. Because the intensity of the induced currents can be considerable, they can introduce a substantial direct current (DC) signal in the electrical power transmission grids, which are set up for alternating current (AC) flow, causing serious damages to the network transformers and potentially affecting the final user (Figure 1.6). These currents, especially when they affect ground-based technical networks, are generally termed geomagnetically-induced currents (GICs). A typical example used in this context is the severe geomagnetic storm occurred in March 13, 1989, which collapsed the entire power grid supplying the Canadian sector of Quebec and caused a power outage affecting more than 6 million people during 9 hours [*Kappenman et al.,* 1997]. This type of events has raised awareness of the electrical companies about the potential hazard of severe geomagnetic events to their transmission lines, and they have taken ongoing measures to evaluate the potential risk of damages, not only at high but also at middle and low latitudes [e.g. *Torta et al.*, 2014]. By similar reasons, GICs can affect the anti-corrosion system of pipelines transporting oil and gas along hundreds of kilometers, causing expensive costs to the running companies.

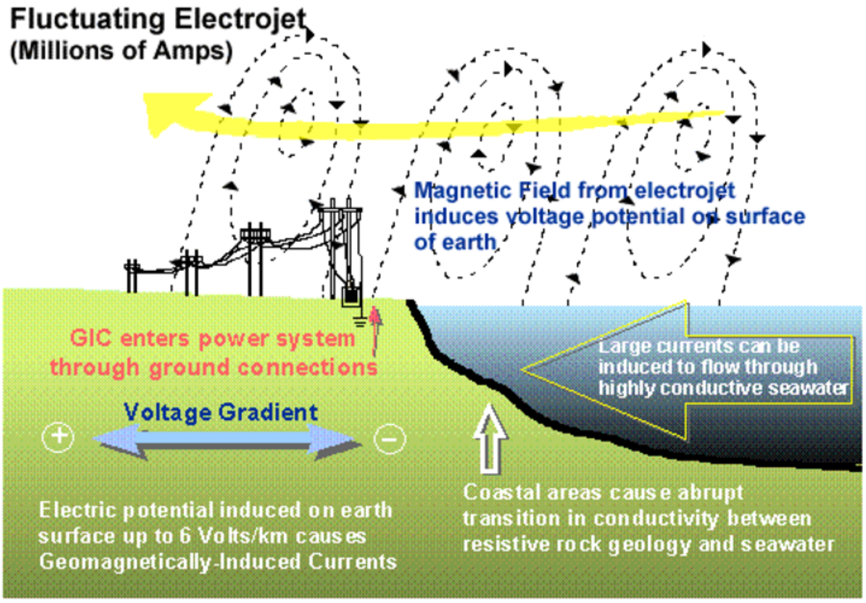

Figure 1.6. Sketch showing the mechanism of generation of GICs on power grids. Figure by John Kappenman (Metatech corporation).

There also exists evidence that intense GICs can hamper rail traffic by disturbing signaling and train control systems [e.g., *Ptitsyna et al.*, 2008]. Such a threat concerns long railway segments and is primarily caused by high-latitude geomagnetic disturbances driven by the auroral electrojet, but also by storm sudden commencements (SC) and pulsations, which can affect a higher range of latitudes.

Another growing branch of geophysics is the study of the potential relation between the Sun and the Earth's climate, and it intends to establish the precise role of this link in the vast and complex subject of the climate changes [*Vázquez*, 1998]. *Svensmark and Calder* [2007], in their controversial book, stated that the solar activity reduces the influx of GCRs onto the upper atmosphere, thereby producing depletion in the number of available condensation nuclei for the formation of clouds in the troposphere**.** This would decrease the Earth albedo, which in turn would increase the heat input from the Sun, eventually contributing to a global warming. As examples of this, it is the subject of ongoing debate the exact weight of anthropogenic versus solar causes of the present global climate change, or the possible link between the lower-than-average temperatures affecting an important part of the northern hemisphere during the second half of the 17th century and beginning of the 18th (which has come to be known as the Little Ice Age) and the low solar activity during that time (the so-called Maunder minimum) [*Legrand et al.,* 1990]. Still related to modulations of the GCR flux (although the exact mechanisms are not clear at present), other studies [e.g., *Gallet et al.*, 2007, and references therein] show a coincidence between periods of rapid increase in the magnetic dipole moment of the Earth and climate cooling events.

Finally, it is worth mentioning that a substantial number of studies have also been carried out about the negative effects of geomagnetic activity on diverse aspects of human physiology, not only in space, but also on the Earth's surface [e.g., *Cornélissen et al.,* 2002; *Papailiou et al.*, 2011; *Feigin et al.,* 2014].

1.4. MOTIVATION AND SCOPE OF THE PRESENT WORK

It has been stated that space weather can be compared to Earth's weather in terms of our interest to forecast its immediate consequences. However, our current knowledge and prediction capabilities of the space phenomena is comparable to the situation that we had fifty years ago in terms of atmospheric modeling [*Hapgood*, 2012]. Having stressed in this chapter the increasing importance of systematically studying space weather phenomena to advance in the knowledge and forecasting capabilities of severe events potentially affecting our technology-based society, the aim of the following chapters is to situate the present work in the context of the multidisciplinary studies related to the solar-terrestrial physics and to establish its objectives.

We can divide the vast subject of the solar-terrestrial physics in different disciplines, corresponding to the different segments of the space from the Sun to the Earth's surface being considered. Obeying this division, this work would pertain to one of the last portions, as it deals with the modeling of aspects of the solar activity on the terrestrial environment, including the inner magnetosphere and upper atmosphere. Specifically, our interest will mainly (though not exclusively) be focused on the description of the magnetic field disturbances on the Earth's surface. In fact, ground magnetic records are an evidence of the phenomena described above, and its study, supported by the long tradition and the global coverage of these measurements, has helped to reveal the nature of a number of aspects concerning the solar-terrestrial physics.

Understanding the upper atmosphere processes and their associated magnetic field variations is not only fascinating from a purely theoretical point of view but it is of major importance in some sub-disciplines of Space Weather with clear practical implications in human society, such as that studying GICs or health-related phenomena. Our personal motivation and, by extension, the objective of this work is thus advancing in the knowledge of the coupling mechanisms of the magnetosphere-ionosphere system; in particular, we will be concerned with geomagnetic field-aligned currents, which are active drivers of the high-latitude (and to a great extent of the global) upper atmosphere and are deemed responsible of space weather phenomena when they are closed through the conducting ionosphere under perturbed conditions. These currents could indeed be considered the last link in the chain of events from the solar atmosphere to the ionosphere, their specification being essential (if not major) to upper atmosphere models as the one addressed here.

The aim of this work is to describe in more detail the technique applied for the first time in the paper by *Marsal et al.* [2012], and subsequently exploited in the case study carried out by *Blanch et al.* [2013], for which use is made of the TIE-GCM model. Details are also given of a recent extension of this method. For purposes of studying the ground magnetic perturbations at middle and high latitudes and the connection with their sources in the ionosphere and magnetosphere, this technique is focused on improving the modeling of the upper atmospheric processes. We are especially interested in high-latitude events during disturbed conditions, which are closely related to the interplanetary conditions and magnetospheric phenomena, and specifically on realistically modeling the spatial and temporal variation of the high-latitude forcing. Our approach consists in making use of the newly available, high-resolution Birkeland current distribution provided by the Active Magnetosphere and Planetary Electrodynamics Response Experiment (AMPERE) to drive the ionosphere electrodynamics solution in the TIE-GCM model. A thorough description of the procedure will be carried out here, and the achievements and limitations of the technique will be discussed from a critical point of view on the basis of new case studies. In particular, chapter 2 introduces the subject of Earth's magnetism and modeling, and develops fundamental concepts and equations relevant to this work. In chapter 3, the reader's interest is progressively focused on the physics and phenomena of the upper atmosphere, especially at high latitudes. Chapter 4 introduces the AMPERE mission and data set, as well as the TIE-GCM model, which this work is based on. Chapter 5 thoroughly describes the author's contribution to space physics modeling. Chapter 6 applies the technique to different case studies and discusses the results from a critical point of view. Finally, chapter 7 concludes with some final remarks and future guidelines.

1.5. STATE OF THE ART

Though the next chapter is aimed at situating this work in a general context, we summarize here the most important connections of our work with others having related objectives.

General circulation models (GCM), i.e., mathematical models of the general circulation of a planetary atmosphere, started to proliferate during the second half of the 20th century, with the advent of computer science [e.g., *Phillips*, 1956; *Smagorinsky,* 1963]. While these first GCMs were applied to lower atmosphere science and its coupling with oceans, upper atmospheric (mainly purely thermospheric) models started to be developed by several groups in the late seventies and early eighties [e.g., *Roble et al.,* 1977; *Fuller-Rowell and Rees,* 1980; *Serebriakov,* 1982], which were afterwards coupled with the ionospheric dynamo and with the magnetosphere [e.g., *Namgaladze* *et al.,* 1990; *Richmond et al.*, 1992; *Peymirat et al.,* 1998; *Millward et al.,* 2001; *Raeder et al.,* 2001a; *Ridley et al.,* 2003; *Wiltberger et al.,* 2004; *Wang et al.,* 2004; *Klimenko et al.,* 2006; *Ren et al.,* 2009; *Jin et al.,* 2011; *Pembroke et al.,* 2012] (see *Richmond and Maute* [2014] for an extended review of ionospheric electrodynamics modeling).

One of these models, the National Center for Atmospheric Research Thermosphere-Ionosphere-Electrodynamics General Circulation Model (NCAR TIE-GCM) is an essentially physical model trying to diagnose the upper atmosphere of the Earth. It can be driven by a series of parameters and/or indices describing the solar wind conditions and the effectiveness of its coupling with the Earth's environment [*Heelis et al.,* 1982; *Weimer,* 2005]. These parameters, which are linked to the model by rather statistical relationships, are in most cases reasonable estimates of the average conditions comprising a great variety of external situations, though they fail in specifying the particular circumstances of stress and energy being dumped from the magnetosphere at each particular time and location of the ionosphere. Other drivers are more in the field of complementary magnetospheric physical models including an interface with the TIE-GCM [e.g., *Peymirat et al.,* 1998; *Ridley et al.,* 2003], one example of the latter being the Coupled Magnetosphere Ionosphere Thermosphere model (CMIT), which is aimed at coupling the former with the Lyon-Fedder-Mobarry (LFM) magnetosphere-ionosphere model. The complexity and power of this tool in modeling the Earth's segment of the space weather chain is noteworthy, and some milestones have already been achieved [e.g., *Merkin and Lyon,* 2010; *Wang et al.,* 2004].

An alternative approach commonly utilized in driving the TIE-GCM is the use of real data as an input. In this case, observations of diverse origin are assimilated by the model, as is the case of Assimilative Mapping of Ionospheric Electrodynamics (AMIE)-type data, including radar, satellite, magnetometer and other types of available data [*Emery et al.,* 1996; *Lu et al.,* 1998]; electric field data from the Super Dual Auroral Radar Network (SuperDARN) [e.g., *Shiokawa et al.,* 2007]; or thermospheric wind and temperature data from the Thermosphere-Ionosphere-Mesosphere Energetics and Dynamics (TIMED) satellite [*Yamazaki et al.,* 2014]. Feeding a physical model with real data and later comparison of the outputs with observational data helps to discriminate between the model strengths and weaknesses, and thus to improve different aspects of it. In this sense, the real input data play the role of anchoring points enabling to evaluate several outputs of the model (especially those more closely related to the real input) if observational data associated with these outputs are available. AMPERE [*Anderson et al.,* 2008] is a satellite mission providing real and specific information on time, location and magnitude of magnetic field-aligned currents, which are key drivers of the high-latitude ionospheric electrodynamics. This dataset is therefore a natural candidate to be used as a driver of the TIE-GCM. This exercise has been conducted for the first time by *Marsal et al.* [2012], and is thoroughly detailed, and in some aspects extended, in this work.

2. FUNDAMENTAL CONCEPTS

2.1. FUNDAMENTALS OF EARTH'S MAGNETISM

The magnetic field measured at a given point on the Earth's surface is contributed by several sources. Over 95 % of the total field originates in the liquid outer core of the Earth in a dynamo process that converts kinetic energy into magnetic energy. This main field, also known as core field, varies at the surface between about 23,000 nT in the so-called South-Atlantic Anomaly sector and 66,000 nT near the South magnetic pole, and it is sometimes approximated by the magnetic field that an eccentric dipole (i.e., a current loop with the appropriate intensity, direction and location in the interior of our planet) would produce on the Earth's surface, reason by which it is also known as dipole filed. The associated variations of the main field are relatively smooth and constant in a timescale of decades or even centuries, with typical variations of the order of tens of nanoteslas per year in a given location [e.g. *Parkinson*, 1983].

Both the remanent and the induced magnetization of rocks in the lithosphere also contribute to the total magnetic field. The first type of magnetization was frozen into rocks at the moment of their formation, when their temperature cooled below a certain threshold known as Curie point, after ascending from the hot mantle. The second type of magnetization depends on the magnetic susceptibility of crustal rocks, and is imposed on them by the main field. Due to its space variability, the individual features of these magnetizations as measured above the surface are often referred to as magnetic anomalies. Some of these anomalies may extend along hundreds of kilometers, and have an amplitude of several thousand nanoteslas as revealed by aeromagnetic surveys [*Lühr et al.,* 2009]. Internal sources (i.e., below the Earth's surface) are completed by induced currents flowing in the conducting Earth. Such currents appear as a result of Faraday's induction law (see equation (2.1)) in response to variable external sources, often referred to as primary sources, mainly in the ionosphere. Their intensity varies depending on the rate of variation of the primary sources, ranging from a few nanoteslas to tens or even hundreds of nanoteslas below the auroral zones during disturbed periods. Magnetic fields arising from motional induction driven by ocean tidal flow can be considered a particular subset of the latter. The electric currents originating from the highly conductive sea water moving within the Earth's magnetic field produce small magnetic signals of the order of a few nanoteslas.

The external sources of the magnetic field are the current systems flowing in the magnetosphere and the ionosphere (see sections 1.1 and 1.2). The ionospheric currents produce daily regular variations of the order of tens of nanoteslas at midlatitudes during geomagnetically quiet periods, while the regular variations of magnetospheric origin use to be of lesser extent. However, during disturbed periods the ionosphere produces variations of hundreds or even thousands of nanoteslas at high latitudes, and tens or hundreds of nanoteslas in the case of the magnetosphere, especially due to ring current enhancements affecting low latitudes.

The magnetic field vector can be represented in different coordinate systems in a geographical local reference frame, giving rise to the different magnetic elements, as seen in Figure 2.1. The elements in Cartesian coordinates are denoted as the triple *X*, *Y*, *Z*, corresponding to the geographic north, east and downward projections, respectively; in cylindrical coordinates they are denoted as *H*, *D*, *Z*, standing for the horizontal projection, declination (angle between the true north and the horizontal projection of the magnetic field, positive towards East) and downward projection; and in spherical coordinates they are denoted as *D*, *I*, *F*, corresponding to the declination, inclination (angle between the horizontal plane and the magnetic field vector, positive downward), and total field intensity.

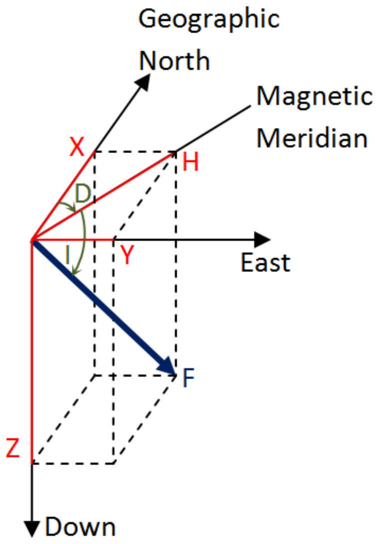

Figure 2.1. The magnetic field vector and its elements in the geographic reference frame.

Geomagnetic observatories are permanent locations on the Earth's surface aimed at measuring the time evolution of the natural geomagnetic field vector [*Rasson*, 2007]; such objective is essential not only for science but also for commercial and governmental purposes. The world-wide network of observatories providing magnetic field data has variably increased since its origins at the first half of the 19th century up to a population around 180 at the present time [*Macmillan*, 2007]. The International

Association of Geomagnetism and Aeronomy (IAGA) is the section of the International Union of Geodesy and Geophysics (IUGG) in charge of their coordination, as well as of promoting research in the field of geomagnetism and aeronomy, and of standardizing observatory practice [*Jankowsky and Sucksdorff*, 1996]. Despite the present number of observatories is not negligible, a map of their global distribution evidences drawbacks with respect to the coverage, as there exist large areas, especially in the oceans, Antarctica, Africa and South America with few settlements, in contrast to the high density of geomagnetic observatories in central Europe. Other means of measuring the magnetic field, like satellites, are employed to cover sparse areas of our planet, while others like marine and land campaigns, or aeromagnetic surveys, are principally intended to measure the spatial variability of the crustal field.

Magnetometers are the instruments aimed at measuring the magnetic field. There exists a large variety of technologies being used in magnetometry, some examples being proton magnetometers, which are based on the magnetic properties of fundamental particles interacting with the Earth's magnetic field, optically pumped magnetometers, which are based on quantum effects, or those purely electronic, like the fluxgate or the coil systems [*Rasson*, 2007]. There is an increasing tendency in modern magnetometers to use fluxgate technologies [e.g., *Ripka*, 2000], as they provide a considerable resolution both in time and in magnetic field measurements themselves. The widely used D/I fluxgate theodolites [e.g. *Lauridsen*, 1985] (see *Marsal and Torta* [2007] for an assessment of this instrument) and the triaxial fluxgate magnetometers are some examples of instruments using this technology.

2.2. MAGNETIC FIELD MODELS

Magnetic field models are intended to provide the magnitude of the different elements of the geomagnetic field vector at a given point in time and space. Depending on the nature of the model, it is possible to group them into two different categories: (1) statistical, empirical, or inverse models, and (2) physical, first-principles, forward, or simulation models. Note, however, that these qualifiers are not necessarily equivalent among them, and some models may combine features of both categories.

The first set of models is aimed at describing the geomagnetic field by means of well-behaved mathematical functions whose parameters are adjusted via real data assimilation by use of inversion techniques. Most of the physics are thus implicit in the model basis functions, though accurate selection and treatment of the data sources, as well as adequate data processing tools is required. Examples of statistical models of the magnetic field based on combined ground and space data are the International Geomagnetic Reference Field (IGRF) [e.g., *Finlay et al.*, 2010] (Figure 2.2), the Comprehensive Model [e.g., *Sabaka et al.*, 2004] and the Potsdam Magnetic Model of the Earth (POMME) [e.g., *Maus et al.,* 2010] model series. All of them give a mathematical representation of the magnetic field using spherical harmonic functions up to a certain degree. However, the IGRF series, which are generally revised every five years, are intended to account only for the main field contribution, while the latter two include lithospheric as well as external magnetic field sources. Many other statistical models of middle- and low-latitude magnetic field variations at the ground have been presented [e.g., *Yamazaki et al.,* 2011]. Worth mentioning in this context are the magnetospheric magnetic field models by N. Tsyganenko [e.g., *Tsyganenko*, 2014], who uses satellite data to adjust theoretically-derived descriptions of the magnetic field produced by the main currents surrounding the Earth.

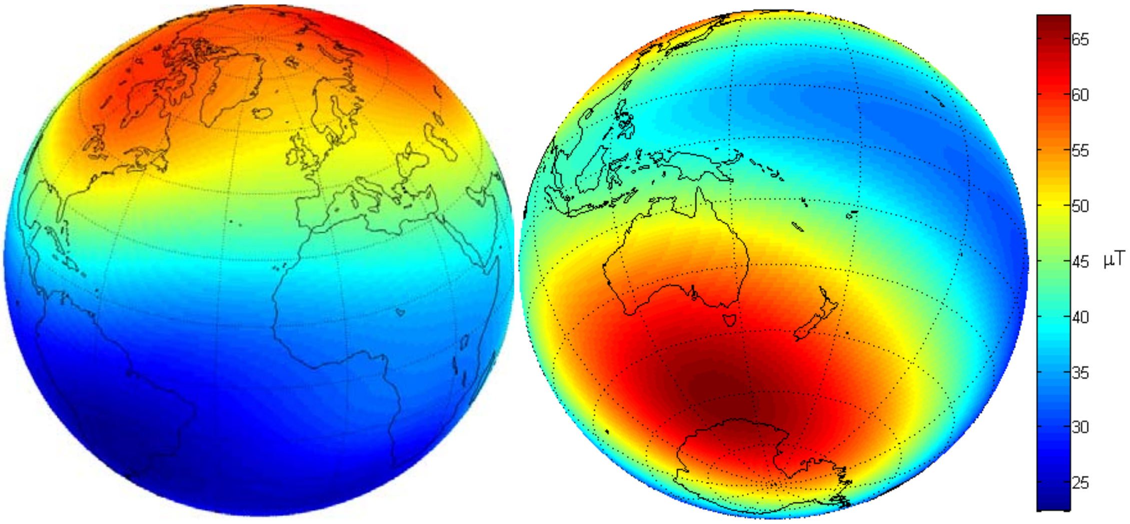

Figure 2.2. Map of the total intensity *F* of the geomagnetic field on the Earth's surface synthesized from the 11th generation of the IGRF model for the epoch 2014.0.

Besides these statistical approaches, many authors have studied the ground magnetic effects of the current systems surrounding the Earth on a more theoretical basis; some of the most notable are enumerated here: *Van Sabben* [1966] computed the ground magnetic effects of geomagnetic field-aligned currents flowing between conjugate ionospheres, and suggested that such currents may account for a significant part of the North-South asymmetry of the solar-quiet magnetic variation observed during equinoxes. *Fukushima* [1969] established his theorem regarding the null magnetic effects on the ground of radial field-aligned currents being closed by irrotational horizontal (mainly Pedersen) currents in the ionosphere. *Kamide and Matsushita* [1979a, 1979b] calculated the equivalent currents of statistical distributions of field-aligned currents flowing into and out of the high-latitude ionosphere during both quiet and disturbed periods. *Kamide et al.* [1981] developed the Kamide-Richmond-Matsushita (KRM) inversion method consisting in the estimation of ionospheric electric fields and currents from real ground magnetic records; this and the previous method assume known ionospheric conductance distributions. The Assimilative Mapping of Ionospheric Electrodynamics (AMIE) procedure extended that inversion technique to the assimilation of diverse types of observations (including ground magnetometer data) to estimate the contemporaneous distributions of various electrodynamic quantities over the polar regions consistent with the observations [e.g., *Richmond and Kamide,* 1988; *Richmond*, 1992; *Lu et al.,* 2001; *Wilder et al.,* 2012]. Both the KRM and AMIE techniques, which indeed can be classified as statistical models for the use of large data sets that need to be assimilated, assume certain approximations like radial magnetic field lines and the neglect of the dynamo effect produced by neutral winds.

Simulation models of ionospheric currents which include their coupling with the magnetosphere have been used to examine magnetic perturbations on the ground.

Magnetohydrodynamic magnetospheric models have been used to estimate the magnetic perturbations under the auroral electrojets [e.g., *Raeder et al.,* 2001b; *Shao et al.,* 2002; *Pulkkinen et al.,* 2007, 2011; *Yu and Ridley*, 2008]. The NCAR TIE-GCM was used to compute magnetic perturbations at low and middle latitudes by *Doumbia et al.* [2007] for quiet conditions and by *Zaka et al.* [2010] for a disturbed period for comparison with observations. These models are based on first principles, meaning that they have explicit physical equations in their computer codes that allow computing derived quantities from a few simple observational (or fictitious) parameters. This fact makes them forward models in contrast to the inverse models discussed earlier. The use of the first-principles models has the advantage of incorporating our present knowledge of the upper atmospheric science from a theoretical point of view. This provides them with more potential, as permits a direct evaluation of our limitations and subsequent revision of the theory if comparisons with the observations are found unsatisfactory. In contrast, the results of these latter models use not to be as accurate as those from empirical models.

2.3. FUNDAMENTAL EQUATIONS

This section deals with the fundamental equations of the electrodynamics that will be relevant to this work. First of all, we limit ourselves to presenting Maxwell's equations in the vacuum for an inertial reference frame, which are widely discussed in fundamental textbooks (e.g., *Reitz et al.* [2008], *Prölss* [2004] or *Kelley* [2009]):

$$\vec{\nabla} \times \vec{\boldsymbol{E}} = -\frac{\partial \vec{\boldsymbol{B}}}{\partial t}, \tag{2.1}$$

$$\vec{\nabla} \times \vec{\boldsymbol{B}} = \mu_0 \vec{\boldsymbol{J}} + \mu_0 \varepsilon_0 \frac{\partial \vec{\boldsymbol{E}}}{\partial t}, \tag{2.2}$$

$$\vec{\nabla} \cdot \vec{\boldsymbol{E}} = \frac{\rho}{\varepsilon_0}, \tag{2.3}$$

$$\vec{\nabla} \cdot \vec{\boldsymbol{B}} = 0. \tag{2.4}$$

$\vec{\boldsymbol{J}}$ is the current density (A/m^2), $\vec{\boldsymbol{E}}$ is the electric field, $\vec{\boldsymbol{B}}$ is the magnetic flux density, generally (and hereafter) simply referred to as magnetic field, t is time, ρ is the electric charge density, and μ_0 and ε_0 are the permeability and permittivity of free space, respectively. Equations (2.1) to (2.4) are Faraday's induction law, Ampère-Maxwell's law, Gauss's law, and Gauss's law for magnetism, respectively. An abrupt temporal change of the magnetic field (e.g., associated to a substorm or to a magnetic sudden impulse) gives rise to an induced, rotational electric field in virtue of Faraday's law. However, the electric field is generally assumed to derive from an electrostatic potential Φ, so that $\vec{\boldsymbol{E}} = -\vec{\nabla}\Phi$. For this condition to be fulfilled we must firstly consider phenomena that vary with time scales longer than a minute or so, thus omitting rapid changes; and secondly, the electric field must be described in a reference frame where the main magnetic field does not explicitly vary with time. A reference frame co-rotating with the Earth accomplishes such condition in the vicinity of our planet, and (2.1) to (2.4) are still reasonably valid despite the non-inertial nature of this frame. In an inertial reference frame co-moving with the Earth, on the contrary, our planet rotates, carrying along the magnetic field with it. Even so, if the magnetic field were dipolar and its axis coincided with the rotation axis, the magnetic field would not change with time. Since this is not far from the real situation (the dipole axis is currently less than 10° apart from the rotation axis), we assume that the (rotational) electric field induced by the temporal change of the main field is negligible in this co-moving reference frame. As a result, $\vec{\boldsymbol{E}} = -\vec{\nabla}\Phi$ results in a good approximation in both frames, though we will be mainly concerned with the Earth-fixed (i.e., the co-rotating) one in the discussion below.

Introducing the divergence of (2.2) into (2.3), and accounting for the fact that the curl of a vector does not diverge, one gets:

$$\vec{\nabla}\cdot\vec{\boldsymbol{J}} = -\frac{\partial\rho}{\partial t}, \tag{2.5}$$

which is the current continuity equation, and describes the fact that the total electric charge is locally conserved, i.e., the divergence of the current density (or simply *current*) at a given point is the rate of reduction of the charge density at that point.

There is also need of an equation that describes the reaction of the electric fluid within a certain medium to an imposed external forcing like an electric field. This equation is a generalized form of Ohm's law, which can be written as

$$\vec{\boldsymbol{J}} = \boldsymbol{\sigma}\vec{\boldsymbol{E}} + \vec{\boldsymbol{J}}_{\boldsymbol{no}}, \tag{2.6}$$

where $\boldsymbol{\sigma}$ is the electric conductivity tensor, which depends on the characteristics of the medium, $\boldsymbol{\sigma}\vec{\boldsymbol{E}}$ is the ohmic component of the current, and $\vec{\boldsymbol{J}}_{\boldsymbol{no}}$ its non-ohmic component (i.e., not proportional to the electric field). Although $\vec{\boldsymbol{J}}_{\boldsymbol{no}}$ may include a number of components in the Earth's space environment, such as pressure gradient, gravity or inertial forces, we will consider that it essentially consists of a thermospheric component proportional to the electromotive force $\vec{\boldsymbol{u}}\times\vec{\boldsymbol{B}}$, where $\vec{\boldsymbol{u}}$ is the velocity of the thermospheric neutral wind, often called the *dynamo electric field*, and a magnetospheric component $\vec{\boldsymbol{J}}_{\boldsymbol{M}}$, which includes, among others, parallel electric fields connecting with the auroral zone, as well as curvature and magnetic gradient differential drifts in the magnetopause and ring current regions. In contrast, the ohmic component $\boldsymbol{\sigma}\vec{\boldsymbol{E}}$ is essentially due to the conducting ionosphere.

Both the electric and magnetic fields depend on the observer's reference frame. If we denote with a subscript zero the frame of reference where the neutral wind is locally at rest (i.e., where $\vec{\boldsymbol{u}}_{\boldsymbol{0}} = 0$), then $\vec{\boldsymbol{B}}_{\boldsymbol{0}} = \left(\vec{\boldsymbol{B}} - \vec{\boldsymbol{u}}\times\vec{\boldsymbol{E}}/c^2\right)/\sqrt{1-|\vec{\boldsymbol{u}}|^2/c^2}$, for which $\vec{\boldsymbol{B}}_{\boldsymbol{0}} = \vec{\boldsymbol{B}}$ turns out to be an excellent approximation, since $|\vec{\boldsymbol{u}}| \ll c$ (c is the speed of light) in any reference frame tied to the Earth. However, that is not the case for the electric field, for which $\vec{\boldsymbol{E}}_{\boldsymbol{0}} = \left(\vec{\boldsymbol{E}} + \vec{\boldsymbol{u}}\times\vec{\boldsymbol{B}}\right)/\sqrt{1-|\vec{\boldsymbol{u}}|^2/c^2}$ is suitably approximated by $\vec{\boldsymbol{E}}_{\boldsymbol{0}} = \vec{\boldsymbol{E}} + \vec{\boldsymbol{u}}\times\vec{\boldsymbol{B}}$. As the total current is proportional to the relative velocities of the electric charges, it does not depend on the observer in the non-relativistic approximation, and $\vec{\boldsymbol{J}}_{\boldsymbol{0}} = \vec{\boldsymbol{J}}$. Therefore, $\vec{\boldsymbol{J}} = \boldsymbol{\sigma}\vec{\boldsymbol{E}} + \vec{\boldsymbol{J}}_{\boldsymbol{no}} = \vec{\boldsymbol{J}}_{\boldsymbol{0}} = \boldsymbol{\sigma}\vec{\boldsymbol{E}}_{\boldsymbol{0}} + \vec{\boldsymbol{J}}_{\boldsymbol{0},\boldsymbol{no}} = \boldsymbol{\sigma}\left(\vec{\boldsymbol{E}} + \vec{\boldsymbol{u}}\times\vec{\boldsymbol{B}}\right) + \vec{\boldsymbol{J}}_{\boldsymbol{M}}$, where $\vec{\boldsymbol{J}}_{\boldsymbol{0},\boldsymbol{no}}$ is the non-ohmic component of the current density in the reference frame where the neutral wind is locally at rest, i.e., essentially $\vec{\boldsymbol{J}}_{\boldsymbol{M}}$. Separating the tensor $\boldsymbol{\sigma}$ in its different components, equation (2.6) takes the following form in this reference frame:

$$\vec{\boldsymbol{J}} = \sigma_B \vec{\boldsymbol{E}}_{\mathbf{0}\parallel} + \sigma_P \vec{\boldsymbol{E}}_{\mathbf{0}\perp} + \sigma_H \widehat{\boldsymbol{b}} \times \vec{\boldsymbol{E}}_{\mathbf{0}\perp} + \vec{\boldsymbol{J}}_{\boldsymbol{M}}, \tag{2.7}$$

where $\widehat{\boldsymbol{b}} = \vec{\boldsymbol{B}}/B$ is the unit vector along the field line, being B the magnetic field intensity; $\vec{\boldsymbol{E}}_{\mathbf{0}\parallel} = \left(\vec{\boldsymbol{E}}_{\mathbf{0}} \cdot \widehat{\boldsymbol{b}}\right)\widehat{\boldsymbol{b}}$ and $\vec{\boldsymbol{E}}_{\mathbf{0}\perp} = \widehat{\boldsymbol{b}} \times \left(\vec{\boldsymbol{E}}_{\mathbf{0}} \times \widehat{\boldsymbol{b}}\right)$ are the vector projections of $\vec{\boldsymbol{E}}_{\mathbf{0}}$ parallel and perpendicular to $\vec{\boldsymbol{B}}$, respectively; σ_B is the Birkeland or parallel component of the conductivity tensor, i.e., the conductivity parallel to the magnetic field; and σ_P and σ_H are the Pedersen and Hall transverse components, respectively. The parallel conductivity σ_B in the ionosphere is several orders of magnitude greater than the transverse components. This implies that any electric potential difference along the field line is immediately balanced by a field-aligned ionospheric current $\vec{\boldsymbol{J}}_{\boldsymbol{i}\parallel} = \sigma_B \vec{\boldsymbol{E}}_{\mathbf{0}\parallel}$, so that $\vec{\boldsymbol{E}}_{\mathbf{0}\parallel}$ is readily neutralized, i.e., $\vec{\boldsymbol{E}}_{\mathbf{0}\parallel} \cong 0$ in the ionosphere although $\vec{\boldsymbol{J}}_{\boldsymbol{i}\parallel}$ is finite. Since $\left(\vec{\boldsymbol{u}} \times \vec{\boldsymbol{B}}\right) \cdot \widehat{\boldsymbol{b}} = 0$, it turns out that $\vec{\boldsymbol{E}}_{\mathbf{0}\parallel} = \vec{\boldsymbol{E}}_{\parallel} \cong 0$, and thus the ionospheric electric field (in any reference frame) is virtually perpendicular to $\vec{\boldsymbol{B}}$. Returning to the original Earth-fixed frame where the neutral wind velocity is $\vec{\boldsymbol{u}}$, (2.7) is written as

$$\vec{\boldsymbol{J}} = \vec{\boldsymbol{J}}_{\boldsymbol{i}\parallel} + \sigma_P\left(\vec{\boldsymbol{E}}_{\perp} + \vec{\boldsymbol{u}} \times \vec{\boldsymbol{B}}\right) + \sigma_H \widehat{\boldsymbol{b}} \times \left(\vec{\boldsymbol{E}}_{\perp} + \vec{\boldsymbol{u}} \times \vec{\boldsymbol{B}}\right) + \vec{\boldsymbol{J}}_{\boldsymbol{M}}\,. \tag{2.8}$$

Let us now define the transverse projection of the gradient as $\vec{\nabla}_{\perp} = \vec{\nabla} - \widehat{\boldsymbol{b}}\frac{\partial}{\partial s}$, where s is the geometric distance along the magnetic field line, e.g., starting at the bottom of the ionosphere in the southern hemisphere, and ending with a greater value at the bottom of the ionosphere in the northern hemisphere for closed field lines. Recalling that $\vec{\boldsymbol{E}} = -\vec{\nabla}\Phi$, one gets $\vec{\boldsymbol{E}}_{\perp} = -\vec{\nabla}_{\perp}\Phi$ and $\vec{\boldsymbol{E}}_{\parallel} = -\widehat{\boldsymbol{b}}\frac{\partial \Phi}{\partial s} = 0$, from where we deduce that magnetic field lines are equipotential in the ionosphere. Thus (2.8) becomes

$$\vec{\boldsymbol{J}} = \vec{\boldsymbol{J}}_{\parallel} + \sigma_P\left(-\vec{\nabla}_{\perp}\Phi + \vec{\boldsymbol{u}} \times \vec{\boldsymbol{B}}\right) + \sigma_H \widehat{\boldsymbol{b}} \times \left(-\vec{\nabla}_{\perp}\Phi + \vec{\boldsymbol{u}} \times \vec{\boldsymbol{B}}\right) + \vec{\boldsymbol{J}}_{\boldsymbol{M}\perp}, \tag{2.9}$$

where $\vec{\boldsymbol{J}}_{\parallel} = \vec{\boldsymbol{J}}_{\boldsymbol{i}\parallel} + \vec{\boldsymbol{J}}_{\boldsymbol{M}\parallel}$ is the total field-aligned component of the current, i.e., the sum of the ionospheric $\vec{\boldsymbol{J}}_{\boldsymbol{i}\parallel}$ and any possible magnetospheric component $\vec{\boldsymbol{J}}_{\boldsymbol{M}\parallel}$ arising from parallel electric fields above the auroral ionosphere, and $\vec{\boldsymbol{J}}_{\boldsymbol{M}\perp} = \vec{\boldsymbol{J}}_{\boldsymbol{M}} - \vec{\boldsymbol{J}}_{\boldsymbol{M}\parallel}$ is the transverse component of the magnetospheric current.

Now we come back to equation (2.5). Let's start from an initial situation, in which the current does not diverge, i.e., $\vec{\nabla} \cdot \vec{\boldsymbol{J}} = 0$. If then suddenly a divergence begins, the charge density resulting from (2.5) gives rise to an electric field $\vec{\boldsymbol{E}}$ through Gauss's law (2.3). However, the divergence of the current resulting from Ohm's law in reaction to $\vec{\boldsymbol{E}}$ gives rise to a charge density, which in turn creates a quick buildup of the electric field that modifies the electric fluid so that $\vec{\nabla} \cdot \vec{\boldsymbol{J}} = 0$ once again (e.g., *Kelley*, [2009]). In other words, in most practical applications the total charge does not change in a given volume, and the divergence-less equation for $\vec{\boldsymbol{J}}$,

$$\vec{\nabla} \cdot \vec{\boldsymbol{J}} = 0, \tag{2.10}$$

results in an excellent practical approximation. The same result can be directly achieved by dropping off the second term on the right hand side of (2.2), i.e., considering relatively slowly varying electric fields. Combining (2.4) and (2.10), and defining $\vec{\boldsymbol{J}}_{\parallel} = (\vec{\boldsymbol{J}} \cdot \hat{\boldsymbol{b}})\hat{\boldsymbol{b}} = J_{\parallel}\hat{\boldsymbol{b}} = J_{\parallel}\vec{\boldsymbol{B}}/B$, and $\vec{\boldsymbol{J}}_{\perp} = \vec{\boldsymbol{J}} - \vec{\boldsymbol{J}}_{\parallel}$, it follows that

$$-\vec{\nabla} \cdot \vec{\boldsymbol{J}}_{\perp} = \vec{\nabla} \cdot \vec{\boldsymbol{J}}_{\parallel} = \vec{\nabla} \cdot \left(J_{\parallel}\frac{\vec{\boldsymbol{B}}}{B}\right) = \frac{J_{\parallel}}{B}\vec{\nabla} \cdot \vec{\boldsymbol{B}} + \vec{\boldsymbol{B}} \cdot \vec{\nabla}\left(\frac{J_{\parallel}}{B}\right) = \vec{\boldsymbol{B}} \cdot \vec{\nabla}\left(\frac{J_{\parallel}}{B}\right) = B\frac{\partial}{\partial s}\left(\frac{J_{\parallel}}{B}\right), \quad (2.11)$$

where use has been made of the fact that $\vec{\nabla} \cdot (a\vec{\boldsymbol{A}}) = a\vec{\nabla} \cdot \vec{\boldsymbol{A}} + \vec{\boldsymbol{A}} \cdot \vec{\nabla}a$. Multiplying both ends of (2.11) by $1/B$, integrating the resulting equation between two arbitrary points s_1 and s_2 along the same field line, and multiplying both sides by B times the sine of the magnetic inclination at the final point s_2, $B(s_2)\sin I(s_2)$, one gets

$$B(s_2)\sin I(s_2)\int_{s_1}^{s_2}\frac{1}{B}\vec{\nabla} \cdot \vec{\boldsymbol{J}}_{\perp}ds = \sin I(s_2)\left(J_{\parallel}(s_1)\frac{B(s_2)}{B(s_1)} - J_{\parallel}(s_2)\right), \quad (2.12)$$

where $J_{\parallel}(s_1)$ and $J_{\parallel}(s_2)$ are the parallel current densities at those two points. If we now assume closed magnetic field lines and take these points to lie below the base of the conjugate ionospheres, i.e., if the integral (2.12) extends from the bottom of the conducting ionosphere in one hemisphere (s_1) to the bottom of the opposite (or conjugate) ionosphere (s_2) following the magnetic field lines, the right hand side of (2.12) becomes zero in virtue of the fact that $J_{\parallel}(s_1) = J_{\parallel}(s_2) = 0$, and it turns out that

$$\int_{s_1}^{s_2}\frac{1}{B}\vec{\nabla} \cdot \vec{\boldsymbol{J}}_{\perp}ds = 0. \quad (2.13)$$

Note that we have assumed in this reasoning that the conductivity reduces to zero below the ionosphere base, although strictly speaking weak currents flow connecting the ionosphere with the atmosphere below.

Things are different for open magnetic field lines (i.e., magnetic field lines that have a unique footpoint), where s_1 can still be situated below the ionosphere base in the concerned hemisphere. In this case, however,

$$B(s_2)\sin I(s_2)\int_{s_1}^{s_2}\frac{1}{B}\vec{\nabla} \cdot \vec{\boldsymbol{J}}_{\perp}ds = -\sin I(s_2)J_{\parallel}(s_2) = J_r(s_2), \quad (2.14)$$

where $J_{\parallel}(s_2)$ is the parallel current at a given point s_2 along the field line, and $J_r(s_2)$ its radially outward component. For reasons that will become evident later on, s_2 is more conveniently chosen to lie above the conducting ionosphere.

Note that from (2.9)

$$B(s_2)\sin I(s_2)\int_{s_1}^{s_2}\frac{1}{B}\vec{\nabla} \cdot \vec{\boldsymbol{J}}_{\perp}ds =$$

$$B(s_2)\sin I(s_2)\left(\int_{s_1}^{s_2}\frac{1}{B}\vec{\nabla} \cdot \vec{\boldsymbol{J}}_{\boldsymbol{\Phi}}ds + \int_{s_1}^{s_2}\frac{1}{B}\vec{\nabla} \cdot \vec{\boldsymbol{J}}_{\boldsymbol{u}}ds + \int_{s_1}^{s_2}\frac{1}{B}\vec{\nabla} \cdot \vec{\boldsymbol{J}}_{\boldsymbol{M}\perp}ds\right), \quad (2.15)$$

where $\vec{\boldsymbol{J}}_{\Phi} = -\sigma_P \vec{\nabla}_{\perp}\Phi - \sigma_H \hat{\boldsymbol{b}} \times \vec{\nabla}_{\perp}\Phi$ is the current tied to the electrostatic potential, and $\vec{\boldsymbol{J}}_{\boldsymbol{u}} = \sigma_P \vec{\boldsymbol{u}} \times \vec{\boldsymbol{B}} + \sigma_H \hat{\boldsymbol{b}} \times \left(\vec{\boldsymbol{u}} \times \vec{\boldsymbol{B}}\right)$ is the so-called dynamo current related to the $\vec{\boldsymbol{u}} \times \vec{\boldsymbol{B}}$ term. In integrating (2.15) in practice, advantage can be taken if we consider magnetic field lines to have a constant potential even above the conducting ionosphere. This is a reasonable approximation at middle and low latitudes, though it fails at high latitudes, as will be discussed later on.

2.4. THE IONOSPHERIC CURRENT SHEET APPROXIMATION

The following two sections are aimed at establishing basic and useful ideas on which the ionospheric electrodynamics lays, for which some simplifying assumptions are made for clarity purposes. The equations hereafter deduced, however, are not explicitly applied in our method, but it is the TIE-GCM model which carries out the computations without most of the mentioned limiting approximations.

It is possible to obtain an expression for the height-integrated ionospheric current $\vec{\boldsymbol{K}}$ (A/m) in terms of the electric field and neutral wind. Let us start with expression (2.8) for the ionosphere, where the last (magnetospheric) term on the right hand side is thus omitted. Embedded in the medium there is a perpendicular electric field $\vec{\boldsymbol{E}}_{\perp}$ and a neutral wind field $\vec{\boldsymbol{u}}$ which depend on the chosen reference frame. Because the conductivity at the bottom of this layer (below about 80 km) goes to zero, the vertical current flowing there must vanish. This is achieved by an additional charge buildup there, which produces a secondary electric field that slightly deflects our initial, purely perpendicular electric field. The resulting electric field thus has a small component along the magnetic field line, which, given the relatively large parallel conductivity σ_B, gives rise to a finite parallel current. The superposition of $\vec{\boldsymbol{J}}_{i\parallel}$ and $\vec{\boldsymbol{J}}_{i\perp} = \sigma_P\left(\vec{\boldsymbol{E}}_{\perp} + \vec{\boldsymbol{u}} \times \vec{\boldsymbol{B}}\right) + \sigma_H \hat{\boldsymbol{b}} \times \left(\vec{\boldsymbol{E}}_{\perp} + \vec{\boldsymbol{u}} \times \vec{\boldsymbol{B}}\right)$ in (2.8) must yield a purely horizontal current $\vec{\boldsymbol{J}}$ at the bottom of the ionosphere. Given the vector fields $\vec{\boldsymbol{E}}_{\perp}$ (or equivalently its horizontal projection) and $\vec{\boldsymbol{u}}$, we thus must find $\vec{\boldsymbol{J}}_{i\parallel}$ that cancels the vertical component of $\vec{\boldsymbol{J}}$.

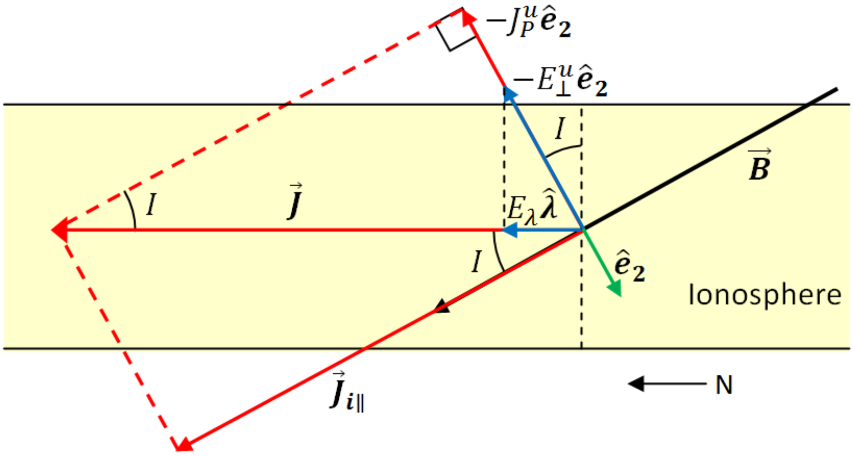

Figure 2.3. Meridional cross-section of the northern hemisphere ionosphere used to deduce the horizontal current $\vec{J}$ flowing on it as the sum of a perpendicular and a field-aligned component.

Let us consider a dipole main field outside of the equatorial zone (this latter zone would require a special treatment because of its horizontal magnetic field lines), and let $\widehat{\boldsymbol{\phi}}$ and $\hat{\boldsymbol{\lambda}}$ be the unit vectors along the eastward and northward directions, respectively. Likewise, we define a unit vector in the magnetic meridian plane $\hat{\boldsymbol{e}}_{\boldsymbol{2}} = \widehat{\boldsymbol{b}} \times \widehat{\boldsymbol{\phi}}$ with a vertically downward component. Let E_ϕ, E_λ and $-E_\perp^u$ be the projections of the perpendicular electric field $\vec{\boldsymbol{E}}_\perp$ along these directions, respectively. It is easily seen from Figure 2.3 that $E_\lambda = E_\perp^u \sin I$. Thus $\vec{\boldsymbol{E}}_\perp$ gives rise to a current $J_\perp^u$ along $-\hat{\boldsymbol{e}}_{\boldsymbol{2}}$ (i.e., with an upward component) which is the sum of a Pedersen current $J_P^u = \sigma_P E_\perp^u = \sigma_P E_\lambda / \sin I$ and a Hall current $J_H^u = -\sigma_H E_\phi$. As stated above, the parallel current is the one that cancels the vertical component of $J_\perp^u$. From Figure 2.3 it is clear that the vector sum of the parallel and the perpendicular currents, $J_\parallel \widehat{\boldsymbol{b}} - J_\perp^u \hat{\boldsymbol{e}}_{\boldsymbol{2}}$, must be $J_\lambda \hat{\boldsymbol{\lambda}} = J_\perp^u / \sin I \, \hat{\boldsymbol{\lambda}} = \left(-\sigma_H E_\phi / \sin I + \sigma_P E_\lambda / \sin^2 I\right)\hat{\boldsymbol{\lambda}}$. On the other hand, the zonal component of the current needs not be cancelled by any parallel current, so it is directly given by $J_\phi \widehat{\boldsymbol{\phi}} = \left(\sigma_P E_\phi + \sigma_H E_\lambda / \sin I\right)\widehat{\boldsymbol{\phi}}$. The total ionospheric current is thus $\vec{\boldsymbol{J}} = \left(\sigma_P E_\phi + \sigma_H E_\lambda / \sin I\right)\widehat{\boldsymbol{\phi}} + \left(-\sigma_H E_\phi / \sin I + \sigma_P E_\lambda / \sin^2 I\right)\hat{\boldsymbol{\lambda}}$. The above discussion has taken only the electrostatic field into account. However, it is straightforward to extend the formulation to include the dynamo electric field as well. In this case,

$$\vec{\boldsymbol{J}} = \left[\sigma_P\left(E_\phi - u_\lambda B \sin I\right) + \sigma_H\left(\frac{E_\lambda}{\sin I} + u_\phi B\right)\right]\widehat{\boldsymbol{\phi}} + \left[-\frac{\sigma_H}{\sin I}\left(E_\phi - u_\lambda B \sin I\right) + \frac{\sigma_P}{\sin I}\left(\frac{E_\lambda}{\sin I} + u_\phi B\right)\right]\hat{\boldsymbol{\lambda}}\,. \tag{2.16}$$

Whereas the need of a purely horizontal current (implicit in (2.16)) is strictly restricted to the bottom of the layer, we assume that this is approximately the case throughout its thickness, which allows us to integrate (2.16) between the boundaries of the conducting ionosphere following geomagnetic field lines; this view of the ionosphere corresponds to that of a thin conducting sheet. Likewise, we consider that the magnetic field vector (both its magnitude, B, and inclination, I) is constant for a given field line crossing the ionosphere, and that magnetic field lines are approximately parallel, which are reasonable assumptions outside of the equatorial zone. Since magnetic field lines are equipotential, the latter implies that the electric field vector is also constant throughout the layer thickness. The height-integrated ionospheric current $\overrightarrow{\boldsymbol{K}}$ is the projection of this field-line integral onto the radial direction, which is obtained by the product with $|\sin I|$. It can be seen that its eastward and northward components can be written in the following terms, respectively:

$$K_\phi = \Sigma_{\phi\phi} E_\phi + \Sigma_{\phi\lambda} E_\lambda + K_\phi^D, \tag{2.17}$$

$$K_\lambda = \Sigma_{\lambda\phi} E_\phi + \Sigma_{\lambda\lambda} E_\lambda + K_\lambda^D, \tag{2.18}$$

where

$$\Sigma_{\phi\phi} = |\sin I| \int_{s_a}^{s_b} \sigma_P \, ds = |\sin I| \Sigma_P, \tag{2.19}$$

$$\Sigma_{\lambda\lambda} = \frac{1}{|\sin I|}\int_{s_a}^{s_b} \sigma_P \, ds = \frac{\Sigma_P}{|\sin I|}, \tag{2.20}$$

$$\Sigma_{\phi\lambda} = -\Sigma_{\lambda\phi} = \frac{|\sin I|}{\sin I}\int_{s_a}^{s_b} \sigma_H \, ds = \frac{|\sin I|}{\sin I}\Sigma_H, \tag{2.21}$$

$$K_\phi^D = B|\sin I|\int_{s_a}^{s_b} \left(u_\phi \sigma_H - u_\lambda \sin I \, \sigma_P\right) ds, \tag{2.22}$$

$$K_\lambda^D = B|\sin I|\int_{s_a}^{s_b} \left(u_\lambda \sigma_H + \frac{u_\phi \sigma_P}{\sin I}\right) ds. \tag{2.23}$$

In the above equations, s_a and s_b, where $s_a < s_b$, are chosen to be the boundaries of the ionosphere at a given hemisphere, and s increases in the magnetic field direction. This means that in the northern (southern) hemisphere s_a and s_b are the upper (lower) and lower (upper) limits of the ionosphere, respectively. Σ_P and Σ_H are the field-line integrated Pedersen and Hall conductivities, respectively, and K_i^D are the components of the dynamo current (i.e., derived from the dynamo electric field). Note that neither the neutral wind nor the conductivities are assumed to be constant along magnetic field lines throughout the ionosphere; they indeed vary drastically with height.

2.5. CONSIDERATIONS ABOUT THE GROUND MAGNETIC SIGNATURE OF CURRENTS FLOWING IN THE IONOSPHERE AND MAGNETOSPHERE

Let us now restrict ourselves to latitudes of the northern polar cap and oval (the developments are similar for the southern counterpart) and assume $I = 90^\circ$ (i.e., radial field-lines, which is a reasonable approximation for magnetic latitudes λ above about 57˚, where $|\sin I| \geq 0.95$). In this case, (2.17) and (2.18) reduce to

$$K_\phi = \Sigma_P E_\phi + \Sigma_H E_\lambda + K_\phi^D \,,$$

$$K_\lambda = -\Sigma_H E_\phi + \Sigma_P E_\lambda + K_\lambda^D \,,$$

which can be written in vector form as:

$$\vec{\boldsymbol{K}} = \left(\Sigma_P \vec{\boldsymbol{E}} + \vec{\boldsymbol{K}}_P^D\right) + \left(-\Sigma_H \hat{\boldsymbol{r}} \times \vec{\boldsymbol{E}} + \vec{\boldsymbol{K}}_H^D\right), \tag{2.24}$$

where $\hat{\boldsymbol{r}}$ is the upward unit vector and the electric field is horizontal. The first parenthetical term on the right hand side of (2.24) is the Pedersen component of the height-integrated current, $\vec{\boldsymbol{K}}_{\boldsymbol{P}}$, the second one its Hall component, $\vec{\boldsymbol{K}}_{\boldsymbol{H}}$, and

$$\vec{\boldsymbol{K}}_P^D = B\int_{h_l}^{h_u} \sigma_P\left(-u_\lambda \hat{\boldsymbol{\phi}} + u_\phi \hat{\boldsymbol{\lambda}}\right) dh = \int_{h_l}^{h_u} \sigma_P \vec{\boldsymbol{u}} \times \vec{\boldsymbol{B}} dh \,,$$

$$\vec{\boldsymbol{K}}_H^D = B\int_{h_l}^{h_u} \sigma_H\left(u_\phi \hat{\boldsymbol{\phi}} + u_\lambda \hat{\boldsymbol{\lambda}}\right) dh = -\hat{\boldsymbol{r}} \times \int_{h_l}^{h_u} \sigma_H \vec{\boldsymbol{u}} \times \vec{\boldsymbol{B}} dh$$

are the Pedersen and Hall dynamo currents, respectively. h is height, being h_l and h_u the lower and upper limits, respectively, of the conducting layer. Note that, unlike the southern hemisphere, $dh = -ds$, $h(s_a) = h_u$, and $h(s_b) = h_l$ in the northern hemisphere when trying to deduce the above expressions from (2.22) and (2.23).

The curl of $\vec{\boldsymbol{u}} \times \vec{\boldsymbol{B}}$ is different from zero in general, but if B is assumed constant in the polar cap ionosphere and surroundings (it does not change by more than 20 %), and the neutral wind is assumed essentially horizontal and divergence-less (incompressible), then

$$\hat{\boldsymbol{r}} \cdot \vec{\nabla} \times \left(\vec{\boldsymbol{u}} \times \vec{\boldsymbol{B}}\right) = B\vec{\nabla} \cdot \vec{\boldsymbol{u}} = 0\,. \tag{2.25}$$

Let us now assume horizontally homogeneous Pedersen and Hall conductivities and calculate the vertical component of the curl of $\vec{\boldsymbol{K}}_{\boldsymbol{P}}$:

$$\hat{\boldsymbol{r}} \cdot \vec{\nabla} \times \vec{\boldsymbol{K}}_{\boldsymbol{P}} = \hat{\boldsymbol{r}} \cdot \vec{\nabla} \times \left(\Sigma_P \vec{\boldsymbol{E}} + \vec{\boldsymbol{K}}_P^D\right) = -\Sigma_P \hat{\boldsymbol{r}} \cdot \vec{\nabla} \times \left(\vec{\nabla}\Phi\right) + \hat{\boldsymbol{r}} \cdot \vec{\nabla} \times \int_{h_l}^{h_u} \sigma_P \vec{\boldsymbol{u}} \times \vec{\boldsymbol{B}} dh = 0,$$

where use has been made of the fact that the gradient is curl-free in the electrostatic term, and the vertical projection of the dynamo integral is also zero in virtue of (2.25) (with the mentioned restrictions). Note that $\hat{\boldsymbol{r}} \cdot \vec{\nabla} \times \vec{\boldsymbol{K}}_P^D = 0$ implies that $\vec{\boldsymbol{K}}_P^D$, which is a vector confined to the horizontal plane with no vertical dependence, can be written as the gradient of a scalar function which is constant with height, just like in the case of $\Sigma_P \vec{\boldsymbol{E}} = \vec{\nabla}(-\Sigma_P \Phi)$. In consequence, $\vec{\boldsymbol{K}}_{\boldsymbol{P}} = -\vec{\nabla}\tau$, where τ, designated the current potential, includes both the electrostatic and the dynamo contributions.

Now compute the divergence of $\vec{\boldsymbol{K}}_{\boldsymbol{H}}$:

$$\begin{aligned}\vec{\nabla} \cdot \vec{\boldsymbol{K}}_{\boldsymbol{H}} &= \vec{\nabla} \cdot \left(-\Sigma_H \hat{\boldsymbol{r}} \times \vec{\boldsymbol{E}} + \vec{\boldsymbol{K}}_H^D\right) = \Sigma_H \vec{\nabla} \cdot \left(\hat{\boldsymbol{r}} \times \vec{\nabla}\Phi\right) - \vec{\nabla} \cdot \left(\hat{\boldsymbol{r}} \times \int_{h_l}^{h_u} \sigma_H \vec{\boldsymbol{u}} \times \vec{\boldsymbol{B}} dh\right) \\ &= -\Sigma_H \vec{\nabla} \cdot \left(\vec{\nabla} \times \hat{\boldsymbol{r}}\Phi\right) + \hat{\boldsymbol{r}} \cdot \vec{\nabla} \times \int_{h_l}^{h_u} \sigma_H \vec{\boldsymbol{u}} \times \vec{\boldsymbol{B}} dh = 0\,,\end{aligned}$$

where use has been made of the fact that the curl is divergence-free in the electrostatic term. The dynamo integral is zero here as well for the same reasons exposed above.

Thus we see that the Pedersen current is a purely potential current, while the Hall current is a purely toroidal one if the assumptions stated above are fulfilled (constant conductances probably being the strongest one). As noted, e.g., by *Richmond* [1974] or *Fukushima* [1976], the ground magnetic effect of a current system consisting of a radial field-aligned current closing through a purely potential current in the ionosphere is zero, leaving the entire magnetic signature to the Hall current.

Performing the integral in (2.14) for a constant vertical main magnetic field yields:

$$-\int_{h_l}^{h_u} \vec{\nabla} \cdot \vec{\boldsymbol{J}}_\perp dh = -\vec{\nabla} \cdot \int_{h_l}^{h_u} \vec{\boldsymbol{J}}_\perp dh = -\vec{\nabla} \cdot \vec{\boldsymbol{K}} = -\vec{\nabla} \cdot \vec{\boldsymbol{K}}_{\boldsymbol{P}} = \nabla^2 \tau = J_r\,, \tag{2.26}$$

which (along with appropriate boundary conditions) determines the function τ (and so $\vec{\boldsymbol{K}}_{\boldsymbol{P}}$) for a given distribution of radial currents at the top of the ionosphere, J_r, as provided by the AMPERE dataset. Note that τ (or $\vec{\boldsymbol{K}}_{\boldsymbol{P}}$) does not depend on the existing conductivity distribution, which does not appear explicitly in (2.26).

It is thought that the magnetosphere behaves as a current source from the point of view of the ionosphere under certain conditions. This means that the electric voltage is set in the ionosphere as a function of both, its conductivity distribution and the field-aligned current distribution established by the magnetospheric source. In the above conditions, and assuming further that the dynamo electric field is negligible compared to the electrostatic field, which is a reasonable assumption in the high-latitude ionosphere [*Kamide et al.*, 1981], the Hall current is found to be proportional to the Pedersen one:

$$\vec{\boldsymbol{K}}_{\boldsymbol{H}} = -\Sigma_H \hat{\boldsymbol{r}} \times \vec{\boldsymbol{E}} = -\frac{\Sigma_H}{\Sigma_P} \hat{\boldsymbol{r}} \times \vec{\boldsymbol{K}}_{\boldsymbol{P}}(J_r) \,.$$

So in conclusion, the Hall current, which determines the ground magnetic signature for a constant ionospheric conductance distribution and a radial magnetic field, is directly proportional to the Hall-to-Pedersen conductance ratio, Σ_H/Σ_P. Non-uniform horizontal conductivities do not yield the same result; however, it is still expected that the ground magnetic signature increases with the local value of Σ_H/Σ_P. It is also worth to mention, as illustrated by *Fukushima* [1976], that the effect of non-radial field lines is equivalent to that produced by a magnetospheric circuit following the lines of the geomagnetic field down to the ionosphere, and then closing through the opposite radial currents to or from infinity. The relatively small ground magnetic effect of this fictitious, purely magnetospheric current system at high latitudes is superimposed to the toroidal one, strictly flowing in the ionosphere, which coincides with the Hall current in case of horizontally-uniform conductances.

3. THE LARGE-SCALE SYSTEM OF FIELD-ALIGNED CURRENTS

3.1. OVERVIEW

As mentioned above, it was *Birkeland* [1908] who, based on his measurements and observations of the auroral phenomena, proposed the existence of geomagnetic field-aligned currents connecting the Earth's upper atmosphere at high latitudes with its space environment and eventually with the Sun. However, in part because it was out of the mainstream, this theory was left aside for nearly six decades, and it was the low-altitude polar-orbiting satellite 1963 38C which first detected the existence of this large-scale current system as "transverse magnetic disturbances" [*Zmuda et al.*, 1966]. However, such disturbances were not immediately recognized as the effect of field-aligned currents, and it was *Cummings and Dessler* [1967] who first suggested its link with the current system proposed by K. Birkeland. A further ten years had to pass before the precise morphology of this current system was established, when T. Iijima and T. A. Potemra published a number of papers [e.g. *Iijima and Potemra*, 1976] based on the study of vector magnetic field measurements from the Triad satellite. The authors suggested the existence of two distinct regions in the overall pattern of the high-latitude field-aligned currents: the Region 1 (R1) and the Region 2 (R2) (Figure 3.1) [e.g., *Prölss*, 2004]. Currents in the former region flow at latitudes above about 70° magnetic latitude, and consist of an inward current flowing from the magnetosphere into the dawn side of the polar ionosphere, and an upward current towards the magnetosphere in the dusk side. R2 currents flow at somewhat lower latitudes and they have opposite polarities with respect to their R1 counterparts. This general current pattern has been found to be an almost permanent feature of the Earth's environment, though it varies depending on the magnitude and orientation of the IMF and on the amount of energy stored in the magnetosphere. Thus, the magnitude of the R1 currents typically varies between 1.6 MA during quiet times and 2.7 MA during more disturbed times, while that of the R2 currents varies between 1.1 MA during quiet times and 2.5 MA during disturbed times. It is precisely during perturbed periods, and especially during the growth phase of substorms, when the overall pattern of R1/R2 currents expands a few degrees equatorward due to the build-up of the magnetotail lobe field [*McPherron*, 1972]. Further statistical analyses of these currents and their magnetic perturbations in space have been presented by *Weimer* [2005], *Anderson et al.* [2008], *Korth et al.* [2010a], and *Clausen et al.* [2012], while *Weimer et al.* [2010] have presented an empirical model of ground magnetic perturbations at high latitudes.

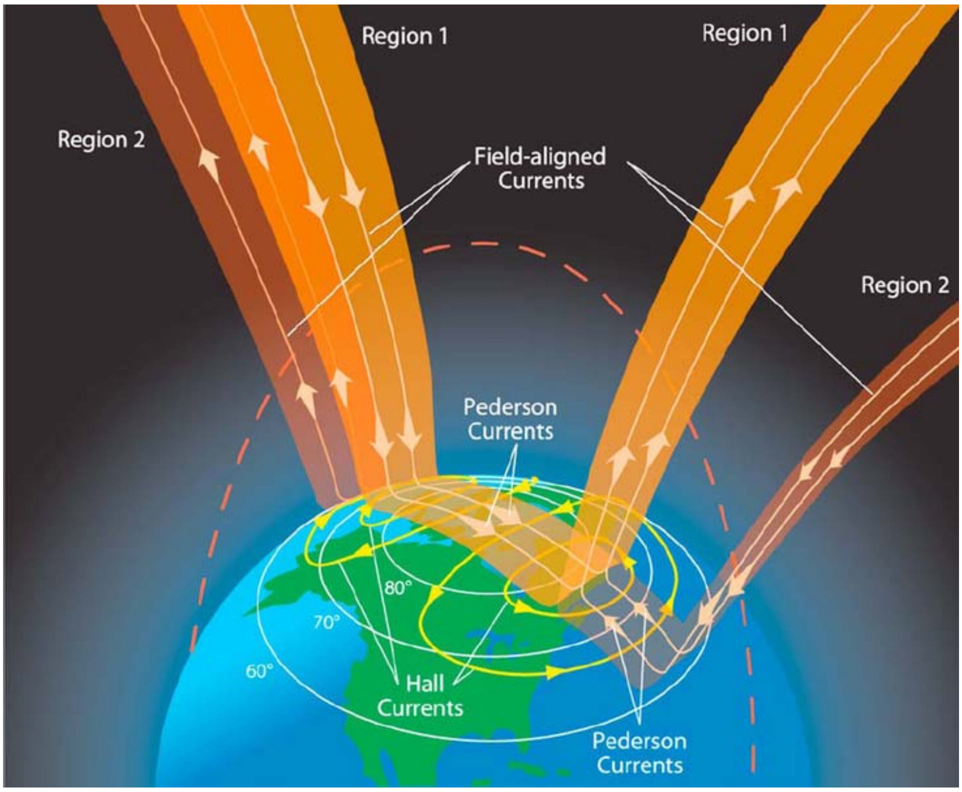

Figure 3.1. Sketch of the large-scale system of field-aligned currents with its associated Pedersen and Hall ionospheric currents flowing at high latitudes. Figure from *Le et al.* [2010] (note that Pedersen is misspelled with Pederson in the figure).

The origin of the R1 Birkeland current is intimately related to the solar wind dynamo and the Dungey cycle. The field lines of the IMF, which are nearly contained in the ecliptic plane, are “frozen in” and carried along with the solar wind plasma. As a result of the shock produced by fast solar wind flow streaming out from active regions of the Sun, these field lines are sometimes deformed upon catching up with the average wind in the interplanetary medium. Such IMF deformations, which may be assimilated to the folds undergone by a piece of cloth subject to a tangential stress, may take place in the direction perpendicular to the ecliptic, giving rise to a considerable component of the IMF in the north-south direction. Another mechanism, namely magnetic clouds released by explosive events in the Sun such as the so-called solar or coronal mass ejections (CME), have been proposed to potentially cause a north-south component of the IMF as well; in either case, when such perturbations reach the Earth’s orbit in conditions of southward IMF, this magnetic field is merged with the Earth’s one in a process known as magnetic field reconnection [*Dungey,* 1961]. Visually, somewhere in the dayside magnetopause a magnetic field line from the IMF is (re)connected with another one having its footpoints in the noon sector of the Earth’s polar caps. Such reconnection takes place as long as the two merging field lines have opposite polarities. This is indeed the case near the subsolar point, as the Earth's magnetic field is northward in that zone. The Dungey cycle starts at this point, when the solar wind plasma associated with the newly formed open magnetic field lines (one per hemisphere) undergo a dynamo process under the effects of the intense magnetic field of the Earth that leads to a dawn-dusk polarization electric field. This electric field is transferred to the polar ionosphere along the highly conducting magnetic field lines, originating the observed R1 currents by closure of the circuit in the finitely conducting ionosphere. In the magnetosphere, the R1 currents flow on the outer surface of the plasma sheet and close in the tail lobe magnetopause. As a consequence of the originated dawn-dusk electric field, ionospheric plasma undergoes convection toward the nightside polar cap by action of the $\vec{\boldsymbol{E}} \times \vec{\boldsymbol{B}}$ drift, which is associated with the migration of the open magnetic field line towards the magnetotail through the magnetotail lobe. This vision is commensurate with that of magnetic field lines frozen in the F region plasma of the ionosphere. Once in the nightside, a new reconnection takes place near the equatorial plane of the magnetotail with another open field line having its footpoint in the nightside polar cap of the opposite hemisphere, thus conserving the flux of open magnetic field lines. The closed field line so produced passes through the magnetosphere plasma sheet in the nightside equatorial plane, where the dawn-dusk electric field is also mapped. As a result of the interaction of this electric field with the northward magnetic field of the plasma sheet, a new $\vec{\boldsymbol{E}} \times \vec{\boldsymbol{B}}$ drift is produced, which brings back the reconnected field line towards the dayside magnetosphere, starting over the Dungey cycle (Figure 3.2). In its way toward the dayside, the field line footpoints pass through the two hemispherically opposite (or more appropriately, conjugate) auroral ovals, where the ionospheric electric field has a dusk-dawn polarity.

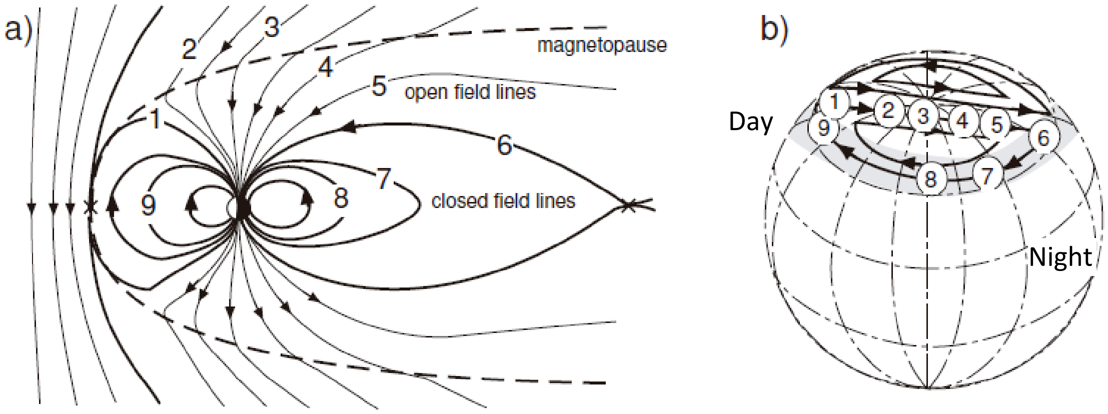

Figure 3.2. Schematic representation of the Dungey cycle, showing magnetospheric and ionospheric convection during southward IMF. Numbers in the left panel follow the progressive flow of the magnetic field lines from the dayside magnetopause to the magnetotail and back. The right panel shows the corresponding convection in the polar ionosphere. Illustration by Minna Palmroth, after *Dungey* [1961].

At high latitudes, Hall currents flow in the direction $\vec{\boldsymbol{B}} \times \vec{\boldsymbol{E}}$ (where $\vec{\boldsymbol{E}}$ is predominantly electrostatic; see equation (2.7)), just opposite to the plasma drift, i.e., sunward in the polar cap and anti-sunward at auroral latitudes. As a result, a current system is formed in the polar cap ionosphere with one vortex in its dawn sector and the other in the dusk sector, as depicted in Figure 3.1, or reversed with respect to the convection shown in Figure 3.2b. This system is a relatively persistent feature of the high-latitude ionosphere, especially during southward IMF, and its ground magnetic signature, denoted as DP2 (stemming from "disturbance polar of the second type") field [*Nishida et al.,* 1966], can be regarded as a polar diurnal variation [e.g., *Parkinson,* 1983].

R2 currents, on the other hand, have their origin in the strong dawn-dusk electric field that dominates the magnetospheric plasma sheet region, causing electric charges to flow toward the Earth. When such magnetotail plasma arrives at the vicinity of the Earth, typically below 10 R_E, it is subjected to increasing magnetic field forces that push positive charges towards dusk and negative charges towards dawn. These forces have their origin either in the increasing magnetic field gradient near the Earth (giving rise to the so-called gradient drift), or in the field lines curvature (giving rise to the curvature drift), and the resulting differential motion of charges originates a (partial) ring current. A "forbidden zone" for hot electrons convecting in from the tail is thus created in the dusk side of the plasma sheet near the Earth, while a "forbidden zone" for convecting positive charges is created in the dawn side, giving rise to a charge polarity with an associated electric field in the dusk-dawn direction in the inner magnetosphere. The charges responsible for such a polarity use to build up in the so-called Alfvén layers until the inner magnetosphere is shielded from the larger scale electric field of the plasma sheet. The Alfvén layers, with their associated electric potential, are mapped to the high-latitude zones, at somewhat lower latitudes than the R1 current sheets. The opposite polarity with respect to the nearby R1 currents thus produces the additional current of the region 2, while lower latitudes are virtually shielded from polar cap electric fields.

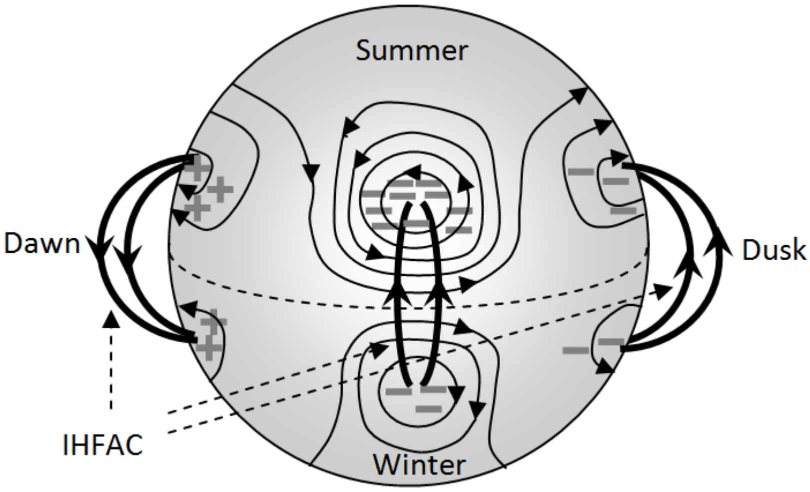

Figure 3.3. Illustration of the sunlit hemisphere during the northern hemisphere summer. During these conditions, the IHFAC system is southward at dawn, and northward at noon and dusk.

We note, however, that shielding is the asymptotic situation that would be reached in a steady state. In reality, Alfvén layers and the associated R2 currents are adjusted to the changing conditions of the solar wind forcing (which in turn is associated with the

R1 current system) within timescales of tens of minutes [*Kikuchi et al.,* 2000], and may take a few hours to complete [*Wolf et al.,* 2007]. In consequence, a transient undershielding is expected to exist shortly after an abrupt change of the IMF orientation from north to south, while an overshielding may be produced in presence of a northward turning of the IMF. During such events, relatively strong disturbance electric fields and currents have been reported to penetrate to the magnetic equator [e.g., *Kikuchi et al.,* 2000; *Kobea et al.,* 2000].

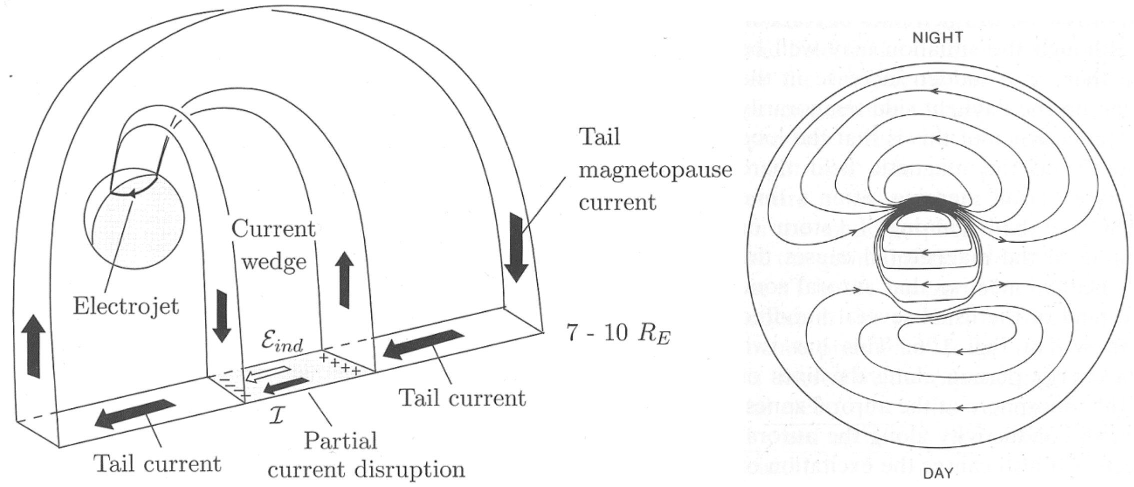

Figure 3.4. (Left) Schematic of the 3-D circuit associated with the expansion phase of a substorm, showing the current wedge and the westward electrojet flowing in the auroral ionosphere (adapted from *McPherron et al.* [1973]). (Right) DP1 or equivalent current pattern of the circuit shown in the left panel (from *Parkinson* [1983]).

Mention must be made of other systems of field-aligned currents, like the one on the dayside cusp, which flows at even higher latitudes than the R1 system [e.g., *Cowley*, 2000]. Also important for the magnetic signature produced on ground magnetometers are the so-called inter-hemispheric field-aligned currents (IHFAC), which flow between magnetically conjugate points of the midlatitude ionosphere in virtue of residual potential differences appearing as a result of an incipient charge build-up caused by the dynamo effect of the large-scale thermospheric winds [e.g., *Van Sabben,* 1966]. Such potential differences, which reach their maximum with some delay after the solstices, are thus immediately neutralized by the high conductivity in the direction parallel to the magnetic field lines, giving rise to measurable currents flowing in the inner magnetosphere, as seen in Figure 3.3. A number of additional field-aligned current systems have been proposed to explain ground magnetic signatures during disturbed conditions, some of which are outlined here: *Araki* [1977] proposed a field-aligned current system connecting the dayside magnetopause with the ionosphere that is sensitive to the solar wind pressure, thus explaining the different morphology of SCs as a function of latitude and longitude. Substorms would also have their associated field-aligned currents connected with the nightside auroral oval. The ionospheric closure of this circuit is related to the current wedge, a westward auroral electrojet observed around midnight during the expansion phase of substorms [e.g., *Atkinson*, 1967; *McPherron et al.,* 1973]. The ground magnetic signature of this 3-D current gives rise to the historical concept of DP1 (stemming from "disturbance polar of the first type") field and its associated ionospheric equivalent current system, that is, the current system entirely flowing in a thin shell at ionospheric heights that would produce the same magnetic field on the ground than the real magnetospheric-ionospheric system [e.g., *Clauer and Kamide,* 1985] (Figure 3.4).

3.2. ENERGY AND MOMENTUM TRANSFER FROM THE SOLAR WIND TO THE UPPER ATMOSPHERE

It is also useful to think in terms of energy and stress transfer from the solar wind and magnetosphere to the ionosphere [*Cowley*, 2000]. The dawn-to-dusk polarization electric field $\vec{\boldsymbol{E}}_{\boldsymbol{m}}$ generated by the solar wind dynamo process in the magnetosheath-magnetopause creates a current that closes in the polar ionosphere from dawn to dusk, originating the R1 current. Hence, the closure magnetopause current $\vec{\boldsymbol{J}}_{\boldsymbol{m}}$ flows in the opposite direction, which is also opposite in direction to the polarization electric field. As a result of this, the product $\vec{\boldsymbol{J}}_{\boldsymbol{m}} \cdot \vec{\boldsymbol{E}}_{\boldsymbol{m}}$ is negative, and this zone acts as a generator, where the energy is extracted from the solar wind plasma and conveyed to the electromagnetic field. Of course, the kinetic energy of the solar wind must be reduced in this process, as it follows from the Ampère force $\vec{\boldsymbol{J}}_{\boldsymbol{m}} \times \vec{\boldsymbol{B}}_{\boldsymbol{m}}$ (where $\vec{\boldsymbol{B}}_{\boldsymbol{m}}$ is the local magnetic field in the magnetopause), which accelerates the plasma sunward.

Let us now consider the polar ionosphere in a reference frame rotating with the Earth, where a Pedersen current $\vec{\boldsymbol{J}}_{\boldsymbol{i}}$ flows in response to an electric field $\vec{\boldsymbol{E}}_{\boldsymbol{i}}$ (see Figure 3.1). In this region, unlike the former situation, the product $\vec{\boldsymbol{J}}_{\boldsymbol{i}} \cdot \vec{\boldsymbol{E}}_{\boldsymbol{i}} > 0$, meaning that energy is extracted from the field. Now, the electric field can be written as $\vec{\boldsymbol{E}}_{\boldsymbol{i}} = \vec{\boldsymbol{E}}_{\boldsymbol{0}} - \vec{\boldsymbol{u}} \times \vec{\boldsymbol{B}}_{\boldsymbol{i}}$, where $\vec{\boldsymbol{E}}_{\boldsymbol{0}}$ is again the electric field in the frame of reference of the neutral wind, with velocity $\vec{\boldsymbol{u}}$ in our co-rotating reference frame, and $\vec{\boldsymbol{B}}_{\boldsymbol{i}}$ is the local magnetic field in the ionosphere. Part of this energy, namely an amount (per unit time and volume) $q_J = \vec{\boldsymbol{J}}_{\boldsymbol{i}} \cdot \vec{\boldsymbol{E}}_{\boldsymbol{0}} = \sigma_P E_0^2$, is dissipated in the upper atmosphere by Joule heating, so this region acts as an electric load. The remaining part of this energy equals $-\vec{\boldsymbol{J}}_{\boldsymbol{i}} \cdot (\vec{\boldsymbol{u}} \times \vec{\boldsymbol{B}}_{\boldsymbol{i}}) = (\vec{\boldsymbol{J}}_{\boldsymbol{i}} \times \vec{\boldsymbol{B}}_{\boldsymbol{i}}) \cdot \vec{\boldsymbol{u}}$, where $\vec{\boldsymbol{J}}_{\boldsymbol{i}} \times \vec{\boldsymbol{B}}_{\boldsymbol{i}}$ is the Ampère force exerted by the polar cap current to the upper atmosphere medium, generally in the anti-sunward direction. So the latter is the amount of electromagnetic energy converted into kinetic energy of the neutral wind, which tends to equalize the plasma velocity $\vec{\boldsymbol{v}}_{\boldsymbol{p}} = \vec{\boldsymbol{E}}_{\boldsymbol{i}} \times \vec{\boldsymbol{B}}_{\boldsymbol{i}}/B_i^2$. Thus, the energy is transformed from kinetic to electromagnetic in the magnetosheath-magnetopause region, and from electromagnetic to heat and kinetic in the upper atmosphere.

The energy transfer from one region to the other is described by the flux of electromagnetic energy or Poynting vector $\vec{\boldsymbol{S}} = \vec{\boldsymbol{E}} \times \boldsymbol{\Delta}\vec{\boldsymbol{B}}/\mu_0$, where $\boldsymbol{\Delta}\vec{\boldsymbol{B}}$ is the magnetic field perturbation produced by the R1 current circuit. It can be checked that $\boldsymbol{\Delta}\vec{\boldsymbol{B}}$ points sunward (anti-sunward) over the northern (southern) polar cap, so that the Poynting vector (i.e., the electromagnetic energy flux) points towards the ionosphere, as shown in Figure 3.5. Furthermore, in a steady state where the electromagnetic field energy is constant with time, and assuming that the electric field is that of the ionosphere,

$-\vec{\nabla}\cdot\vec{\boldsymbol{S}}=\vec{\boldsymbol{J}}_i\cdot\vec{\boldsymbol{E}}_i=q_J+\left(\vec{\boldsymbol{J}}_i\times\vec{\boldsymbol{B}}_i\right)\cdot\vec{\boldsymbol{u}}$, and thus the convergence of $\vec{\boldsymbol{S}}$ in an ionospheric volume equals the gain of total (thermal and mechanical) energy in that volume.

As regards the stress, momentum from the solar wind is transferred to the electromagnetic field via the Ampère force, which in turn transfers momentum from the electromagnetic field to the thermosphere.

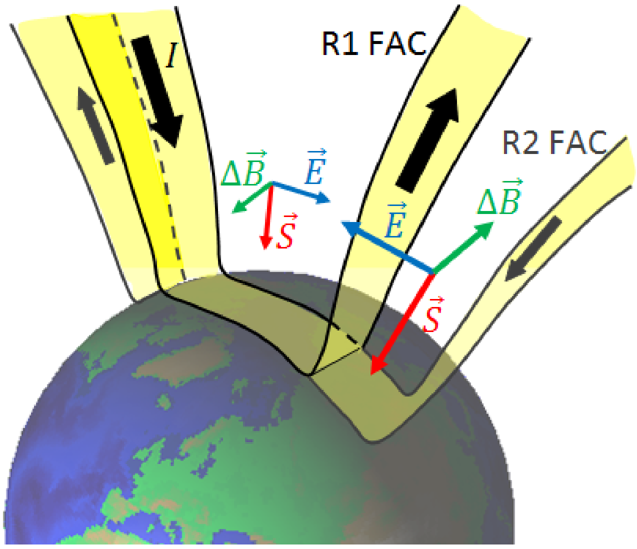

Figure 3.5. Sketch of the R1 and R2 field-aligned current (FAC) system with the associated electric ($\vec{E}$) and magnetic perturbation ($\Delta\vec{B}$) fields, and the resulting Poynting flux ($\vec{S}$) into the ionosphere.

A similar reasoning may be applied to the R2 current system, where now the closure (mostly Pedersen) current in the ionosphere flows from dusk to dawn, consistent with the direction of the electric field $\vec{\boldsymbol{E}}$. The magnetic field perturbation $\boldsymbol{\Delta}\vec{\boldsymbol{B}}$ created by the R2 current is then directed anti-sunward (sunward) in the northern (southern) hemisphere, and so the Poynting vector $\vec{\boldsymbol{S}}=\vec{\boldsymbol{E}}\times\boldsymbol{\Delta}\vec{\boldsymbol{B}}/\mu_0$ again points downward toward the auroral oval ionosphere, which again acts as an electric load dissipating a part of the energy by Joule effect and transferring another part to the neutral wind. The $\vec{\boldsymbol{J}}\times\vec{\boldsymbol{B}}$ force in the auroral zone ionosphere, however, pushes the neutral wind sunward in this case.

We indeed assumed a southward (or negative) B_Z component of the IMF in the above discussion of the R1 and R2 Birkeland currents. However, when the IMF is persistently northward in the vicinity of the Earth, mainly after a long period of low activity, a different convection pattern shows up, emerging additional vortices poleward of the region 1. This indicates the existence of new extrema in the electric potential distribution, which are inescapably linked to an additional large-scale field-aligned current system. Such current system extends over a large portion of the polar cap, and is designated NBZ (stemming from northward B_Z). It usually presents a downward current in the dusk polar cap region (connected to a relative potential maximum) and an upward current in its dawn side (connected to a relative minimum), being more intense and homogeneous in its sunlit portion. The convection pattern, which is not as clear as that for southward B_Z, is normally observed to flow sunward in the central portion of the polar cap in such conditions. Some observations [e.g. *Heelis et al.*, 1986] support the picture of a three or even four-cell pattern under these circumstances, while others favor a distorted two-cell pattern, so that sunward plasma flow is obtained in the polar cap [e.g. *Heppner and Maynard*, 1987]. Reconnection in these conditions would take place preferably somewhere in the tail lobe magnetopause, where the Earth's magnetic field is southward (and hence opposite to the IMF) rather than near the subsolar point. According to the 'frozen in' view of magnetic field lines in the plasma, the newly reconnected field line would initially be pulled sunward due to magnetic tension, and then swept into the magnetotail by the magnetosheath flow, corresponding to an anti-sunward movement of the footpoint in the polar cap ionosphere. After completing the cycle, the open magnetic field line would reconnect again with the IMF, thus keeping the open flux constant with time. It is worth to note here that the NBZ currents may well coexist with R1 and R2 currents closing at somewhat lower latitudes in the ionosphere.

We will not go into more detail here, but it is worth to note that the overall configuration and intensity of the current systems and convection patterns exposed in the above paragraphs not only vary in terms of the B_Z component of the IMF, but they also depend upon its B_Y component.

It is worth to mention before closing this section that the energy and momentum transfer to the thermosphere during magnetic disturbances, either proceeding via Joule heating or through Ampère acceleration, leads to altered thermospheric winds that produce an anomalous dynamo effect. These disturbance winds give rise to the so-called ionospheric disturbance dynamo [*Blanc and Richmond*, 1980], sometimes referred to as Ddyn, which alters the generation of electric fields and currents that extend to middle and low latitudes and can persist for up to several days after the end of the originating storm, implying magnetic disturbances of at least tens of nanoteslas in a global scale (see, e.g., *Fathy et al.* [2014] for a case study).

3.3. THE AURORAL UPPER ATMOSPHERE IN CONNECTION WITH FIELD-ALIGNED CURRENTS

The auroral oval is a ring-like region of the upper atmosphere around each polar cap where the auroral glow takes place. It encloses the footpoints of magnetic field lines connecting with the plasma sheet, a relatively dense and hot particle population centered on the mid-plane of the magnetotail that acts as a plasma reservoir. Depending on the state of the solar wind and the IMF, the plasma sheet particles undergo different processes leading to precipitation onto the auroral oval. Two types of aurorae can be distinguished from a morphological point of view: the diffuse and the discrete aurora.

The diffuse aurora is a vaguely confined, structureless luminous feature presumably produced by particles (primarily electrons) that have undergone magnetospheric convection and subsequent pitch angle diffusion into the loss cone primarily by interaction with whistler-mode waves [*Ni et al.,* 2011a, 2011b]. Diffuse aurorae are a common feature of the auroral oval not necessarily linked to a net field-aligned current, and can be observed during relatively quiet times.

The discrete aurora, on the other hand, consists of spatially confined apparitions with a more recognizable shape, showing up during magnetically disturbed conditions such as substorms. Although proton aurorae can also be observed, these are mainly produced by higher energy electrons, observed mean energies being typically in the range 2 – 20 keV [*Fridman and Lemaire,* 1980]. Such energies require additional acceleration processes of the plasma sheet particles, since the characteristic energy in this magnetospheric region barely surpasses a few keV. Acceleration is assumed to be produced by magnetic field-aligned, or parallel, electric fields, giving rise in turn to field-aligned currents [*Knight,* 1973], but also by dispersive Alfvén waves [e.g., *Chaston et al.,* 2003]. Such an acceleration process may take place somewhere along the field line, i.e., between about 10 R_E (near the central plane of the magnetotail) and 1 R_E or so above the auroral ionosphere.

Figure 3.6. Discrete auroral display. Rayed bands or "curtains" produced by the emission line of atomic oxygen at 557.7 nm wavelength. Picture taken by Rayann Elzein in Utsjoki, Finland, on January 9, 2014 (available at http://spaceweather.com).

Incident particles, upon striking the auroral ionosphere, initiate a series of processes such as scattering, collisional ionization, dissociation and excitation of the upper atmosphere particles [*Prölss*, 2004]. The energy is thus gradually transferred to the different layers of the ionosphere, penetrating deeper as the energy of the incident particles increases. Roughly speaking, the energy of 10 keV electrons, for example, is absorbed at heights about 100 km. The ionization produced at this altitude, where the neutral density is relatively high, leads to an enhancement of the Hall conductivity, which may have consequences for the electric currents flowing in this medium. In particular, an enhanced Hall conductivity enables more current to flow around the electric potential extrema (see section 2.5), producing notable magnetic fields clearly recorded by ground magnetometers below and near the auroral zone. The significance of such magnetic variations has been highlighted in the introduction of this work, especially in relation to their consequences on the human technology.

About half of the deposited particle energy is finally converted into heat in the upper atmosphere, circa one third is converted to potential chemical energy, and just about 1 % is converted to radiation [*Prölss*, 2004]; the rest is scattered back into the magnetosphere. Figure 3.6 and the front cover of this work show pictures of the light emitted by discrete auroras.

It may be worth to review at this point the different mechanisms by which energy is deposited into the high-latitude upper atmosphere. The Poynting vector flux mentioned in section 3.2 is just one way by which electromagnetic energy is dumped at the Earth's environment. Particle energy is a different one, and leads to the concept of Hemispheric Power (HP), that is, the amount of energy per unit time associated with particle precipitation incident over each hemisphere of the Earth. Both processes transfer energy from the magnetosphere to the high-latitude upper atmosphere. For the sake of completeness, it is worth to mention that other sources of energy input may exist, such as solar UV, plasma wave heating and energy transportation from the lower atmosphere, though the former two are probably the most important at high latitudes [*Rich et al.,* 1987].

4. AMPERE AND TIE-GCM

4.1. THE AMPERE MISSION

The AMPERE mission is based on the constellation of the Iridium communications satellites. Its main scientific goal is to understand the global-scale coupled electrodynamic response of the ionosphere and magnetosphere to solar wind forcing. For that purpose, it aims at providing global continuous observations of Birkeland currents with sufficient sampling cadence to chart global-scale dynamics.

Consisting of a total of 66 active vehicles flying at an altitude of 780 km, the AMPERE constellation is distributed over six circular polar orbit planes (Figure 4.1). Each space vehicle is equipped with an engineering magnetometer with 30 nT digitization resolution sampled at two possible rates, a standard mode yielding one sample every 20 s and a fast mode taking one sample every 2 s. This allows the global radial current density to be estimated every 10 minutes, commensurate with the inter-satellite time spacing in each orbit plane. The resulting data, whose density is 100 times greater than any other previous mission, are available within minutes for analysis. Data reduction and processing, provided by the Johns Hopkins University Applied Physics Laboratory Science Data Center (in Baltimore, Maryland, USA), consists of the following steps: a pre-processing that includes satellite attitude correction, where data are repaired after subtraction of the main field of the Earth; use of leading and trailing satellites to fill gaps or substitute spurious data; data interpolation with spherical harmonics to increase measurement density, thus producing vector magnetic perturbations; and derivation of the Birkeland current by means of Ampère's law [*Waters et al.,* 2001; *Korth et al.*, 2010b]. Once this process is completed, the AMPERE database (http://ampere.jhuapl.edu) provides the magnetic perturbations and the radial component of the Birkeland current densities, J_r^{AMP}. First tests were carried out during 2009, and normal acquisition started in June 1, 2010. Processed data are available in the website covering the period from January 1, 2010 to May 28, 2013, when the project expired. The initial inversions used for this study are based on spherical harmonic fits to the global magnetometer data with latitude degree of 60 (implying a minimum wavelength of 6° and a half-wavelength latitude resolution of 3°) and longitude order of 5 (36° longitude resolution). Because the inversions are not regularized and not of high degree, steps in the data sharper than the latitude resolution lead to high order ringing in the spherical harmonic fit, giving rise to spurious currents. Data are given to the final user above 30° magnetic latitude (north and south) at intervals of 2 minutes, on a regular spatial grid 1° latitude × 1 hour magnetic local time (MLT) in Altitude Adjusted Corrected Geomagnetic (AACGM) coordinates [*Baker and Wing,* 1989].

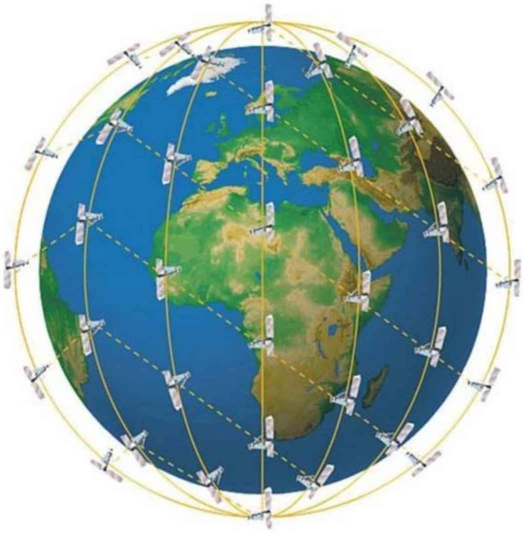

Figure 4.1. Schematic view of the distribution of the 66 satellites in the Iridium constellation holding the magnetometers of the AMPERE mission. Image credit: Iridium Communications Inc.

Scientific results of the AMPERE mission have come up in the recent years in the form of different peer-reviewed publications, e.g., on the subjects of polar cap dynamics [*Clausen et al.,* 2012; *Merkin et al.,* 2013], ionospheric electrodynamics [*Marsal et al.,* 2012], substorm dynamics [*Murphy et al.,* 2012; *Connors et al.,* 2014], or magnetosphere-ionosphere coupling [*Wilder et al.,* 2012, 2013], besides those of a more technical nature [e.g., *Knipp et al.,* 2014; *Anderson et al.,* 2008; *Korth et al.,* 2010a, 2010b].

4.2. THE TIE-GCM

The TIE-GCM model, developed at NCAR (in Boulder, Colorado, USA), is a comprehensive, first-principles, three-dimensional, non-linear representation of the coupled thermosphere and ionosphere system that includes a self-consistent solution of the low-latitude electric field [*Roble et al.,* 1988; *Richmond et al.,* 1992]. The model solves the three-dimensional momentum, energy and continuity equations for neutral and ion species at each time step, using a semi-implicit, fourth-order, centered finite difference scheme on each pressure surface in a staggered vertical grid. It has 29 constant-pressure levels in the vertical, extending from approximately 97 km to 500 km at intervals of one-half scale height, and a 5° x 5° latitude-longitude grid, in its base configuration. The electrodynamics module of the TIE-GCM is described in terms of Modified Magnetic Apex Coordinates [*Richmond*, 1995b].

Hydrostatic equilibrium, constant gravity, steady-state ion and electron energy equations, and incompressibility on a constant pressure surface are assumed throughout. The electric potential field created by combining the imposed magnetospheric potential with the low-latitude dynamo potential allows calculating ion velocities from $\vec{E} \times \vec{B}$ drifts, rather than solving the ion momentum equations explicitly. The standard operation of the TIE-GCM consists of either of two different modes to determine the high-latitude electrostatic potential: the Heelis potential model [*Heelis et al.,* 1982] uses the cross-polar cap potential (CPCP) and the hemispheric power (HP) of auroral precipitation as an input, which in turn can (both) be specified either manually or calculated using the observed 3-hourly K_p index [*Emery et al.,* 2012]; the other mode makes use of the Weimer model [*Weimer,* 2005], which uses 15-60 minute averaged solar wind density and speed as an input, as well as the IMF B_Y and B_Z components. Other geospace conditions, like the extreme ultraviolet (EUV) input, are defined by the $F_{10.7}$ index (which is the daily flux of solar radio emissions at a wavelength of 10.7 cm) by use of a proxy model. This is afterwards used to calculate the ionization, dissociation and heating rates of the upper atmosphere [e.g., *Solomon and Qian,* 2005], which will ultimately affect the conductivities and neutral winds.

Some minor species are not currently incorporated in the model, including hydrogen and helium and their ions, and argon. Despite the main physical nature of the model, several parameterizations are used in the TIE-GCM: an empirical model is used to specify photoelectron heating; the production of secondary electrons is included using an empirical model derived from two-stream calculations; the effects of mixing by gravity waves are included using an eddy diffusion formulation; CO_2 is included by specifying a lower boundary condition and assuming that it is in diffusive equilibrium; and the upper boundary conditions for electron heat transfer and electron number flux are empirical formulations.

At the low-altitude boundary, atmospheric tides are specified using the Global Scale Wave Model (GSWM) [*Hagan and Forbes*, 2002, 2003]. This is a numerical model of planetary waves and solar tides in the Earth's atmosphere from 0 - 125 km. GSWM solves for non-migrating (longitude-dependent) or migrating (sun-synchronous) waves with 2-dimensional, linearized, steady-state assumptions and a realistic zonal mean atmosphere. The forcing is due to thermospheric absorption of solar EUV radiation, absorption of solar radiation in the Schumann-Runge bands and continuum in the mesopause region, strato-mesospheric absorption of solar UV radiation, tropospheric absorption of solar infrared radiation, and tropospheric latent heating associated with deep convective activity. GSWM also includes dissipation due to ion drag, thermal conductivity, molecular and eddy diffusivity, and gravity wave drag. Both migrating and non-migrating tidal components are included for both the diurnal and semidiurnal harmonics. The GSWM practically affects the TIE-GCM neutral wind distribution.

We end this opening introduction to the TIE-GCM with a note on the huge number of scientific publications to which this model has given rise. Some of the most recent ones are cited here: *Qian et al.* [2014]; *Yamazaki et al.* [2014]; *Cnossen* [2014]; *Nguyen and Palo* [2014].

4.2.1. THE CURRENT CONTINUITY EQUATION IN THE TIE-GCM

The electrodynamics in the TIE-GCM is implemented in terms of the formalism introduced by *Richmond* [1995b]. In that article, which is crucial to the present work, the author introduces the Modified Magnetic Apex (MMA) coordinates and he makes a mathematically rigorous and extensive development of the ionospheric electrodynamics using this and the closely related quasi-dipole (QD) coordinate system on closed magnetic field lines. The definition of the MMA latitude λ_m and longitude ϕ_m will not be reproduced here (neither that of the QD coordinates); however, it is relevant to note that they are constant along the magnetic field-lines defined by the IGRF model, and they have the benefit that all of the magnetic field lines crossing a certain reference height h_R (usually chosen to lie within the ionosphere) have their corresponding values of λ_m and ϕ_m (this is not the case, for example, for the AACGM coordinates, for which description is not necessarily allowed for equatorial field lines). Taking advantage of these facts, and assuming equipotential field lines at all latitudes, the field-line integrated current continuity equation (2.15) for closed magnetic field lines takes the form:

$$\frac{1}{R^2\cos\lambda_m}\left[\frac{\partial}{\partial\phi_m}\left(\frac{\Sigma^T_{\phi\phi}}{\cos\lambda_m}\frac{\partial\Phi}{\partial\phi_m}+\Sigma^T_{\phi\lambda}\frac{\partial\Phi}{\partial|\lambda_m|}\right)+\frac{\partial}{\partial|\lambda_m|}\left(\Sigma^T_{\lambda\phi}\frac{\partial\Phi}{\partial\phi_m}+\Sigma^T_{\lambda\lambda}\cos\lambda_m\frac{\partial\Phi}{\partial|\lambda_m|}\right)\right]$$

$$=\frac{1}{R\cos\lambda_m}\left[\frac{\partial K^{DT}_{m\phi}}{\partial\phi_m}+\frac{\partial\left(K^{DT}_{m\lambda}\cos\lambda_m\right)}{\partial|\lambda_m|}\right]+J_{M\perp r}. \tag{4.1}$$

The different terms of this equation, also known as the *electrodynamo equation*, are defined in *Richmond* [1995b]; however, we give some guidelines for its interpretation here. The Σ^T_{ij} terms are the components of the conductance tensor in the direction of the local MMA coordinates represented by i, j, and are essentially proportional to field-line integrated conductivities (or equivalently, to the sum of the field-line integrated conductivities of the two conjugate ionospheres; compare with equations (2.19) to (2.21)); Φ is again the electrostatic potential, which *Richmond* [1995b] considers to be constant along magnetic field lines and symmetric about the magnetic equator, including the polar regions; defining R_E as the mean Earth's radius, $R = R_E + h_R$ is the reference radius, and can be taken as the radius of the base of the ionosphere; K^{DT}_{mi} is the integrated wind-driven current in the coordinate direction i (compare with equations (2.22) and (2.23)), and $J_{M\perp r} = J^N_{mr} + J^S_{mr}$ is the sum of upward radial currents J_{mr} at the top of the ionosphere at the northern (J^N_{mr}) and southern (J^S_{mr}) magnetic conjugate locations, representing the magnetospheric source of current associated with the divergence of transverse magnetospheric currents, $\vec{\boldsymbol{J}}_{\boldsymbol{M}\perp}$, along magnetic field lines. At midlatitudes, where the magnetospheric source is negligible, $J_{M\perp r} = 0$, and therefore $J^N_{mr} = -J^S_{mr}$, i.e., the sum of upward currents in the two hemispheres vanishes because any current flowing out of one hemisphere continues along geomagnetic field lines to flow into the opposite hemisphere. At high latitudes, the northern and southern values of J_{mr} are generally unequal, and do not cancel when summed because of magnetospheric sources.

It is interesting to show the correspondence between equations (2.15) and (4.1). It should be recalled that *Richmond* [1995b] considers closed magnetic field lines, so the left hand side of (2.15) vanishes in virtue of (2.13). The left hand side of (4.1) corresponds to the term containing the electrostatic current $\vec{\boldsymbol{J}}_{\Phi}$ on the right hand side of (2.15), and represents the convergence of the ionospheric currents driven by the electric fields (summed over both hemispheres). The first term on the right hand side of (4.1) corresponds to the term containing the dynamo current $\vec{\boldsymbol{J}}_{\boldsymbol{u}}$ in (2.15), and represents the divergence of the wind-driven currents (again the sum of both hemispheres). The last term $J_{M\perp r}$ in (4.1) corresponds to the transverse magnetospheric current term in (2.15).

The continuity equation in the case of open magnetic field lines deserves special attention. In this case, the formalism introduced by *Richmond* [1995b] is no longer valid, in part because the MMA coordinates are not defined for open magnetic field lines. However, they can still be defined at each point as in the case of closed magnetic field lines, i.e., considering the description provided by the IGRF model, which is a good approximation at any latitude as we approach the Earth. In this case, the integration of (2.15) cannot be performed between conjugate points; instead, the limits s_1 and s_2, which for open magnetic field lines are named s'_l and s'_u respectively, will be chosen to lie at the lower and upper boundaries, respectively, of the conducting ionosphere (note that for low-latitude magnetic field lines that do not reach to the top of the conducting ionosphere, s'_u is defined to be the value of s' at the field-line apex). Obviously, the integral containing the divergence of the magnetospheric term $\vec{\boldsymbol{J}}_{\boldsymbol{M}\perp}$ in (2.15) is zero between the ionosphere boundaries s'_l and s'_u, and the left hand side of (2.15) is $J_r(s'_u)$ in virtue of (2.14). Thus (4.1) takes the form

$$\frac{1}{R^2\cos\lambda_m}\left[\frac{\partial}{\partial\phi_m}\left(\frac{\Sigma_{\phi\phi}}{\cos\lambda_m}\frac{\partial\Phi}{\partial\phi_m}+\Sigma_{\phi\lambda}\frac{\partial\Phi}{\partial\lambda_m}\right)+\frac{\partial}{\partial\lambda_m}\left(\Sigma_{\lambda\phi}\frac{\partial\Phi}{\partial\phi_m}+\Sigma_{\lambda\lambda}\cos\lambda_m\frac{\partial\Phi}{\partial\lambda_m}\right)\right]$$
$$=\frac{1}{R\cos\lambda_m}\left[\frac{\partial K^D_{m\phi}}{\partial\phi_m}+\frac{\partial\left(K^D_{m\lambda}\cos\lambda_m\right)}{\partial\lambda_m}\right]+J_{mr} \qquad (4.2)$$

as expressed in *Richmond*'s [1995b] formalism, where Σ_{ij} and K^D_{mi} are the hemispheric versions of Σ^T_{ij} and K^{DT}_{mi}, respectively (see definitions (5.13) to (5.20) in *Richmond* [1995b]), and the term J_{mr} plays the role of $J_r(s'_u)$.

Note that, though we have inferred equations (4.1) and (4.2) from (2.15) for the sake of comprehensibility, this is not a straightforward operation, and the definitions given by *Richmond* [1995b] must be rigorously followed to achieve the exact formulation. This applies, for example, to the s coordinate: unlike what we have introduced in section 2.3 as the s coordinate (whose value increases in the magnetic field direction), s' (as introduced in the previous paragraph) increases *upward* following the magnetic field lines in this formulation, reaching its maximum in the field-line apex, which implies $s'_l < s'_u$ in both hemispheres. In more general terms, *Richmond*'s [1995b] formulation and, by extension, that in (4.1) and (4.2), accounts for the non-dipolar form of the real geomagnetic field, for what the IGRF approximation is used. Thus, the conductivity and current parameters in (4.1) and (4.2) include scale factors that involve the non-dipolar field distortions, as can be checked by comparing equations (2.19) to (2.23) with equations (5.13) to (5.20) of *Richmond* [1995b]. This also applies to J_{mr}, which differs somewhat from the true radial current density $J_r(s'_u)$ at the point s'_u

when the field is not a perfect dipole. All of these considerations must be taken into account in the deduction of (4.1) and (4.2) from (2.15).

Note, finally, that equation (4.1) applies to one single hemisphere of the Earth, as one hemisphere is folded into the other in virtue of the fact that this is a field-line integrated equation. On the contrary, (4.2) applies to each and every point of the Earth's surface where the MMA coordinates are defined.

4.2.2. THE STANDARD TIE-GCM

A simplified flowchart of the electrodynamics of the standard TIE-GCM can be found in Figure A.1a of appendix A. As stated above, the electrodynamics module of the model uses *Richmond*'s [1995b] formulation, which is valid for the closed magnetic field lines defined by the IGRF model. This implies an electrostatic potential Φ which is hemispherically symmetric all the way from the magnetic equator through the poles. However, although this is an excellent approximation at low and middle latitudes, it fails at high latitudes, where the magnetic field topology is much more complex and dependent on the solar wind conditions, especially for field lines that pass through the outer magnetosphere, or in the presence of a strong IMF B_Y component [e.g., *Heppner,* 1972; *Siscoe et al.,* 2001; *Weimer,* 2005]. To get round this, the high-latitude potential in the standard TIE-GCM is determined by one of the two modes mentioned at the beginning of section 4.2, i.e., either the Heelis or the Weimer mode. We will be exclusively concerned ourselves with the former here, as the present work is based on it. Thus in the Heelis mode, the time-varying solar $F_{10.7}$ radio flux index and the K_p index are input to the TIE-GCM. The former index is used to parameterize the solar radiation, which is essential to the chemistry and dynamics of the upper atmosphere, while the latter is used to parameterize both the auroral HP [*Zhang and Paxton*, 2008] and the CPCP of the *Heelis et al.* [1982] convection pattern at absolute magnetic latitudes above 75˚. The above indices essentially affect global conductivities (Σ_{ij}) and wind distributions ($\vec{\boldsymbol{u}}$ and hence K_{mi}^{D}) from the electrodynamics point of view, which are self-consistently calculated by the model. The effect of neutral winds is ignored at magnetic latitudes above 75˚ for purposes of computing the electric field, for which the *Heelis el al.* [1982] model provides the ion convection pattern (i.e., the $\vec{\boldsymbol{E}} \times \vec{\boldsymbol{B}}$ drift) and hence the electric field. Below 60˚ magnetic latitude, the electric field is calculated by the dynamo model (4.1) assuming divergence-free transverse magnetospheric currents, i.e., $J_{M\perp r} = 0$. Between 60˚ and 75˚ magnetic latitude (north and south), there is a smooth transition between the dynamo solution and the high-latitude solution imposed by the *Heelis et al.* [1982] model. As mentioned above, migrating tides are specified at the low-altitude boundary of the thermosphere using the GSWM.

Once in possession of the electrostatic potential at each point of the ionosphere, along with the conductivity and wind distributions, the electrodynamics of this medium is determined by the model. In particular, the ionospheric and field-aligned currents can be computed at each point with the help of the generalized Ohm's law (see section 2.3). Such currents in turn produce a perturbation magnetic field whose value can be modeled above and below the ionosphere. Comparison of these theoretical values with real observations can then be used to validate the model. In particular, we will be interested in the ground magnetic signatures of these currents.

The TIE-GCM gives the values of J_{mr}, $K_{q\phi}$ and $K_{q\lambda}$ as an output, which we can identify with the field-aligned current at the top of the ionosphere, and the local magnetic east and north components, respectively, of the height-integrated horizontal currents $\vec{\boldsymbol{K}}$ flowing in the ionosphere (see *Richmond* [1995b] again for the appropriate definitions, which are tied to the QD coordinates).

4.2.3. CALCULATION OF GROUND MAGNETIC SIGNATURES

The ground magnetic signature of the obtained currents, i.e., of those strictly in the ionosphere and of those flowing along magnetic field lines, is calculated following the method presented by *Richmond* [1974]. Although the code used to calculate the ground magnetic perturbations is indeed separated from the standard TIE-GCM, the procedure followed is outlined below.

Treating the height-integrated ionospheric currents as flowing in a thin shell at 110 km altitude, this method calculates the equivalent current function, the magnetic potential, and the external component of the magnetic perturbation; see also *Richmond and Maute* [2014] for a more detailed description. In calculating the equivalent current function, the MMA coordinates are treated as though they are dipole coordinates, so that field-aligned current can be treated as though it flows along dipolar field lines, allowing the algorithm of *Richmond* [1974] to be used. The symmetric field-aligned current, which is defined as the part of the current that flows in the same sense (i.e., upward or downward) in the two conjugate ionospheres, is treated as though it flows to the field-line apex, from where it flows radially to or from infinity. The antisymmetric component, on the contrary, is defined as the part of the field-aligned current flowing between the two conjugate ionospheres. No magnetospheric currents perpendicular to the dipolar field lines are considered (e.g., ring current, Chapman-Ferraro current, tail current) other than these.

The conductive nature of the Earth is also taken into account, which is approximated by a sphere of perfectly conducting material below a certain depth, and a perfect insulator above; this differs from other models, like the Comprehensive Model version 4 (CM4) [*Sabaka et al.*, 2004], which considers a 1-D (i.e., radially varying) finite Earth conductivity, or the 3-D model used by *Kuvshinov and Utada* [2010].

Thus in summary, at the high latitudes (above 70˚) the electric field is defined by the K_p-dependent Heelis (electric) potential model. At latitudes below 60˚ magnetic latitude the standard TIE-GCM solves equation (4.1) for the electrostatic potential Φ, using the values of the conductivities Σ_{ij} and dynamo terms K_{mi}^{D} calculated by the model, which implicitly depend on the input $F_{10.7}$ index. Use is also made of different boundary conditions, such as the one provided by the Heelis potential model at high latitudes or the GSWM model at the low-altitude boundary. The term $J_{M\perp r}$, associated with the divergence of transverse magnetospheric currents, is set to zero below 60˚ magnetic latitude for the reasons exposed above. Once the electric field is determined in a global scale, along with the conductivities and dynamo terms, the current distribution in the ionosphere and above is computed by use of Ohm's law. Finally, a separate module that uses the dipole approximation allows calculating the ground magnetic signature of the global distribution of ionospheric and field-aligned currents.

5. THE AMPERE-DRIVEN TIE-GCM

This chapter is devoted to identifying the author’s contribution to the modeling of the near-Earth space environment, which essentially consists in the modification of the standard TIE-GCM model to receive the AMPERE observational input and in making the model conductivities consistent with it. The terms “modified TIE-GCM” or, interchangeably, “AMPERE-driven TIE-GCM” will be generally used as opposed to “standard TIE-GCM”. Simplified flowcharts of the electrodynamics of the AMPERE-driven TIE-GCM can be found in Figure A.1b and A.1c of appendix A.

Unlike the standard model, the modified TIE-GCM solves the electrodynamo equation (to which equations (4.1) and (4.2) will be referred) for the electrostatic potential Φ at *all* latitudes essentially using the radial currents given by the AMPERE dataset [see *Richmond and Maute*, 2014]. The conductances Σ_{ij} and wind-driven currents K_{mi}^{DT}, on the contrary, are calculated as in the standard version if we limit ourselves to the results presented by *Marsal et al.* [2012] and *Blanch et al.* [2013]; however, the conductivities have recently been made consistent with geomagnetic field-aligned currents at auroral latitudes, where upward currents are associated with higher conductivities due to electron precipitation (the details of this modification have not been published, and will be presented here for the first time; however, some results have been presented in a Geospace Environment Modeling (GEM) workshop, in an Air Force Office of Scientific Research (AFOSR) workshop, and in an assembly of the Committee on Space Research (COSPAR) and are available in the internet; e.g., *Marsal et al.* [2013], *Richmond et al.* [2014], and *Altadill et al.* [2014]). As in the standard model, once the electrostatic potential has been determined at each point of the ionosphere, the remaining electrodynamic quantities, such as the ionospheric currents and associated magnetic field perturbations, are derived from it. In this work, the magnetic signature produced by these currents on the ground will be compared with contemporaneous measurements of the ground-based magnetometer network, thus serving as the main validation means. A second means of validation is provided by comparing our modeled conductance distribution with that yielded by two independent models that account for the effects of precipitation associated with field-aligned currents.

5.1. THE AMPERE INPUT

The radial currents given by the AMPERE dataset, J_r^{AMP}, are calculated at the satellite height (about 780 km) essentially using Ampère's law, i.e., equation (2.2), with the second term on the right hand side equal to zero. Such currents are afterwards mapped at an altitude of 120 km using the AACGM coordinates (B. J. Anderson, personal communication, 2011). However, *Marsal et al.* [2012] and *Blanch et al.* [2013] essentially used the sum of the North and South AMPERE radial currents at conjugate points, $J_r^{AMP,N} + J_r^{AMP,S}$, as an approximation for the quantity $J_{M\perp r}$ appearing in (4.1). Likewise, the open field-line version of the electrodynamo equation, (4.2), was alternatively solved in these articles basically using J_r^{AMP} as an approximation for the term J_{mr}. In the three paragraphs below we analyze the assumptions implicit in these approximations and give arguments to justify them:

First of all, the TIE-GCM uses MMA coordinates and a reference height h_R = 90 km, which implies that the value $R = R_E$ + 90 km should be implicit in the calculation of the different quantities appearing in the electrodynamo equations, including J_{mr}. This height difference of 30 km between the height at which the AMPERE currents are mapped (120 km) and the value h_R (= 90 km) used by the TIE-GCM indeed makes no practical difference (below 2 %) in terms of the geometrical factor affecting the value of the radial component of the field-aligned current.

Secondly, in the above articles the AACGM coordinates used by AMPERE were identified with the MMA coordinates used in the TIE-GCM. Despite these two sets of coordinate systems are defined in a different fashion, this assumption implies a maximum difference of about 0.3° in latitude and 0.5° in longitude in the whole polar cap, increasing as we move towards lower latitudes. Taking into account that the main currents flow at the high-latitude ionosphere, and given the limitations imposed by the AMPERE dataset itself (e.g., resolution, assumptions and mathematical treatment made by the AMPERE team to obtain the field-aligned currents), this identification also turns out to be sufficiently good.

Thirdly, whereas the use of J_r^{AMP} instead of J_{mr} is quite a reasonable approximation in the northern hemisphere, it implies a J_{mr} value underestimated by as much as 30 % in the South Atlantic anomaly sector of the southern hemisphere, as the magnetic field significantly differs from the dipole one in this zone (we recall that J_{mr} accounts for the non-dipolar field, whereas J_r does not, as stated in section 4.2.1).

Although the overall error associated with the abovementioned assumptions should not be substantial, in an improvement implemented after the publication of *Blanch et al.* [2013] (the results are used in the present work but have not been published) the appropriate definitions have been applied, and the AMPERE currents J_r^{AMP} have been properly converted to J_{mr} using a reference height of 90 km instead of 120 km, thus overcoming the three approximations above. Let us denote J_{mr}^0 the radial field-aligned currents obtained after this first step.

Note, finally, that there is a difference between this reference height and the altitude of 110 km chosen for the thin-shell current layer in the method by *Richmond* [1974] used to calculate the ground magnetic signature of the modeled currents (see section

4.2.3). The quantities output by the TIE-GCM, such as the ionospheric height-integrated horizontal currents $\vec{\boldsymbol{K}}$, will thus eventually be referred to an altitude of 90 km. However, no significant error is produced in assigning the resultant vector $\vec{\boldsymbol{K}}$ an altitude of 110 km instead of the genuine height of 90 km. Yet, it is worth to remark that the altitude of 110 km is more adequate, as it is representative of Hall currents, which tend to dominate ground magnetic perturbations associated with the equatorial and (more importantly for this work) auroral electrojets. One can even evaluate the uncertainty associated with this height assignment: consider, first of all, that the AMPERE currents have a latitude resolution of 3°, meaning that they cannot capture horizontal features of scale smaller than $\lambda = 680$ km in the ionosphere (which corresponds to a minimum latitude wavelength of 6° corresponding to the spherical harmonic analysis carried out by the AMPERE team). The vertical scale length of variation of magnetic perturbations for such features is $\lambda/2\pi = 108$ km, meaning that a realistic uncertainty of ± 10 km in the assignment of the thin-shell current height would imply a maximum relative uncertainty of 10 % for the calculated ground magnetic perturbations.

The field-aligned currents J_{mr}^0 thus obtained after this first step are afterwards linearly interpolated to the MMA grid used by the TIE-GCM. As noted above, the AMPERE currents show a spurious ringing effect as a result of the spherical harmonic analysis used by the AMPERE team to fit the data, giving rise to unrealistic currents that stand out at midlatitudes. Finite field-aligned currents flowing into zones where the modeled ionospheric conductance is low (especially at nighttime midlatitudes) would give rise to unrealistic electrostatic potentials being built-up in order to dispatch these incoming currents. Just to avoid such unlikely electric potentials, the AMPERE currents in *Marsal et al.* [2012] and *Blanch et al.* [2013] are suppressed where the hemispheric field-line integrated Pedersen conductivity is lower than 2 S. In order to avoid numerical problems in the TIE-GCM, a correction is also applied to the resulting data so as to balance the globally integrated upward and downward currents. The correction applied is proportional to the field-line integrated Pedersen conductivity, $\Sigma_{\phi\phi}/|\sin I_m|$, and the absolute value of J_{mr}^0:

$$J_{mr,i} = J_{mr,i}^0 - \frac{\Sigma_{\phi\phi,i}}{|\sin I_{m,i}|} |J_{mr,i}^0| \frac{\oint J_{mr}^0 d\Omega}{\oint \frac{\Sigma_{\phi\phi}}{|\sin I_m|} |J_{mr}^0| d\Omega} , \qquad (5.1)$$

where the index i refers to each point of the TIE-GCM grid, I_m is approximately the magnetic inclination at the reference height h_R (see *Richmond* [1995b] for the exact definition), $d\Omega$ is the differential solid angle, and the integrals (strictly speaking discrete sums within the model) enclose the Earth. The use of (5.1) ensures that the surface integral of J_{mr} around the Earth is zero, so that no net radial currents flow. Making the correction proportional to the Pedersen conductance minimizes the effects on the electrostatic potential distribution. On the other hand, making it proportional to the absolute value of J_{mr}^0 prevents the existence of extended high-conductivity zones (especially in the dayside midlatitudes) with originally negligible (or zero) field-aligned currents where the corrected value J_{mr} would otherwise be an unrealistic constant non-zero value.

5.2. THE OPEN FIELD-LINE VERSION OF THE ELECTRODYNAMO EQUATION

Once the corrections described in the previous section have been made, *Marsal et al.* [2012] make use of the sum of the J_{mr}^{N} and J_{mr}^{S} conjugate values to obtain $J_{M\perp r}$ in the closed field-line version of the electrodynamo equation, (4.1), which is solved for the electrostatic potential Φ. As in the standard version, the quantity Φ then yields the global currents perpendicular to the geomagnetic field in the ionosphere (where $\vec{\boldsymbol{J}}_{\boldsymbol{M}\perp} = 0$) using Ohm's law (equation (2.9)). The convergence of those currents, integrated along geomagnetic field lines between the bottom and the top of the ionosphere, should then give the original (or rather the *corrected* as explained in section 5.1) AMPERE field-aligned currents, provided the magnetic field topology, the imposed conductivity and wind distributions, and the assumption of hemispherically symmetric potentials are all realistic. This can indeed be considered as a consistency test of the method.

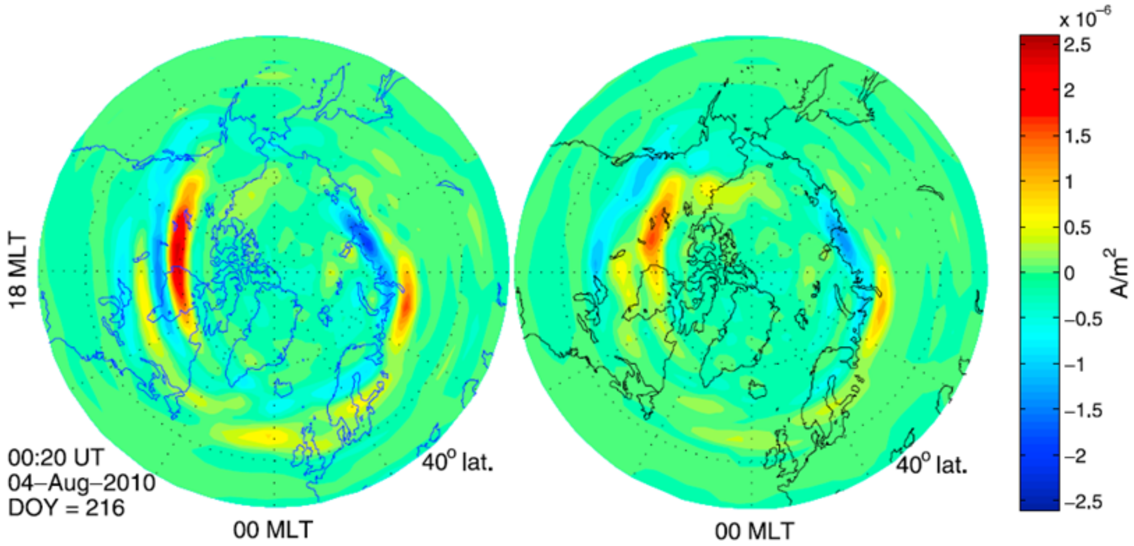

Figure 5.1. (Left) Northern hemisphere azimuthal equidistant projection (above 40° magnetic latitude) of the original AMPERE radial field-aligned currents, J_{mr} ([A/m^2], positive upward), mapped at 90 km height for the magnetically disturbed day August 4, 2010, at 00:20 UT. (Right) Radial currents as output by the TIE-GCM after applying the potential solver and calculating the convergence of the resulting ionospheric currents. QD coordinates [*Richmond*, 1995b] are used in both panels.

Figure 5.1 presents an azimuthal equidistant projection map centered on the QD North pole comparing the radial current distribution, J_{mr}, given by the AMPERE dataset (after the process explained in section 5.1) and the same quantity as output by the TIE-GCM for the disturbed day August 4, 2010, at 00:20 UT. Note that in this and other similar figures along this work, local noon is at the top. As mentioned above, the ability of the model to reproduce the original AMPERE data is a first test of its feasibility. In general, both data sets compare well, though in some sectors the model (right panel) is observed to smooth out the original pattern (left panel). The greatest differences are observed at the afternoon sector of the auroral oval, where the TIE-GCM underestimates by 30 % the J_{mr} local maximum corresponding to the upward R1 field-aligned current. The original nearby R2 field-aligned current has also been eroded. A detailed analysis of the reasons for those discrepancies reveals that the peak upward and downward AMPERE field-aligned current is not located exactly at the same conjugate points of the northern and southern hemispheres, which biases the sum $J_{mr}^{N} + J_{mr}^{S} = J_{M\perp r}$ used as an input to the model. This mismatch could partly be due to field-line distortion in the magnetosphere, especially during disturbed periods (this effect is ignored by the TIE-GCM, which uses the IGRF to trace the field lines). The limited spatial resolution of the AMPERE field-aligned current data, which is 3˚ in latitude, could also play a certain role on that effect, since it is sometimes comparable to the latitudinal width of the R1 and R2 field-aligned current bands (contrast this with the 0.7˚ latitude spacing used by the TIE-GCM at auroral latitudes). Finally, we cannot exclude the possibility that the conductivity and neutral wind distributions imposed by the TIE-GCM, as well as the assumption of hemispherically symmetric potentials, are not sufficiently realistic.

In order to overcome the difficulty associated with mismatched locations of northern and southern peak Birkeland currents, and also to overcome the limitation of hemispherically symmetric potential Φ all the way from the magnetic equator through the poles (which, as stated, loses validity at high latitudes), *Marsal et al.* [2012] decided on assaying an alternative solution inspired on the open field-line version of the electrodynamo equation. Such open field-line version would demand solving (4.2) on the whole Earth at once, instead of solving (4.1). However, the TIE-GCM is not designed for that purpose, but it takes advantage of the symmetric potential assumption made by *Richmond* [1995b] to fold the two hemispheres into one, giving rise to a field-line integrated equation. To partially avoid this constraint we proceeded in the following way: we copied the distributions of field-aligned currents (J_{mr}), conductances and wind-driven terms at magnetic latitudes above 61˚ (north or south) to the conjugate latitudes of the opposite hemisphere. At absolute magnetic latitudes below 58˚, we kept the original distributions of those quantities at both hemispheres. A transition zone was considered between 58˚ and 61˚ magnetic latitude (north and south), allowing for a smoothed connection of the field-aligned current, conductance and wind distributions between the middle and high latitudes. Once in possession of the new distributions, the normal procedure explained at the beginning of this section (i.e., using equation (4.1)) was followed. This allows that, at least at high latitudes where the distributions are copied to the conjugate hemisphere, equation (4.1) be indeed twice equation (4.2), and thus (4.2) be also valid.

The above method yields two possible solutions, depending on which hemisphere is being copied into the other: we will refer to the “NH solution” if the northern hemisphere high-latitude distributions are copied to the southern hemisphere, and “SH solution” in the opposite case. When we are interested in an electrodynamic quantity in the Northern hemisphere, we look at the NH solution, and vice versa. When the NH and SH solutions are combined for a given instant of time to obtain the global solution at that time, this procedure allows asymmetric potentials in the two hemispheres and an improved fit to the AMPERE field-aligned current. The hemispheric asymmetry thereby allowed in the potential may be realistic at high latitudes, but it is unrealistic at middle and low latitudes, where the conjugate hemispheres are electrically tightly coupled. So at some extent, an important constraint has been left behind in this process. This is explained by the following fact: although at middle and low latitudes (below 58˚) we are preserving the original hemispheric sum of the three quantities: field-aligned currents, conductances, and wind-driven terms, the electric potential does not necessarily coincide at these latitudes for the NH and SH solutions, since the high-latitude boundary conditions for Φ differ from each other. Fortunately, the resulting asymmetry is generally small at these lower latitudes and this problem is usually not important for the main high-latitude electrodynamic features of interest in this study.

It is worth to mention here that the comparison between modeled and original AMPERE radial field-aligned currents (as it was shown in Figure 5.1) is no longer meaningful at high latitudes when this alternative method is applied, since both patterns are the same by definition. This is because a forward modeling would be implemented over the results of a previous inverse method, thus yielding the original input if the mathematical implementation of the TIE-GCM is correct (which is definitely the case).

In order to distinguish the electric potential solution obtained using this alternative method from the one obtained using the method explained in the first part of this section (i.e., that corresponding to equation (4.1)), we will refer to the latter as "NS solution", as the northern and southern hemispheres are solved simultaneously when the original method is used. To recap, we have either the NH and SH solutions, or the "normal" NS solution. We advance that, despite the expected improvement to the modeled polar electrodynamics by allowing each hemisphere to have a separate pattern of electric potential, this alternative solution (i.e., NH and SH solutions as an alternative to the simultaneous or NS solution) does not always yield a better comparison between observed and modeled magnetic perturbations at the ground.

5.3. THE AURORAL SPECIFICATION IN THE AMPERE-DRIVEN TIE-GCM

An important step forward has been made, at least from a theoretical point of view, since the publication of the articles from *Marsal et al.* [2012] and *Blanch et al.* [2013]. It consists in the introduction of auroral conductivities which are consistent with AMPERE field-aligned currents in the TIE-GCM model; more specifically, zones of enhanced upward current as specified by the AMPERE data, which are mainly due to energetic precipitating electrons accelerated by parallel electric fields, are made consistent with zones of enhanced conductivity. Figure 5.2 illustrates the basis of this process, the details of which are presented below. This is not the first time that a relationship between upward field-aligned current and ionospheric conductivity is introduced [e.g., *Mishin et al.*, 1986; *Marklund et al.*, 1987, 1988]. *Blomberg and Marklund* [1988], for example, examined the effects of a coupling that is essentially proportional to the upward current density on the high-latitude convection pattern, and found considerable modification in the rotation of the entire potential pattern due to this fact.

The present standard version of the TIE-GCM specifies variable energy fluxes associated with precipitating electrons in the auroral oval as a function of the geophysical indices at the time for which the model is run, in particular of the HP, which in turn is deduced from the K_p activity index [see details in *Roble and Ridley*, 1987]. The characteristic energy (which is defined as half the mean energy) of the precipitating electrons in the standard TIE-GCM, however, does not depend on the activity level, and it simply varies gradually in longitude from a constant value of 1.5 keV in the dayside auroral oval and a constant value of 2 keV in its nightside. In this work, we have considered the specification of the aurora given by *Zhang and Paxton* [2008]. In their article, these authors provide empirical formulations on the energy flux and mean energy of precipitating electrons at each point of the top of the ionosphere as a function of AACGM colatitude, MLT and K_p index, based on a number of global far ultraviolet (FUV) observations made by the Global Ultraviolet Imager (GUVI) instrument mounted on the Thermosphere Ionosphere Mesosphere Energetics and Dynamics (TIMED) satellite. The approach considered in this work consists in identifying Zhang & Paxton's specification with the base diffuse aurora in the TIE-GCM. (Note that we use the text Zhang & Paxton to refer to *Zhang and Paxton* [2008].)

On the other hand, the discrete aurora specification in this work is based on the paper from *Knight* [1973], whose results have been confirmed by several works [e.g., *Korth et al.,* 2014]. That author considers a magnetic field line from the high-latitude auroral zone to the magnetospheric neutral sheet along which the magnetic field strength decreases monotonically. A Maxwellian steady state solution is assumed to exist in the plasma sheet region, and the thermoelectric effect is considered with thermal plasmas at different temperatures at either end of the magnetic field line, i.e., the ionosphere and the plasma sheet. A monotonically decreasing potential difference is then added between these two ends. This provides the computation of the electron flux from one end to the other, which in turn gives rise to a theoretical value of the field-aligned current. In conclusion, the field-aligned current density is given as a function of the potential difference between the plasma sheet and ionospheric ends of the field line. The given formulation also depends on the electron temperature, T, and the electron number density, N, as well as on the ratio β of the magnetic field strength at the ionosphere (B_I) to plasma sheet (B_S) bases (i.e., $\beta \equiv B_I/B_S$), as expressed in the following equation:

$$\begin{aligned} J_{\parallel} = e \Bigg\{ & N_S \sqrt{\frac{kT_S}{2\pi m_e}} \left[\beta - (\beta - 1)\mathrm{e}^{-\frac{eV}{kT_S}\frac{1}{\beta-1}}\right] \\ & - N_I \sqrt{\frac{kT_I}{2\pi m_e}} \left[\beta - (\beta - 1)\mathrm{e}^{-\frac{eV}{kT_I}\frac{1}{\beta-1}}\right] \mathrm{e}^{-\frac{eV}{kT_I}} \Bigg\}, \end{aligned} \tag{5.2}$$

where $J_{\parallel}$ is the resulting upward field-aligned current at the top of the ionosphere, e (in *italics*) is the elementary charge or minus the electron charge (not to confuse with the base of the exponential function e, in normal type), m_e the electron mass, k the Boltzmann constant (see appendix B for the value of some relevant physical constants) and V the potential difference between the ionosphere and the plasma sheet bases ($V = \Phi_I - \Phi_S \geq 0$; we note that negative potential drops are not treated in *Knight*'s [1973] theory). The subscripts S and I in the temperature and density state parameters denote the plasma sheet and ionosphere bases, respectively.

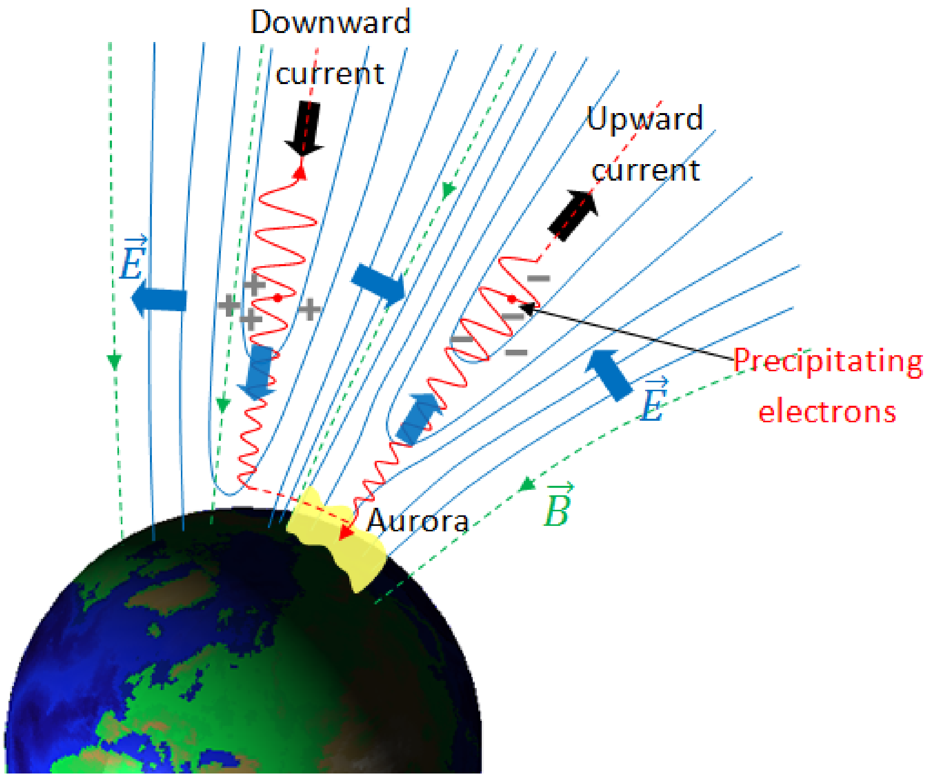

Figure 5.2. Sketch of the parallel electric fields above the auroral oval. Blue lines represent electrostatic potential contours, while green dashed lines represent magnetic field lines. Blue arrows show the electric field direction. Accelerated electrons (whose spiraling trajectories are represented with red lines) in the upward current region produce additional conductivity in the ionosphere, together with the discrete auroral display.

Since the current is assumed to be primarily carried by electrons, it is useful to think of the first term on the right hand side within the braces of (5.2) as the downward flux of electrons precipitating from the plasma sheet region, F_S, and the second term as the upward flux of electrons from the ionosphere, F_I, so that $J_\parallel = e(F_S - F_I)$. Let us define

$$F_0 \equiv N_S \sqrt{\frac{kT_S}{2\pi m_e}} \tag{5.3}$$

the downward flux of electrons from the plasma sheet for a zero potential difference, i.e., essentially the number density times the thermal velocity of the plasma sheet electron population. It should be pointed out that such electron flux, though it has not been accelerated by parallel electric fields, is still capable of producing certain ionization upon incidence onto the auroral ionosphere. This flux is deemed responsible for the diffuse aurora in our approach, and is described in the TIE-GCM by the Zhang & Paxton formulation. It can be checked that F_S increases monotonically from a value of F_0 (for no potential difference) up to a value of βF_0 for an infinite potential difference. The flux F_I, on the contrary, is considered not to produce effective ionization. Although the cases when $V < 0$ are not contemplated in Knight's theory, satellite observations [*Cattell et al.,* 2004] show that the dependence of the potential drop on the downward field-aligned current is weaker in these situations (see an application in *Wiltberger et al.* [2009]). In other words, for a given amplitude of the downward field-aligned current, the potential drop is observed to be a fraction of that observed in upward field-aligned currents of the same amplitude. Consistent with this fact, we will consider that V is close to zero for any downward parallel current, which implies $F_S = F_0$.

The plasma sheet electron temperature, T_S, is of the order of several million (or even several ten million) kelvins, while that of the ionosphere base is just a few thousand kelvins, so $T_S/T_I \sim 1000$. The case of the electron densities is opposite: while the plasma sheet number density is of the order of 10^5 to 10^6 m^{-3}, that of the ionosphere depends on the exact height being considered, but it is about 6 orders of magnitude higher. Finally, given that the magnetic field in the high-latitude ionosphere $B_I \sim 5 \times 10^4$ nT and that of the plasma sheet $B_S \sim 10$ nT, $\beta \equiv B_I/B_S$ may be as large as 5000. However, if the acceleration process takes place about 1 R_E above the ionosphere, β may be as low as 10 [*Fridman and Lemaire,* 1980]. We also note, as may be checked by introducing these figures in (5.2), that the field-aligned current is negative (i.e., downward) for a range of small positive values of the potential drop.

The TIE-GCM essentially requires the number flux F_S and the mean energy $\bar{E}$ of the precipitating electrons to compute the auroral conductivities. Thus in the following discussion we pursue an expression for these quantities as a function of the AMPERE input.

From (5.2) and (5.3), it is straightforward to see that $F_S = F_0$ is a very good approximation when $eV \leq 0.05kT_S$. On the other hand, from the above discussion about the typical values of the state parameters at the two ends of the field line, it follows that $F_I = 0$, and hence $J_\parallel = eF_S$ in an excellent approximation when $eV > 0.05kT_S$. Since $F_S \geq F_0$ and $F_S \geq J_\parallel/e$ (i.e., the flux of downgoing electrons must be greater or at least equal to the net downward flux), it turns out that $J_\parallel/e > F_0$ implies $eV > 0.05kT_S$, and therefore $F_S = J_\parallel/e$ (where $J_\parallel$ is given by the AMPERE satellite measurements); otherwise (i.e., when $J_\parallel/e \leq F_0$) we use $F_S = F_0$.

On the other hand, the mean energy of the precipitating electrons at each point of the ionosphere base is defined as

$$\bar{E} = \frac{\int_{E_k=0}^{\infty} E_k dF_S(E_k)}{\int_{E_k=0}^{\infty} dF_S(E_k)} = \frac{\int_{E_k=0}^{\infty} E_k f_s(E_k) dE_k}{\int_{E_k=0}^{\infty} f_s(E_k) dE_k} = \frac{Q}{F_S}, \tag{5.4}$$

where E_k is the kinetic energy (normally expressed in keV units in the literature) of the electrons from the source region, dF_S (1/cm^2/s) is the differential flux of electrons with kinetic energies within a differential energy interval dE_k, $f_s(E_k) \equiv dF_S/dE_k$ (1/cm^2/s/keV) is the number flux density, and Q (usually erg/cm^2/s) is the associated overall energy flux. We note that the above quantities are defined at each point of the surface defined by the top of the high-latitude ionosphere, i.e., they are given as a function of (magnetic) latitude and longitude. It should also be noted that the integral must comprise precipitating electrons from the source region only (i.e., primary electrons), excluding electrons of ionospheric origin. Since the latter have thermal energies below about 1 eV, the integral in (5.4) is accomplished in practice (e.g., by measuring satellites) by shifting the minimum kinetic energy to a few tens of electronvolts. Given the much higher temperatures in the electron source region, this alternative lower limit does not alter the integral for the mean energy of the magnetospheric electrons. However, as a result of the collision of the primary electrons with the ionosphere, secondary and backscattered electrons are produced with energies up to a few hundred electronvolts. Satellites (e.g., the Defense Meteorological Satellite Program (DMSP) series) measuring the mean energy of incoming electrons must take this component into account [*Robinson et al.,* 1987].

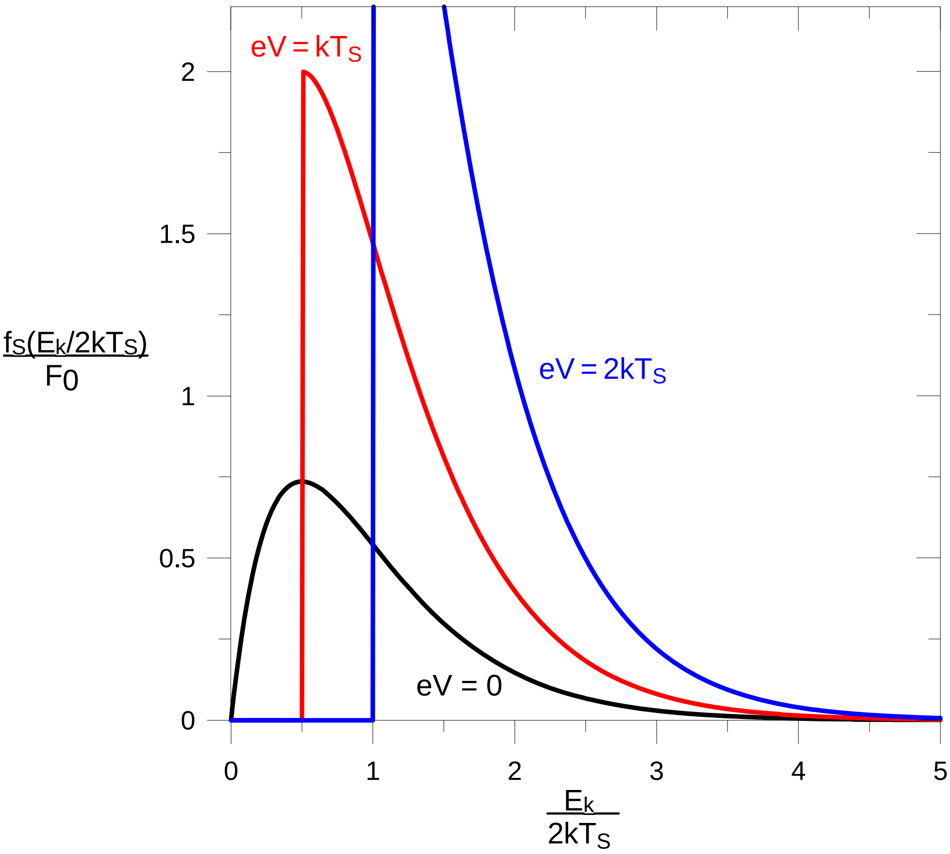

Figure 5.3. Auroral spectrum, i.e., number flux density in the ionosphere base as a function of the kinetic energy of precipitating electrons (relative to the purely Maxwellian values of both, the total flux and the mean energy, respectively) for various Maxwellian distribution functions in the source region and for β >> 1. The zero flux in the low energy region for eV > 0 reflects the lack of flux of magnetospheric electrons with energies below eV in the ionosphere.

Let us assume a purely Maxwellian distribution function in the electron source region, though it is known that the real form is that of a kappa distribution, that is, Maxwellian, but with a power law tail at high energies [*Newell et al.*, 2009]. The number flux density in the magnetosphere, in this case, is proportional to $E_k \exp(-E_k/kT_S)$. When there is no potential drop between the magnetosphere and the ionosphere bases, the expression for the flux density is transferred to the ionosphere unchanged, so $f_s(E_k)$ is also proportional to $E_k \exp(-E_k/kT_S)$, which is represented by the black line in Figure 5.3. Using this expression in equation (5.4) yields a mean energy equal to $2kT_S$. Introducing a potential drop V in the Maxwellian, however, produces a change in the auroral spectrum measured in the ionosphere. Perhaps the most immediate change is that there are no electrons with energies below eV. Even in this case, however, it is still possible to find an exact expression for $\bar{E}$ from (5.4) (see equation C.18 in appendix C):

$$\bar{E} = 2kT_S + \frac{eV}{1 + \frac{1}{\beta}\left(\mathrm{e}^{\frac{eV}{kT_S}\frac{1}{\beta-1}} - 1\right)^{-1}}, \tag{5.5}$$

which reduces to $2kT_S + eV/(1 + kT_S/eV)$ for the relatively common case when $eV/kT_S \ll \beta$, or to $kT_S + eV$ when additionally $eV/kT_S \gg 1$.

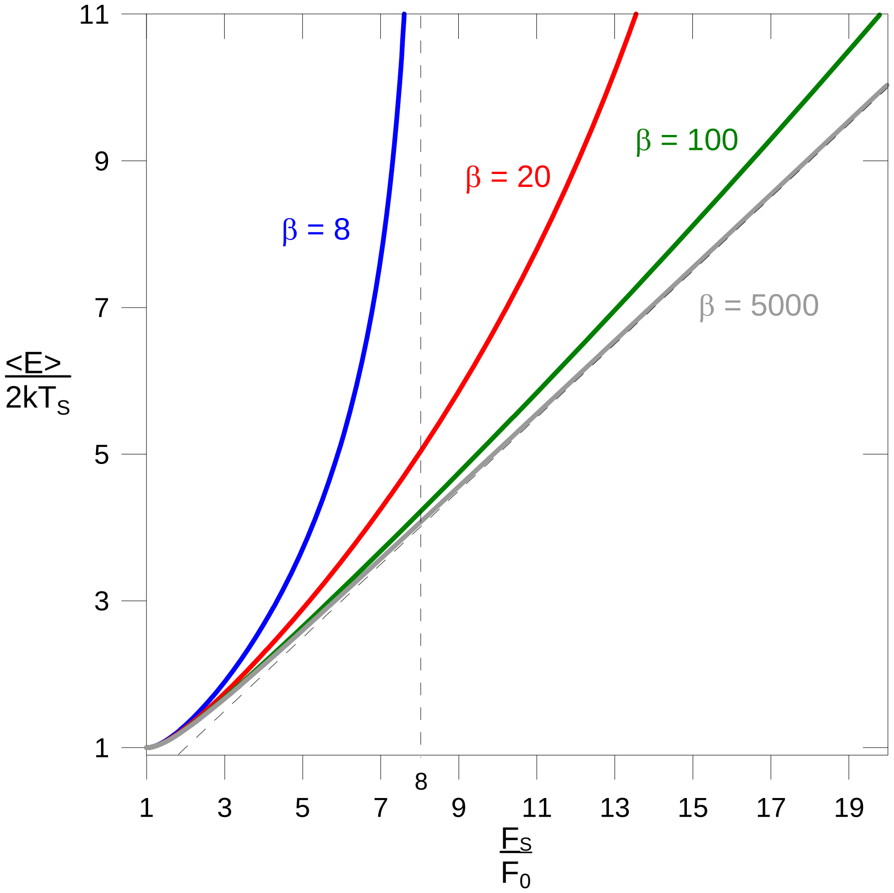

Figure 5.4. Mean energy in the ionosphere base as a function of the flux of precipitating electrons (both relative to their purely Maxwellian values) for various β values.

Expressing V as a function of F_S based on (5.2), one obtains

$$\bar{E} = 2kT_S\left[1 + \frac{\beta}{2}\left(1 - \frac{F_0}{F_S}\right)\ln\left(\frac{\beta - 1}{\beta - \frac{F_S}{F_0}}\right)\right], \tag{5.6}$$

which reduces to

$$\bar{E} = kT_S\left(\frac{F_S}{F_0} + \frac{F_0}{F_S}\right) \tag{5.7}$$

for the relatively common case when $F_S/F_0 \ll \beta$, or to $kT_S F_S/F_0$ when additionally $F_S \gg F_0$. Based on equation (5.6), Figure 5.4 illustrates the dependence of the mean energy (normalized to its Maxwellian value) on the ratio of the accelerated (F_S) to non-accelerated (F_0, or Maxwellian) flux.

Thus in summary, the mean energy of the precipitating electrons is found to be $2kT_S$ where $F_S = F_0$ (i.e., where $J_\parallel/e \leq F_0$), while the full expression (5.6) must be used where $F_S > F_0$ (i.e., where $J_\parallel/e > F_0$).

The number flux F_S, the energy flux Q, and the characteristic energy α, which is defined as half the mean energy $\bar{E}$ associated with electrons precipitating from the source region, are the three quantities used in the TIE-GCM to specify the aurora. In our approach, these input quantities are obtained following the procedure shown in Table 1. Since we use the AMPERE currents as an input, hereafter we change our notation $J_\parallel$ with $J_\parallel^{AMP}$, just to emphasize the use of this dataset. Table 1 is read as follows in the case of the number flux: F_S takes the value $Q_{ZP}/\bar{E}_{ZP}$ when $J_\parallel^{AMP} \leq eQ_{ZP}/\bar{E}_{ZP}$; and $J_\parallel^{AMP}/e$ otherwise. In this sense, the quantity $eQ_{ZP}/\bar{E}_{ZP}$ is referred to as the Zhang & Paxton threshold.

Table 1. Approach Used in This Work to Obtain the Flux F_S and the Characteristic Energy α to Be Input in the TIE-GCM[a]

	F_S	$\alpha\ (= \bar{E}/2)$
$J_\parallel^{AMP} \leq \frac{eQ_{ZP}}{\bar{E}_{ZP}}$	$\frac{Q_{ZP}}{\bar{E}_{ZP}}$	$\frac{\bar{E}_{ZP}}{2}$
$J_\parallel^{AMP} > \frac{eQ_{ZP}}{\bar{E}_{ZP}}$	$\frac{J_\parallel^{AMP}}{e}$	$\frac{\bar{E}_{ZP}}{2}\left[1 + \frac{\beta}{2}\left(1 - \frac{eQ_{ZP}}{J_\parallel^{AMP}\bar{E}_{ZP}}\right)\ln\left(\frac{\beta - 1}{\beta - \frac{J_\parallel^{AMP}\bar{E}_{ZP}}{eQ_{ZP}}}\right)\right]$

[a] The superscript "AMP" stems from AMPERE; the subscript "ZP" refers to the K_p-dependent functions specified by *Zhang and Paxton* [2008].

The mean energy Q is obtained as the product $\bar{E}F_S = 2\alpha F_S$ from (5.4). The quantity β in Table 1 is not a constant along the auroral oval, but it is calculated at each AACGM latitude as the ratio B_I/B_S, where B_S is calculated as a function of the distance to the point that the corresponding field line crosses the dipole equator, and subsequently applying the dipole magnetic field equation to compute the magnetic field strength at that point. This approximation, indeed, often constitutes a lower limit for β, as the IGRF model is used to trace the field line to the equator, whereas real field lines are elongated towards the magnetotail (especially those at the dayside auroral oval, which have an uncertain topology). As the geomagnetic activity increases, however, the inner boundary of the plasma sheet is known to approach the Earth [see *Kamide*, 1988, and references therein], and so is the case for the electron acceleration region of the midnight sector of the auroral oval. The front of the auroral electrons reservoir is sometimes extended down the magnetic field lines [*Fridman and Lemaire*, 1980], and we assume that this is the case during disturbed conditions. These effects have been introduced in our approach in such a way that β is modified over the nightside hemisphere for AACGM latitudes between 50˚ and 70˚ during disturbed conditions. In particular, β is halved when $K_p > 4$, and β is set as low as 8 when $K_p > 6$. A β value of 20 has also been tried for test purposes when $K_p > 6$. However, the quantities output by the TIE-GCM show little sensitivity to these tentative choices.

It is also known that sunlight, and in general higher conductivity regions previously present in the ionosphere, suppresses the discrete aurora [e.g., *Blomberg and Marklund*, 1988; *Newell et al.*, 1996; *Wiltberger et al.,* 2009]. Though the exact mechanism is unknown, the reason for this phenomenon would be associated with the fact that the current may flow from the magnetospheric source region into the ionosphere without need of enhanced potential drops where the background ionospheric conductance is great enough. Where the initial conductance is low, however, parallel electric fields would build up above the ionosphere, giving rise to energetic electrons that would eventually produce collision-induced conductance to close the magnetosphere-ionosphere circuit. This effect has also been simulated in our model by an effective reduction of the parallel currents on the dayside auroral oval, where the EUV conductance is relatively high. As in the work by *Wiltberger et al.* [2009], the energy of the precipitating electrons in the auroral zone has been set inversely proportional to the EUV-induced Pedersen conductance, which in turn is modeled by the empirical formula given by *Richmond* [1995a]:

$$\Sigma_P^{EUV} = \Sigma_{P\,0}^{EUV} \left(\frac{\mathrm{F}_{10.7}}{\mathrm{F}_{10.7}^{0}}\right)^{1.1} \left(\frac{B}{B_0}\right)^{-1.6} \sqrt{\cos\chi}\ , \tag{5.8}$$

where $\Sigma_{P\,0}^{EUV} = 11$ S, B is the geomagnetic-field strength evaluated at an altitude of 125 km over the point of interest, the values $\mathrm{F}^0_{10.7} = 100 \times 10^{-22}$ W/m^2/Hz and $B_0 = 5 \times 10^4$ nT are normalizing factors for $\mathrm{F}_{10.7}$ and B, respectively, and χ is the solar zenith angle, i.e., 0˚ for an overhead sun. The formula (5.8) is an approximation valid for $\chi < 80˚$. The factor that we have adopted here for the effective field-aligned current for purposes of calculating the ionospheric conductances is:

$$J_{\parallel\,eff}^{AMP} = \begin{cases} J_{\parallel}^{AMP} \dfrac{\Sigma_P^{EUV}(80^\circ)}{\Sigma_P^{EUV}(\chi)} = J_{\parallel}^{AMP} \sqrt{\dfrac{\cos 80^\circ}{\cos\chi}} & \chi < 80^\circ \\ J_{\parallel}^{AMP} & \chi \geq 80^\circ \end{cases},$$

resulting, e.g., in an effective 36 % reduction of $J_{\parallel}^{AMP}$ for a solar zenith angle of 65˚, while the parallel current remains unchanged above 80˚ (e.g., in the nighttime sector). Note that a reduction of the effective upward current introduced in Table 1 leads to a reduction of the ionospheric conductances, as experimentally observed.

We refer to the "diffuse aurora solution" where the Zhang & Paxton formulation is applied, i.e., where $J_{\parallel\,eff}^{AMP} \leq eQ_{ZP}/\bar{E}_{ZP}$. Note that, in our approach, this solution is not only adopted at zones where strictly $eV = 0$, but in general where $eV \leq 0.05kT_S$

(including zones with negative potential drops), which typically corresponds to a potential drop of the order of 100 volts. Likewise, we refer to the "discrete aurora solution" where the Knight formulation related to electrons accelerated by parallel electric fields is adopted, i.e., where $J_{\parallel eff}^{AMP} > eQ_{ZP}/\bar{E}_{ZP}$. The upward parallel current $J_{\parallel}^{AMP}$ (from which $J_{\parallel eff}^{AMP}$ is computed) is obtained by interpolating the radial AMPERE currents J_{r}^{AMP} to the TIE-GCM grid, and then multiplying by the factor $1/|\sin I|$, with the magnetic inclination I given at each point by the IGRF, i.e., $J_{\parallel}^{AMP} = J_{r}^{AMP}/|\sin I|$.

Note that the Zhang & Paxton formulation on the energy flux and mean energy of precipitating electrons as a function of K_p is a statistical mean based on a number of satellite passes for a given value of K_p. This average contains not only zones of diffuse precipitation, but also zones of discrete precipitation, especially as K_p increases and at the upward R1 current sector [*Korth et al.,* 2014]. This means that the value of $\bar{E}_{ZP}$, which is adopted as $2kT_S$ in our approach, indeed overestimates the source region temperature T_S, and in consequence the value of α. This is not so much the case for the flux F_S, where $J_{\parallel}^{AMP}/e$ is thought to be an excellent approximation of the high-energy plasma sheet electron flux, though for low energy electrons the flux F_0 could indeed be slightly overestimated. Since $Q = \bar{E}F_S$, this results in an overestimated energy flux. This effect can also be understood through the following reasoning: the approach applied in this work is equivalent in practice to substituting the mean energy of zones with significant upward current by enhanced mean energies proceeding via parallel acceleration, thus enhancing $\bar{E}$ and therefore Q with respect to the results from Zhang & Paxton, which are empirical and hence should be approximately fulfilled when globally averaged. In order to avoid this overestimation, the following step of our approach consists in adjusting the initial guess for F_0 and $\bar{E}_{ZP}$ given in the upper row of Table 1 so that the two following conditions are simultaneously met: 1) the hemispheric average of the mean energy for each K_p (considering zones with significant values of the energy flux and mean energy) equals the empirical K_p-dependent hemispheric average of $\bar{E}$ given by *Zhang and Paxton* [2008]; and 2) the HP, which is the hemispherically integrated energy flux, equals their empirical K_p-dependent HP (see Figure 8 of *Zhang and Paxton* [2008]). This is an iterative process that converges to mean energies and fluxes more according to observations. However, our experience shows that the final values of F_0 and $\bar{E}_{ZP}$, which are typically obtained after two or three iterations, are usually within 10 % of our initial guess, indicating that the original values were sufficiently good.

The overall result of our approach is an auroral specification that gives more weight to prominent upward currents (as given by the AMPERE dataset) with respect to the empirical Zhang & Paxton's mean auroral specification for a given K_p, whereas the empirical values of both, the hemispheric average of the mean energy and the HP, are guaranteed. The consequent redistribution of auroral conductivities should have an impact on the high-latitude electrodynamics.

6. MODEL APPLICATION. RESULTS AND DISCUSSION.

This chapter includes results and discussion relative to several case studies the AMPERE-driven TIE-GCM has been applied to. In particular, we present some of the most relevant electrodynamic quantities output by the model. The ground magnetic signatures of the resulting ionospheric currents are compared with contemporaneous observations at different sites and for different magnetic disturbance levels. The ionospheric conductances yielded by our model have also been put side by side with two existing models that account for precipitation-induced conductance enhancements. All of these comparisons are then used to validate our approach. We also describe the parameters that we have adjusted to get a better agreement between model output and observations. Comparison with the standard TIE-GCM has been carried out to evaluate the impact of our modification.

6.1. MODEL VALIDATION TOOLS

6.1.1. EVALUATING THE GENERAL PERFORMANCE

In order to validate the improvements made on the model, we need to evaluate its performance (P), i.e., how well the model output fits the observations. To that end, we define the following quantity:

$$P = 100\left(1 - \frac{RMSD_{om}}{\sigma_o}\right), \qquad (6.1)$$

where σ_o is the standard deviation of the set of observations for a given case study, and $RMSD_{om}$ the root mean square deviation of the residuals (or differences between model and observations):

$$RMSD_{om} = \sqrt{\frac{\sum_{i=1}^{N}(o_i - m_i)^2}{N}},$$

where o_i and m_i are the i-th elements of the observation and model output series, respectively, out of a total of N. This parameter P has been used in *Torta et al.* [2014] to evaluate the agreement between modeled and observed GICs. Given that the quotient in (6.1) is a positively defined quantity, P cannot be greater than 100, which is reached when the residuals are zero, i.e., when the model exactly fits the observations. Otherwise, P < 100. P would be 0, for example, for a flat model output equal to the mean of the observations. A negative value of P may denote anti-correlation. So in summary, the better performance of the model, the higher the value of P, and one can think of P (with some reservations) as the fraction (over a maximum of 100) of the standard deviation of the observations which can be explained by the model. If the mean of the model output, $\overline{m}$, is further set to equal the mean of the observations, $\bar{o}$, then P can be expressed either in terms of the standard deviation of the residuals, σ_r, or as a function of the covariance between model and observations, σ_{om}:

$$P = 100\left(1 - \frac{\sigma_r}{\sigma_o}\right) = 100\left(1 - \sqrt{1 - \frac{2\sigma_{om} - \sigma_m^2}{\sigma_o^2}}\right). \qquad (6.2)$$

It is relevant to recall in this context that the TIE-GCM is a model of the Earth's upper atmosphere, and as such, its output is not intended to account for the whole magnetic field observed at any altitude (including the surface). Instead, the modeled magnetic field is essentially meant to give the contribution arising from the (toroidal) currents flowing in the ionosphere, no account being made of important magnetospheric current systems such as those especially developed in the magnetopause, magnetotail and ring current regions during disturbed conditions (which are precisely the situations most widely discussed in this chapter), not to mention the slowly-varying core and crustal fields. Furthermore, as mentioned in chapter 4, the code module computing the magnetic signature of the modeled ionospheric currents incorporates a simple 1-D model of the Earth's inner conductivity consisting of a sphere of perfectly conducting material below a certain depth and a perfect insulator above, thus neglecting the real 3-D variation, e.g., the existence of horizontal conductivity variations associated with geological structures or land/ocean discontinuities. We also recall that the magnetic code also accounts for the contribution of the field-aligned currents flowing between the ionosphere and its field-line apex within the magnetosphere. These currents, however, are not assumed to close in the magnetospheric apex, but they flow radially to or from infinity, where the circuit is effectively closed (see section 4.2.3).

The above facts have several implications. Firstly, the model performance P is not expected to be 100 % in any case. It is difficult to assess the relative importance of the contribution of the excluded current systems from the overall ground magnetic field, since they highly depend on the specific conditions at each time. Also an obvious dependence on latitude exists, e.g., the relative weight of the magnetopause contribution is increased at low latitudes with respect to higher ones. Some authors allocate the magnetospheric contribution a fraction as great as 20 % to 30 % of the ionospheric dynamo amplitude [*Olsen,* 1996, 1997], which would imply nearly 20 % of the total (in round numbers). An additional error of at least 10 % of the total amplitude could arise from a simplified estimation of the ground-induced currents. However, this does not necessarily imply that the remaining 70 % is the expected optimum value of the model performance P; we rather believe this maximum value to be closer to 80 % at high latitudes during disturbed conditions, going down to 75 - 70 % at middle and lower latitudes.

Another implication of the fact that the TIE-GCM gives only the ionospheric contribution of the magnetic field is that in evaluating the model behavior we need to put both series on a par to make them comparable. The reason is that the parameter P, as defined in (6.1), is sensitive to a constant baseline added to each of the series. At least two options exist to overcome this point: first, we can move both series by subtracting their respective averages during the overall analyzed interval (i.e., so that $\bar{m} = \bar{o} = 0$); second, if a relatively quiet period exists prior to the advent of the analyzed interval, we can shift both series by subtracting their respective averages during that quiet interval. Whereas the second option would be the most appropriate if we were to evaluate the performance of the magnetic field model itself, this option would detract the results of our evaluation when the magnetospheric currents are important, since they are not accounted for. For this reason, we have adopted the first option, which enables the use of equation (6.2).

6.1.2. EVALUATING THE MODEL CONDUCTANCES

Another means to evaluate our model, and in particular our approach of conductivities consistent with field-aligned currents, is provided by comparing our height-integrated conductivities (or simply conductances) with other previous works where auroral electron precipitation was accounted for. Specifically, we will compare our output with the independent results given by *Robinson et al.* [1987] and by *Marklund et al.* [1988].

In their paper, *Robinson et al.* [1987] give expressions relating Pedersen and Hall conductances (Σ_P and Σ_H, respectively) to the mean energy and energy flux of precipitating electrons. They are reproduced here:

$$\Sigma_P = \frac{40\bar{E}}{4^2 + \bar{E}^2} Q^{1/2}; \qquad \frac{\Sigma_H}{\Sigma_P} = 0.45\bar{E}^{0.85}, \tag{6.3}$$

where the conductances are expressed in siemens (S), the mean energy in keV, and the energy flux in erg/cm^2/s. These expressions are based on previous results by *Vickrey et al.* [1981], which used electron spectral distributions to compute auroral conductances and were in turn validated using simultaneous electron spectrometer data from the Atmospheric Explorer C (AE-C) satellite and ionization measurements made by the Chatanika incoherent scatter radar [*Vondrak and Robinson*, 1985].

Figure 6.1 shows the values of the Pedersen conductance and the Hall-to-Pedersen conductance ratio for several values of $\bar{E}$ and different activity levels as given by the K$_p$ index. Not unexpectedly, the results from *Zhang and Paxton* [2008] show that, in general, zones with enhanced energy flux correspond to enhanced electron mean energies, though in a different manner for each activity level, in such a way that the range of variation of Q for a given $\bar{E}$ increases with K_p. We have found average empirical relations of Q as a function of $\bar{E}$ and K_p based on the Zhang & Paxton model, which in turn have been introduced in expression (6.3) for Σ_P. As a result, we obtain $\Sigma_P\left(\bar{E}, Q(\bar{E}, \mathrm{K_p})\right)$, or equivalently $\Sigma_P(\bar{E}, \mathrm{K_p})$, which corresponds to the different plots in Figure 6.1. As an example, we see that for a K_p = 6, zones of the auroral oval with a mean energy $\bar{E} = 5$ keV have an average Pedersen conductance around 11 S.

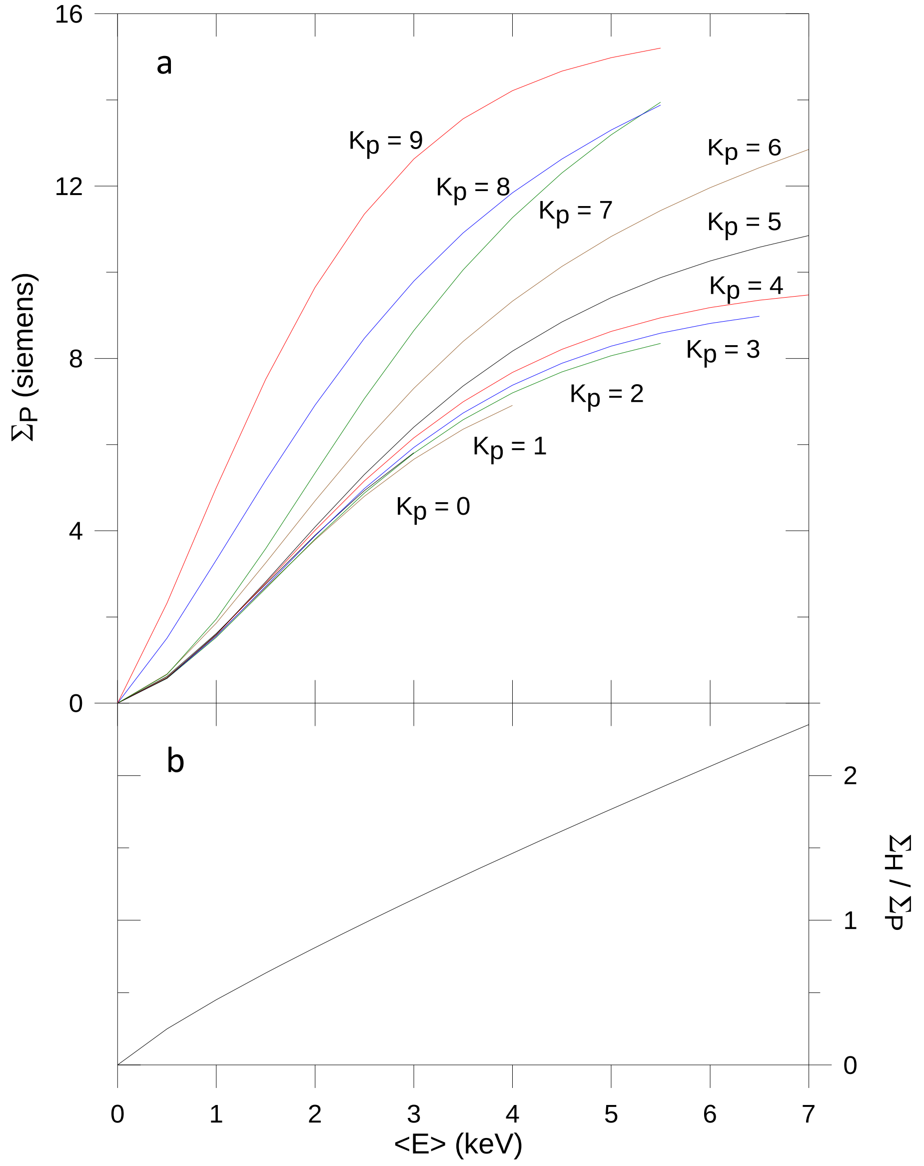

Figure 6.1. Relationships between the mean energy of auroral precipitating electrons and (*a*) Pedersen conductance (upper panel), and (*b*) Hall-to-Pedersen conductance ratio (lower panel) for various activity levels as measured by K_p. The plots have been obtained by combining the *Zhang and Paxton* [2008] model with the formulas of *Robinson et al.* [1987]. The quantity in the lower plot is a measure of the ionospheric capability to produce ground magnetic perturbations.

It is worth to mention here, following *Robinson et al.* [1987] precepts, that the integral in (5.4) is more conveniently terminated at 0.5 keV in the lower limit. The reason, as mentioned in section 5.3, is that the low energy portion of the spectrum below this limit is indeed full of backscattered and secondary electrons of ionospheric origin (not reflected in Figure 5.3), and so the usual means to compute the flux of precipitating electrons (e.g., satellites) cannot differentiate between the two origins, whereas (5.4) is meant to include only those primary electrons precipitating from the magnetosphere. Moreover, because this false component is highly variable in space and time, it is hardly subject to modeling. *Robinson et al.* [1987] illustrate an example where the mean energy increases up to a factor around 25 when the 0.5 keV limit is applied with respect to the usual 10-eV limit. Fortunately in our case, however, electrons below about 0.5 keV do not contribute much to the conductance because they cause ionization at higher altitudes, where perpendicular currents in the ionosphere are negligible [*Rich et al.,* 1987].

Zhang and Paxton's [2008] method uses the whole spectrum of energies for the mean energy computation in (5.4). However, as their method is based on the theoretical FUV radiance produced by a predefined distribution of electrons (e.g., Gaussian or Maxwellian), the low energies do not include the unwanted secondary electrons (Y. Zhang, personal communication, 2014). Thus, strictly speaking, the Zhang & Paxton original values should be corrected to exclude only the low portion of the primary spectrum below E_k^{min} = 0.5 keV if they are to be compared with those obtained by use of relations (6.3). These corrections are observed to depend on the ratio $E_k^{min}/\bar{E}_{ZP}$ (see appendix D). Obviously, when the original mean energy is below about 0.5 keV, the relative weight of the low energies in the F_0, Q_{ZP} and $\bar{E}_{ZP}$ quantities is high, and the corrections must be correspondingly significant. However, the corrected values rapidly converge to the original Zhang & Paxton values for higher energies. For a relatively low value of the mean energy of 2 keV, for example, the corrections to F_0, Q_{ZP} and $\bar{E}_{ZP}$ are just 9 %, 1.4 % and 8 %, respectively. Given that the low energies do not contribute substantially to the generation of currents, and because relations (6.3) (which we use for comparison purposes) are approximated, we have chosen not to implement these second order corrections.

We recall that $\bar{E}$ and Q at each latitude and longitude are available in our approach for use in (6.3) from the relationships summarized in Table 1, where $\bar{E} = 2\alpha$ and $Q = \bar{E}F_S$. This gives rise to conductance distributions that can be compared with those obtained by the AMPERE-driven TIE-GCM. Note, in consequence, that we start from $\bar{E}$ and Q values that have been previously calculated from the AMPERE currents. In this sense, this method does not validate the more controversial translation from field-aligned currents to the distribution function parameters of the precipitating population (i.e., mean energy and energy flux), but it rather evaluates the ability of the standard TIE-GCM to calculate the conductances from these parameters. The application of the results by *Marklund et al.* [1988] to the AMPERE field-aligned current data is aimed at complementing the validation. In that and other related works [e.g., *Blomberg and Marklund,* 1988, 1991], the authors try to quantify the well-known relationship between the density of upward field-aligned current and the height-integrated ionospheric conductivity, proposing the following expressions:

$$\Sigma_{J\parallel}^{P,H} = \begin{cases} k^{P,H}(MLT)\left|J_\parallel\right| & J_\parallel \text{ upward} \\ 0 & J_\parallel \text{ downward} \end{cases},$$

where $J_\parallel$ is the magnetic field-aligned current at the top of the ionosphere, and $k^{P,H}$ are proportionality factors that are in turn functions of MLT, accounting for the differences in the hardness of the particle spectrum. The superscripts P and H on $\Sigma_{J\parallel}$ and k refer to the Pedersen and Hall conductances, respectively. These proportionality factors reach a minimum during daytime, where the particles are softer. The dependence of k on MLT seems to vary slightly in each work, depending upon the activity level of the event being analyzed, among other parameters [*Blomberg and Marklund*, 1991], and here we will use the values employed by *Marklund et al.* [1988] for reference:

$$k^P = \begin{cases} 2\ \times 10^6\ \mathrm{Sm^2/A} & 7\ \mathrm{h} \le MLT \le 17\ \mathrm{h} \\ 13\ \times 10^6\ \mathrm{Sm^2/A} & MLT \le 5\ \mathrm{h};\ MLT \ge 19\ \mathrm{h} \end{cases}; \quad k^H = 1.7k^P \qquad (6.4)$$

with a smooth transition between the two extreme values of k^P in the morning and evening sectors (i.e., between 5 h and 7 h MLT, and between 17 h and 19 h MLT). Note that despite the remarkable differences in solar illumination, $k^{P,H}$ do not depend on the season within the year, the summer solstice being treated as the winter one. Assuming $J_\parallel = J_r^{AMP}/|\sin I|$, we get a conductance distribution that we compare with the one output by the AMPERE-driven TIE-GCM. Because of the approximations stated above assumed by *Marklund et al.* [1988], i.e., linearity between $J_\parallel$ and conductance, and simple MLT dependence of k, we do not expect a close matching of the two conductance distributions, but rather an order-of-magnitude impression on the compatibility of these two methods. At this point, the reader might wonder why we have not introduced this linear dependence between the AMPERE upward Birkeland current and the ionospheric conductance in the TIE-GCM directly. The reason is that the TIE-GCM is a 3-D model of the upper atmosphere, whereas the conductance is a height-integrated conductivity, implying that these two quantities must be consistent with each other. On the other hand, the standard TIE-GCM, as mentioned above, is ready to receive the auroral precipitation parameters (mean energy and fluxes) to compute the conductivities at each point of a 3-D grid by means of a particle deposition code, from where the conductances can afterwards be deduced.

It may be pertinent to make an aside here to evaluate the consistency between our approach and the one used by *Marklund et al.* [1988]. Referring back to equation (5.6), for which (5.7) is a good approximation, we see that $\bar{E} \cong kT_S F_S/F_0 = kT_S J_\parallel/(eF_0)$ where $F_S/F_0 \ge 2$. Likewise, $F_S = J_\parallel/e$ when $F_S/F_0 > 1$, and in particular when $F_S/F_0 \ge 2$, so $Q = F_S\bar{E} = J_\parallel\bar{E}/e \cong kT_S J_\parallel^2/(e^2F_0)$, i.e., $Q^{1/2}$ is approximately proportional to $J_\parallel$. On the other hand, note that equation (6.3) for Σ_H (after *Robinson et al.* [1987]) is weakly dependent on $\bar{E}$ for mean energies above about 7 keV, which are typical for precipitating electrons. Therefore, we obtain $\Sigma_H \propto Q^{1/2} \propto J_\parallel^{AMP}$, in agreement with the work of *Marklund et al.* [1988]. Indeed, the fact that the conductivity is roughly proportional to the square root of the energy flux is also found by *Harel et al.* [1981]. If we consider that the mean diffuse energy given by Zhang & Paxton is about 6 keV in the moderately disturbed auroral oval (meaning $kT_S \cong$ 3 keV), then the $F_S/F_0 \ge 2$ limit implies $\bar{E} \cong kT_S(F_S/F_0 + F_0/F_S) \ge 3\ \mathrm{keV}(2 + 0.5) \cong$

$3\,\mathrm{keV} \times 2 = 6\,\mathrm{keV}$, and so the condition $F_S/F_0 \geq 2$ required above for $Q^{1/2} \propto J_\parallel^{AMP}$ is nearly equivalent to $\bar{E} \geq 7\,\mathrm{keV}$ required for $\Sigma_H \propto Q^{1/2}$. In conclusion, the linear approximation contributed by *Marklund et al.* [1988] for Σ_H as a function of $J_\parallel^{AMP}$ is consistent with that obtained by combining our approach with that of *Robinson et al.* [1987] for $F_S/F_0 \geq 2$. On the contrary, we will show that the same linear approximation for Σ_P is not so suitable.

The values of $k^{P,H}$ given in (6.4) are used by *Marklund et al.* [1988] in a case study for which the $\mathrm{K_p}$ index is below about 4. In these moderately disturbed circumstances, Zhang & Paxton's $\bar{E}_{ZP}$ and Q_{ZP} are about 6 keV and 4 erg/cm^2/s, respectively, in the middle of the nighttime auroral oval. Thus we can calculate $\bar{E}$ and Q as a function of $J_\parallel^{AMP}$ using our approach (Table 1). This yields Σ_P and Σ_H by use of *Robinson et al.* [1987] relations (6.3). The corresponding plots are presented in Figure 6.2, where we compare them with the *Marklund et al.* [1988] conductances computed by use of (6.4). We verify that both methods give consistent Hall conductances, whereas the *Robinson et al.* [1987] method, except for the lowest values, does not even predict a linear relationship with the parallel current in the case of the Pedersen conductance.

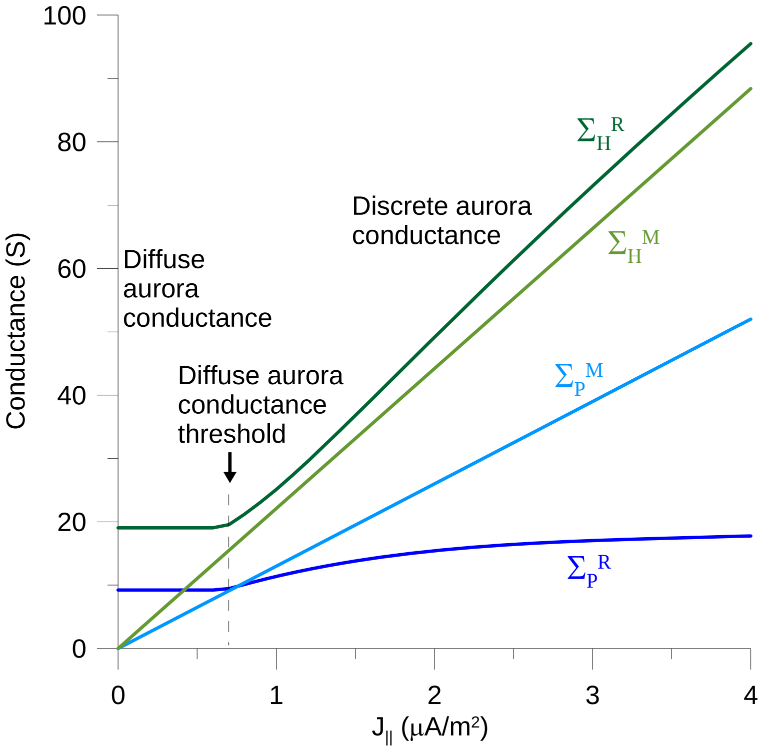

Figure 6.2. Conductances associated with field-aligned currents in the nighttime auroral zone ionosphere for moderately disturbed conditions ($\mathrm{K_p}$ = 4). The superscript R refers to the formulation by *Robinson et al.* [1987] (where mean energies and energy fluxes have been calculated from parallel currents using our approach), while M refers to *Marklund et al.* [1988] approximation. Blue colors correspond to Pedersen conductances, while green colors correspond to Hall conductances.

6.2. RESULTS

6.2.1. PREVIOUS REMARKS

In this section we give diverse information relative to the results that will be presented in this work. In particular, we give details on several options available for the model, analyzed periods, and geomagnetic observatories used to validate our data.

Different geomagnetic grid resolutions are available in the model; the high resolution grid used in this study has a constant longitude spacing of 4.5° and a variable latitude spacing with a minimum of 0.7° at auroral latitudes so as to resolve fine structures associated with localized field-aligned currents. This resolution was already used in *Marsal et al.* [2012]. In addition to this, in this work we have found it convenient to use an enhanced resolution for the geographic grid as well. While the geographic grid resolution used in the above article was 5° longitude × 5° latitude, the one used here is a double resolution, i.e., 2.5° × 2.5°, thus providing more matching with the half-wavelength latitude resolution of 3° inherent to the AMPERE data. This measure is aimed at capturing finer structures related to electron precipitation and associated conductivity enhancements in the auroral ionosphere.

A shorter model time step is recommended with the use of the higher spatial resolution, thus being reduced from 2 minutes (in the article) to 1 minute. However, the TIE-GCM continues to be set to update the AMPERE currents every 10 minutes of model time, assuming that they do not change significantly within this time interval. The above space-time specifications are much more time consuming, implying about 35 minutes of execution time per each simulated day in our 4-processor machine, where parallel computing is used. This time lapse does not include the separate module to compute the ground magnetic signatures.

As in *Marsal et al.* [2012], the soft X-ray solar flux has been increased by a factor of 4.4 following *Fang et al.* [2008]. This paper and references therein point to the difficulty of measuring X-ray fluxes accurately, and justify the particular factor 4.4 by comparing E-region electron densities in the TIE-GCM with those provided by the International Reference Ionosphere (IRI) under certain conditions. However, the improvement to the modeled magnetic perturbations given by the X-ray modification is modest at high latitudes.

Finally, we have upgraded the base model version from v1.94 to v1.95. The latter, released on June 2013, has some bug fixes (besides some other improvements) with respect to the previous one, and is available in the TIE-GCM website (http://www.hao.ucar.edu/modeling/tgcm/download.php). An initial or spin-up run of the standard TIE-GCM is applied 20 days prior to each period analyzed in order to stabilize the upper atmosphere parameters according to the external driving conditions (i.e., solar forcing, activity level, etc.). The conditions thus obtained are then used to feed the AMPERE-driven model for the period of interest. We have checked that use of AMPERE data during the spin-up run hardly has an influence on the final results.

For the sake of clarity, we will refer to our "full approach" when AMPERE data have been used to drive the modified TIE-GCM, including model conductivities consistent with field-aligned currents as thoroughly explained in section 5.3. Thus, we will compare the results of our full approach with those of the standard TIE-GCM and with our previous approach, i.e., forcing the TIE-GCM with AMPERE data but using *no* feedback between auroral conductivities and field-aligned currents [*Marsal et al.,* 2012]. Indeed, unless otherwise specified, the "full approach" version of the modified TIE-GCM is hereafter implied.

For the comparisons to be meaningful, we have recalculated the results presented in *Marsal et al.* [2012] using the same conditions (e.g., model version, resolution, …) as we are using in the new approach, as specified in the previous paragraphs. This, along with other reasons exposed below, could cause some of these recalculated results to differ from those obtained in the cited article. For example, different types of solutions were assayed in *Marsal et al.* [2012] to get a better fit with observations. In particular, we assayed with the "NS, NH and SH solutions" (see section 5.2) and with the depth of the perfect conducting layer (see section 4.2.3), for which the better results were chosen in each case, regardless of the consistency among them. However, since the "NS solution" gave results generally comparable to the "NH/SH solution", here we have chosen to simplify the output by disregarding it, which otherwise would favor confusion due to the large number of solution combinations, all the more so as it contributes no substantial concepts. Thus we will use the NH solution in northern hemisphere observatories, and the SH solution otherwise. Likewise, we have chosen a fixed value of 250 km for the depth of the conducting layer at the two high-latitude observatories used for validation purposes, and a depth of 600 km at the other two midlatitude observatories. The selection of 250 km for the depth of the conducting layer at high latitudes agrees with other studies dealing with the auroral regions during disturbed conditions [e.g., *Richmond and Baumjohann*, 1984], where the effective depth of this layer is shallower as compared to lower latitudes due to dominance of shorter periods and smaller spatial scales [*Rokityansky*, 1982]. On the contrary, a value of 600 km is more adequate for slow external changes like the Sq variation, which dominates in the lower latitudes.

Table 2. Periods Analyzed in This Work and Their Respective Disturbance Levels in Terms of the A_p Index of the Most Disturbed Day in the Period (the Least in the Case of the Quiet Period)[a]

	May 28-**29**[b], 2010	August 03-**04**, 2010	October **24-25**[c], 2011	July 14-**15**, 2012	January 21-**22**, 2013	March **17**-18, 2013
A_p	28	49	60	78	1	72

[a] Values are given in the usual 2-nT units.

[b] The boldface figures in the upper row indicate the date for which A_p is given in each period.

[c] The A_p value for this particular interval is given as the mean of the eight a_p values for a 24-hour period starting on October 24, 2011, at 15:00 UT.

Given that the AMPERE field-aligned current input makes the greatest difference with respect to the standard TIE-GCM during disturbed conditions, and because the most affected (magnetic) latitudes are essentially those between 63° and 70°, we expect our model to be more adequate for gradually more disturbed conditions and increasing latitudes. For this reason, we have run the modified TIE-GCM for five selected periods between 2010 and 2013 in which AMPERE data are available, ranging from moderate to highly disturbed conditions. However, just to evaluate how the model performs during quiet conditions, we have also included a completely quiet interval. A diagnosis of the phenomena occurred during these episodes, both in the Sun and in the Earth's space environment, can be found in different websites (e.g., www.spaceweather.com, www.spaceweatherlive.com). As for the geomagnetic observatories chosen to validate our model, two of them are close to or within the auroral zone, while the other two are midlatitude observatories. Tables 2 and 3 are intended to summarize the disturbance level for the different selected periods and the observatory locations (see Figure E.1 of appendix E for a world map of these observatories), respectively.

Table 3. Geodetic and Quasi-Dipole (QD) Coordinates (for the Epoch 2013.0) of the Different Geomagnetic Observatories Used in This Study[a]

	Geodetic Longitude	Geodetic Latitude	QD Longitude	QD Latitude
Tromsø (TRO)	18.9	69.7	101.9	66.7
College (CMO)	212.1	64.9	266.8	65.0
Ebre (EBR)	0.5	40.8	76.6	34.6
Livingston Is. (LIV)	299.6	-62.7	11.2	-48.6

[a]Units are degrees (positive eastward and northward).

6.2.2. MODELED ELECTRODYNAMIC VARIABLES

The left panel of Figure 6.3 shows the radial component of the field-aligned currents at the top of the ionosphere consistent with the standard version of the TIE-GCM for October 24, 2011, at 23:30 UT. This calculation is made by the model on the basis of the convergence (i.e., minus the divergence) of the horizontal ionospheric current. The figure is aimed at giving an impression on how different these currents are from those obtained by the AMPERE-driven version, which are used to force the model in our approach and are depicted in the right panel. Note that, unlike AMPERE currents, the 'standard' radial currents are concentrated in a narrow ring around 72° QD latitude. Such a difference must have a consequence on the electrodynamics of the system.

Figure 6.4 presents azimuthal equidistant projection maps centered on the QD North pole showing the electrostatic potential at heights of the ionospheric E layer corresponding to selected instants of the six periods analyzed in this study (see Table 2). The selection has been made on the basis of showing either the peak of activity of each interval or outstanding features that we have considered worth illustrating. Panels (*a*) to (*e*) have been obtained with the northern-hemispheric (NH) solution of equation (4.2) using our full approach (i.e., AMPERE data with conductivities consistent with field-aligned currents); panel (*f*), however, has been obtained with the SH solution of (4.2), just for illustrative purposes. Panels (*a*), (*b*), (*d*) and (*f*) show typical bipolar patterns of the potential, with a maximum at the dawn side of the polar cap and a minimum at its dusk side, being approximately symmetric about the 09:30 - 10:30 MLT meridian (depending on each case). The CPCP, which is the maximum potential drop in the polar cap, is beyond 110 kV in panel (*a*). Panel (*e*), valid for quiet conditions, also presents a bipolar pattern, though with a potential drop of just a few ten kilovolts.

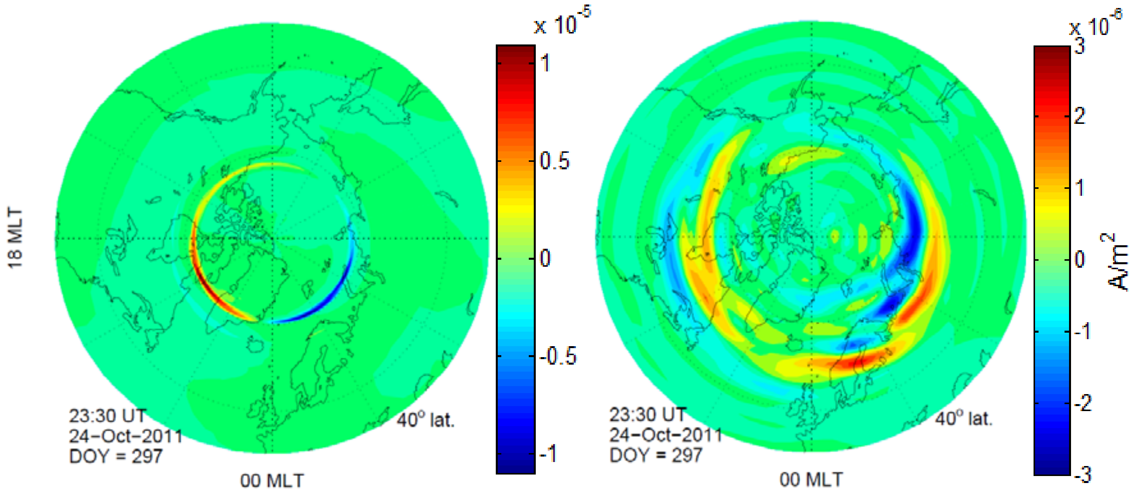

Figure 6.3. Northern hemisphere azimuthal equidistant projection maps (above 40° magnetic latitude) showing the radial field-aligned currents, J_{mr} ([A/m^2], positive upward), for the magnetically disturbed day October 24, 2011, at 23:30 UT. The left panel shows the radial currents consistent with the standard version of the model, while the right one shows the currents consistent with the AMPERE-driven model. QD coordinates are used. Note the change of scale in both panels.

Superimposed in Figure 6.4 are the height-integrated horizontal current vectors in the ionosphere, with components $K_{q\phi}$ and $K_{q\lambda}$. Once again, although for middle and high latitudes these values would be similar to K_ϕ and K_λ obtained by application of equations (2.17) and (2.18) to the above electrostatic potential, the correct definitions given by *Richmond* [1995b] must be strictly applied (note that we have not taken part in this latter calculation, which is implemented in the standard version of the TIE-GCM). Well-formed auroral electrojets can be observed at the dawn and dusk sectors of the auroral oval, as well as at its midnight edge, in most of the panels (except for the quietest day in panel (*e*)).

It is worth to emphasize the high intensity not only of the currents flowing in the dawn and dusk sectors of the auroral oval, which constitute the auroral electrojets, but also in the midnight sector, with values of the height-integrated horizontal current circa 1 A/m. It is precisely at these local times where a strong convergence/divergence of horizontal currents is observed. Such convergence (divergence) gives rise to upward (downward) field-aligned currents, as those clearly shown in the right panel of Figure 6.3, corresponding to panel (*c*) of Figure 6.4. Continuing with the same example, the modeled convection electric field (which is locally perpendicular to the contours and directed towards lower values of the potential in panel (*c*) of Figure 6.4) turns from northward to southward (going through westward) in a narrow latitudinal band that crosses the auroral belt from South to North around the premidnight sector. These facts are reasonably consistent with the Harang discontinuity [*Kamide*, 1978].

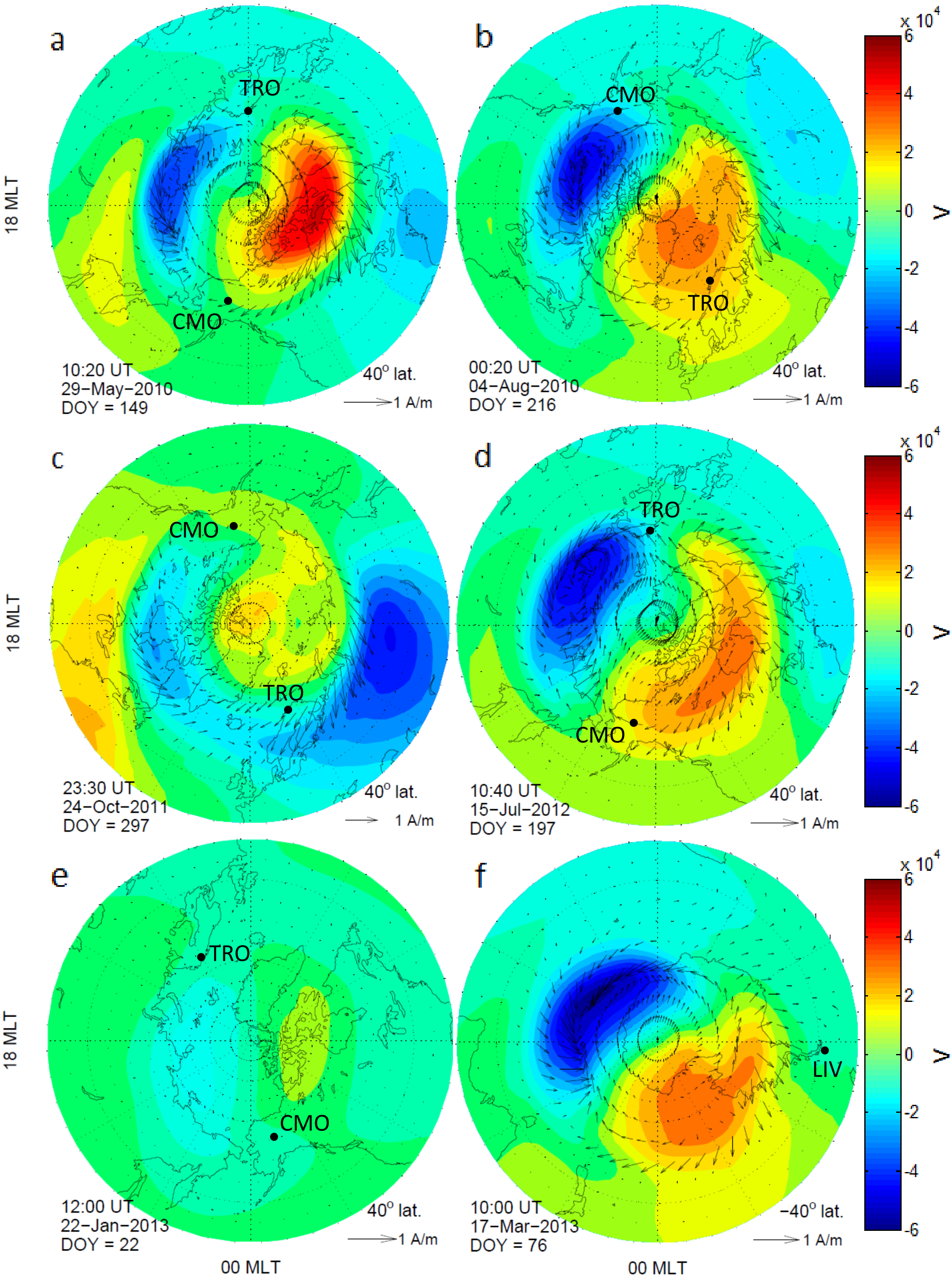

Figure 6.4. Maps showing the electrostatic potential [V] around 100 km height for selected instants of the six periods analyzed in this study. Superimposed are the height-integrated horizontal ionospheric current vectors ([A/m], see scale at the bottom right corner). QD coordinates are used. Panels (*a*) to (*f*) correspond to May 29, 2010 at 10:20 UT; August 4, 2010 at 00:20 UT; October 24, 2011 at 23:30 UT; July 15, 2012 at 10:40 UT; January 22, 2013 at 12:00 UT; and March 17, 2013 at 10:00 UT, respectively. The locations of TRO, CMO and LIV are indicated.

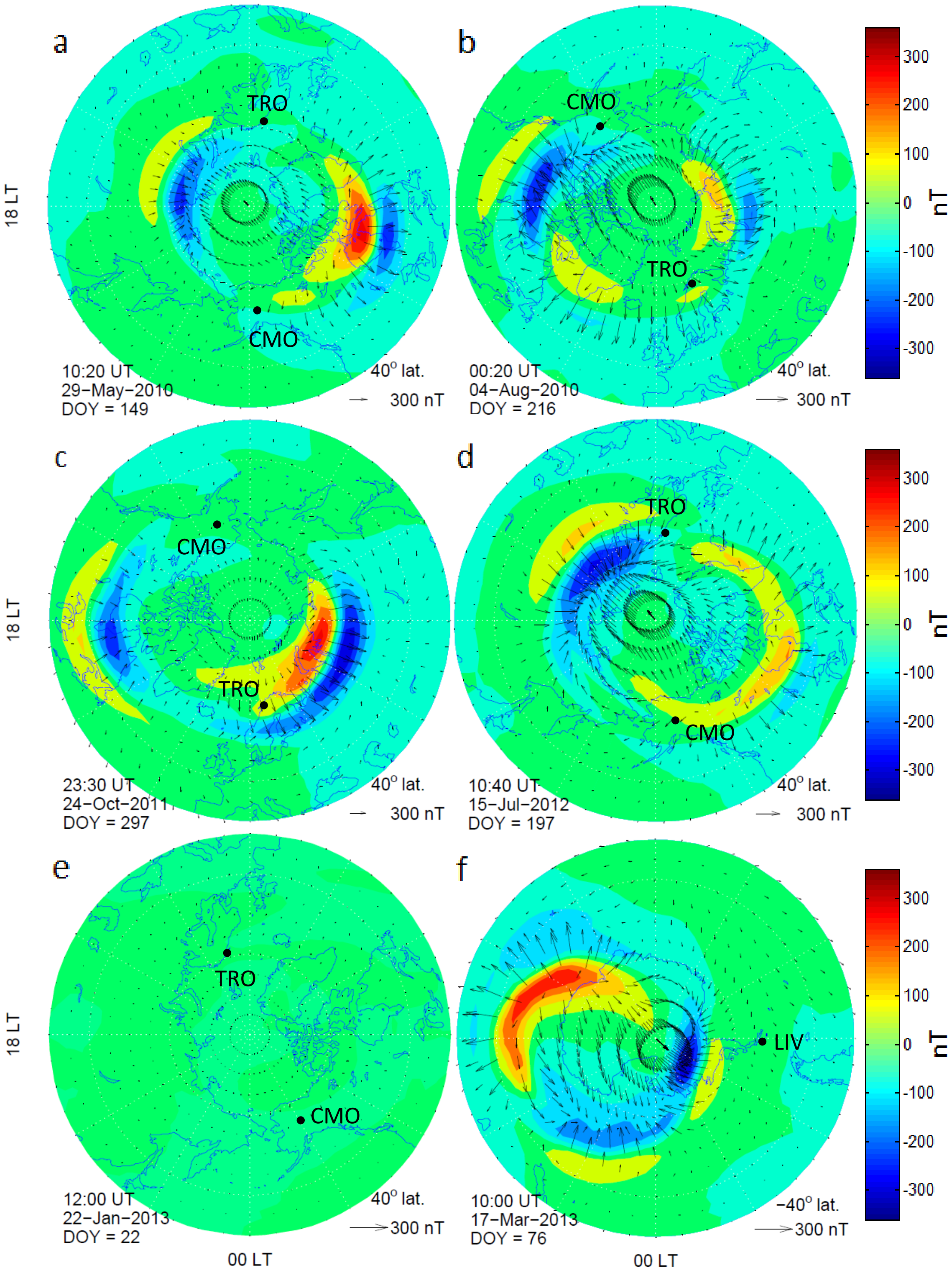

Figure 6.5. Maps showing the ground magnetic signature of currents essentially flowing in the ionosphere (see Figure 6.4) for the six periods analyzed in this work at selected instants. Arrows correspond to the horizontal projection of the vector perturbations (see scale at the bottom right corner), while contour lines correspond to the vertical component (positive downward). Geodetic coordinates are used. Panels (*a*) to (*f*) correspond to May 29, 2010 at 10:30 UT; August 4, 2010 at 00:20 UT; October 24, 2011 at 23:30 UT; July 15, 2012 at 10:40 UT; January 22, 2013 at 12:00 UT; and March 17, 2013 at 10:00 UT, respectively.

Figure 6.5 shows the ground magnetic signature yielded by the model for the selected instants and conditions shown in Figure 6.4, again using our full approach. The perfect conductor depth of the module that calculates the magnetic perturbation field has been set to 250 km in panels (*a*) to (*e*), which is appropriate for high latitudes; however, panel (*f*) has been obtained using a 600 km depth (and the SH solution for the potential, in correspondence with panel (*f*) of Figure 6.4), which is more suitable for the latitude of the Livingston Island (LIV) geomagnetic observatory. Arrows represent the horizontal projection, while the contour lines represent the vertical component (positive downward) of the magnetic signature. Note that mainly the effect produced by currents flowing in the ionosphere is accounted for in this calculation, with a smaller component due to the 'reflection' of the magnetic perturbation in the perfectly conducting Earth. Conspicuous features, both in the horizontal and vertical components, are observed under the auroral electrojets shown in Figure 6.4. Note that strong horizontal perturbations coincide with huge gradients of the vertical component of the magnetic field, though this latter component is not necessarily large locally.

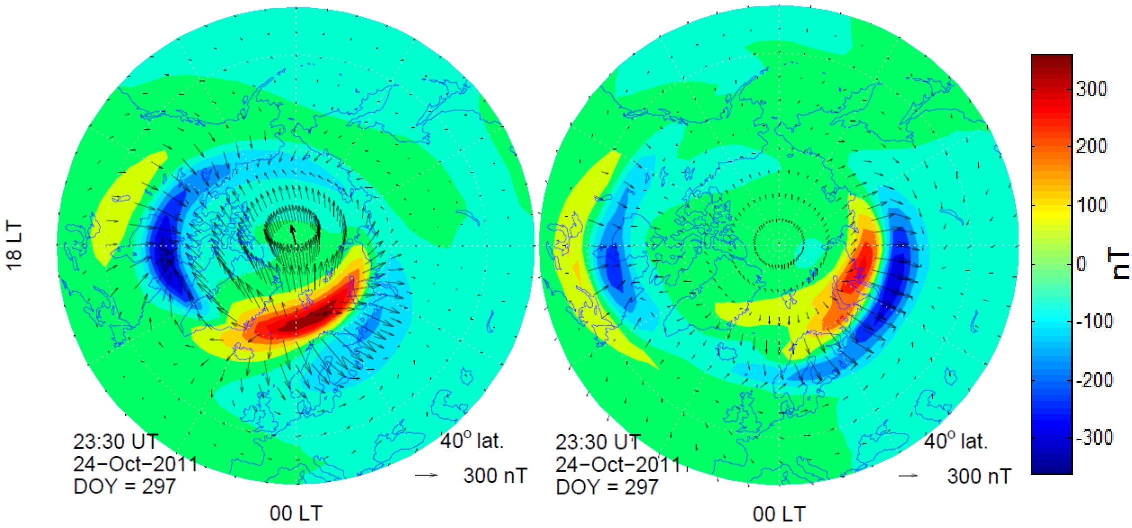

Figure 6.6. Maps showing the ground magnetic signatures of currents essentially flowing in the ionosphere for the magnetically disturbed day October 24, 2011, at 23:30 UT. The left panel corresponds to the output of the standard version, while the right panel corresponds to the output of the AMPERE-driven version. Geodetic coordinates are used.

The left panel of Figure 6.6 shows the ground magnetic perturbation field consistent with the standard version of the TIE-GCM for October 24, 2011, at 23:30 UT. The right panel shows the same quantity obtained using our full approach. The figure is aimed at giving an impression on how different magnetic signatures are in both cases, which correspond with the field-aligned currents shown in Figure 6.3. The reason why the standard model gives larger magnetic perturbations than the AMPERE-driven version must be associated with the highly concentrated sectors of Birkeland currents in the former case, peaking at values up to 4 times larger than the latter (see Figure 6.3). The broader latitudinal extent of the AMPERE currents, on the other hand, helps explain the spread of the magnetic perturbations to lower latitudes in our approach.

6.2.3. VALIDATION RESULTS

Figure 6.7 shows plots of the ground magnetic signatures at the location of the four observatories used to validate the model (see Table 3) for the six analyzed periods. This would give rise to 24 (= 6 periods × 4 observatories) plots, though only a subset is shown here, again selected obeying illustrative purposes and so that the 6 periods and the 4 observatories are represented. The upper subplot of each panel corresponds to the *X* or north component; the middle one to the *Y* or east component, and the lower one to the *Z* or vertical component. The black line represents the observed variations at the observatory in question; the red and blue lines represent the output of the standard and AMPERE-driven (full approach) versions of the TIE-GCM, respectively.

As specified in section 4.2.2, to drive the standard TIE-GCM we have made use of the $F_{10.7}$ index to parameterize the solar radiation, and the time-varying K_p index to parameterize both the auroral HP and the CPCP of the *Heelis et al.* [1982] model at absolute magnetic latitudes above 75˚. The effect of neutral winds is ignored at these latitudes. Below 60˚ magnetic latitude, the electric field is calculated by the dynamo model. Between 60˚ and 75˚ magnetic latitude (north and south), there is a smooth transition between the dynamo solution and the imposed high-latitude solution.

The periods displayed, normally one day long, correspond to the most disturbed interval of the period in question (the least in the case of the quiet period). Concerning the AMPERE-driven TIE-GCM, results for LIV observatory, in Antarctica, are obtained using the southern-hemispheric (SH) solution of equation (4.2), while the NH solution has been used for the others. As for the depth of the perfect conductor, it has been set to 250 km for Tromsø (TRO) and College (CMO), while a depth of 600 km has been used for Ebre (EBR) and LIV due to their magnetic latitudes (this selection applies to both, the standard and the AMPERE-driven model versions).

Figure 6.8, which is valid for the October 2011 storm, is similar to Figure 6.7, though only the X component at TRO observatory is displayed to highlight the details. The magnetic bays starting at 23:10 UT, when the observatory was close to local midnight, are related to the significant westward current given by the model at QD latitude around 65˚ (see Figure 6.4*c*). The first large bay at TRO is only partially reproduced by our model, though the second one, occurring around 04:00 UT on October 25, is notably reproduced. The large observed magnitude of these bays, especially the first one, is a clear sign of substorm occurrence (M. Nosé, personal communication, 2012). This is supported by ground-based observations of the Auroral Electrojet (AE) index, among others [*Nosé et al.*, 2012], and by Pi2 pulsations observed at EBR and LIV geomagnetic observatories around 23:02 UT [*Blanch et al.,* 2013].

Table 4 shows the model performance P (defined in section 6.1) for each of the 24 (= 6 periods × 4 observatories) cases analyzed. We show P for both, the standard model and our full approach. Note that P actually has three components, one for each component of the magnetic variation vector, i.e., P_X, P_Y and P_Z. Thus, for example, $P_X = 10$ for the standard model at CMO observatory on August 4, 2010, while it increases to 31 in our approach. Also note that the observatories (rows) have been arranged by absolute QD magnetic latitude, while the analyzed periods (columns) have been arranged by their A_p index according to Table 2, decreasing from left to right.

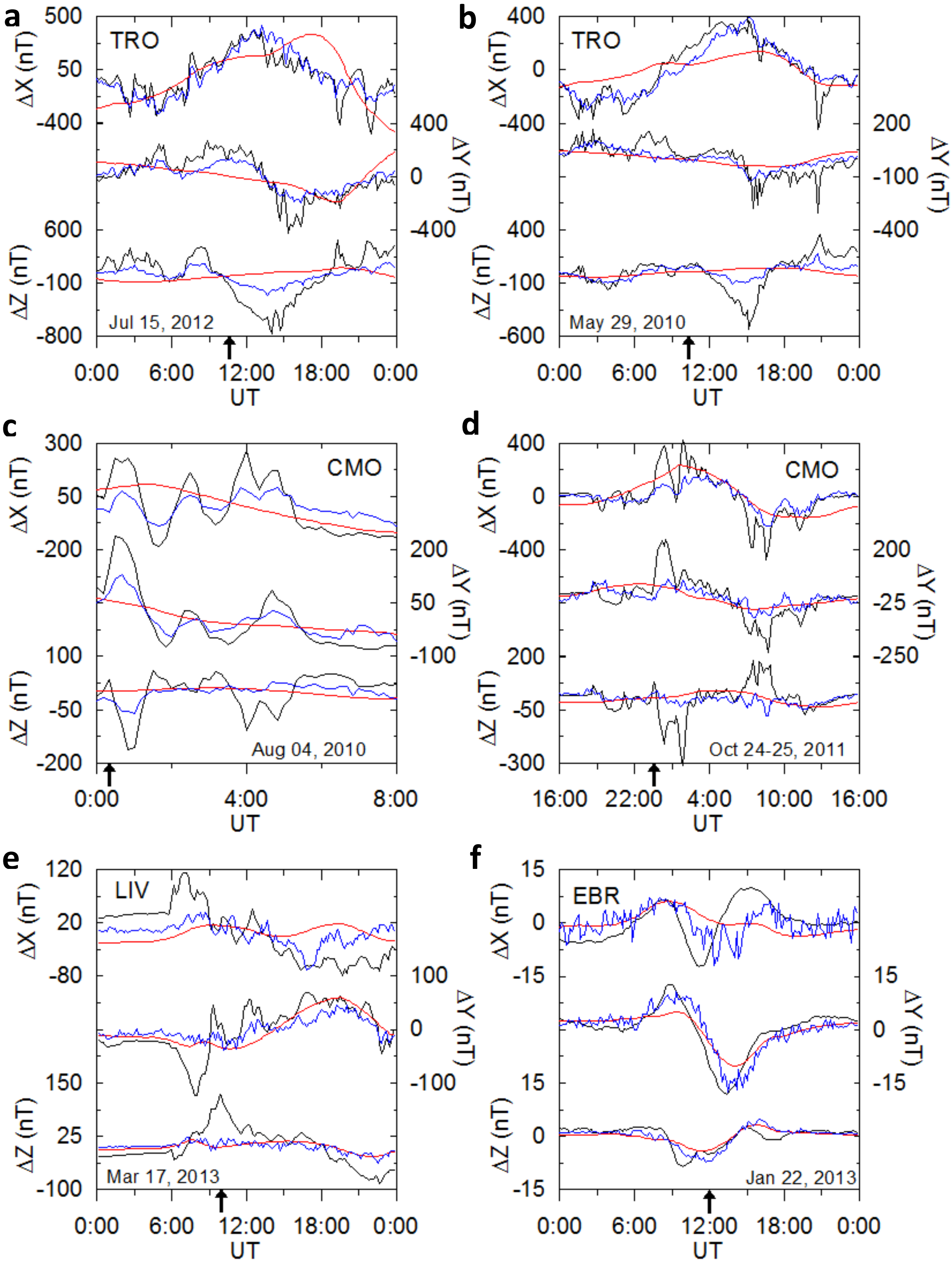

Figure 6.7. Ground magnetic signatures at the location of the observatories used to validate our model. The upper, middle and lower subplots of each panel correspond to the *X*, *Y* and *Z* components of the magnetic variations, respectively. The black line corresponds to the observed variation at the observatory in question, while the red and blue lines represent the standard and AMPERE-driven (full approach) versions of the TIE-GCM, respectively. The periods displayed correspond to the most disturbed interval (the least in the case of the quiet period), and an arrow in the time axis of each panel indicates the particular time displayed in Figures 6.4 and 6.5. Note that the average has been subtracted to each curve so as to make them comparable.

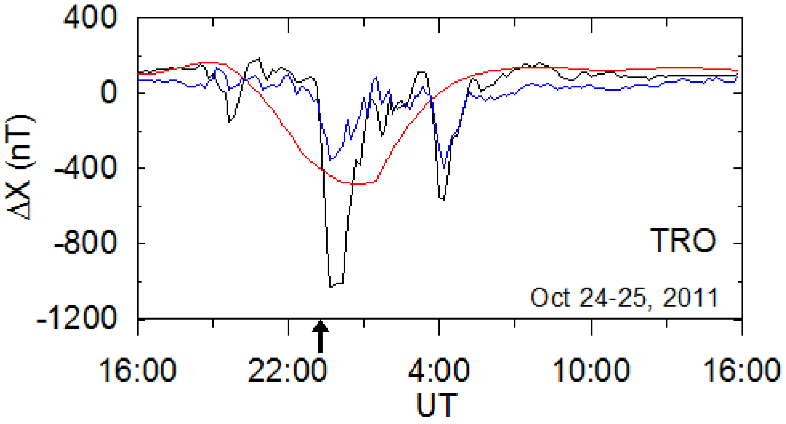

Figure 6.8. Northward component of the ground magnetic signature at TRO observatory for the disturbed 24-h period starting on October 24, 2011 at 16:00 UT. The meaning of the three lines is the same as that for Figure 6.7. The arrow in the time axis, in this case, indicates the approximate beginning of the substorm.

Table 4. Model Performance P Used as a Validation Means$^{a, b}$

		July 15, 2012		March 17, 2013		October 24-25^{c}, 2011		August 04, 2010		May 29, 2010		January 22, 2013	
Obs.	Comp.	Std	AMP	Std	AMP	Std	AMP	Std	AMP	Std	AMP	Std	AMP
TRO	P_X	*-8*	*48*	*-5*	*35*	*25*	*36*	*35*	*46*	*29*	*61*	**22**	**-144**
	P_Y	*15*	*48*	*-3*	*16*	**16**	**10**	*33*	*39*	*13*	*31*	*-54*	*-36*
	P_Z	*-7*	*30*	*-2*	*17*	*-32*	*25*	*-11*	*12*	*-5*	*26*	*-45*	*-25*
CMO	P_X	*19*	*43*	*11*	*36*	*29*	*39*	*10*	*31*	*15*	*46*	**-54**	**-100**
	P_Y	*11*	*40*	*-13*	*19*	*24*	*31*	*22*	*49*	*8*	*26*	**0**	**-18**
	P_Z	*-15*	*16*	*-12*	*12*	*-5*	*-2*	*-7*	*12*	*-11*	*2*	**5**	**-2**
LIV	P_X	*-6*	*7*	*-8*	*20*	**-8**	**-26**	*3*	*23*	*12*	*23*	**48**	**11**
	P_Y	*23*	*34*	**28**	**26**	*24*	*30*	*19*	*37*	*10*	*34*	**52**	**48**
	P_Z	*7*	*24*	*15*	*17*	*26*	*36*	**5**	**0**	*6*	*18*	**22**	**15**
EBR	P_X	*3*	*11*	**20**	**17**	*-59*	*-24*	**0**	**-3**	*1*	*17*	*-11*	*-8*
	P_Y	*17*	*35*	0	0	*24*	*29*	**38**	**13**	**35**	**13**	*47*	*49*
	P_Z	**17**	**16**	*12*	*13*	**-7**	**-14**	**14**	**4**	**23**	**10**	*30*	*39*

[a] "Std" stems from standard model; "AMP" from AMPERE-driven model (full approach).

[b] Values in *italic* script denote improvement of the AMPERE-driven model with respect to the standard version; boldface indicates worsening.

[c] P values in this case are given for a 24-hour period starting on October 24, 2011, at 16:00 UT.

Italic and boldface script in Table 4 helps identify improvement or worsening, respectively, of our full approach with respect to the standard model. As discussed below, one can easily check that improvement largely dominates throughout the table, though worsening takes over, in general, as one approaches the bottom and the right portions of it, corresponding to increasingly lower (absolute) latitudes and quieter periods.

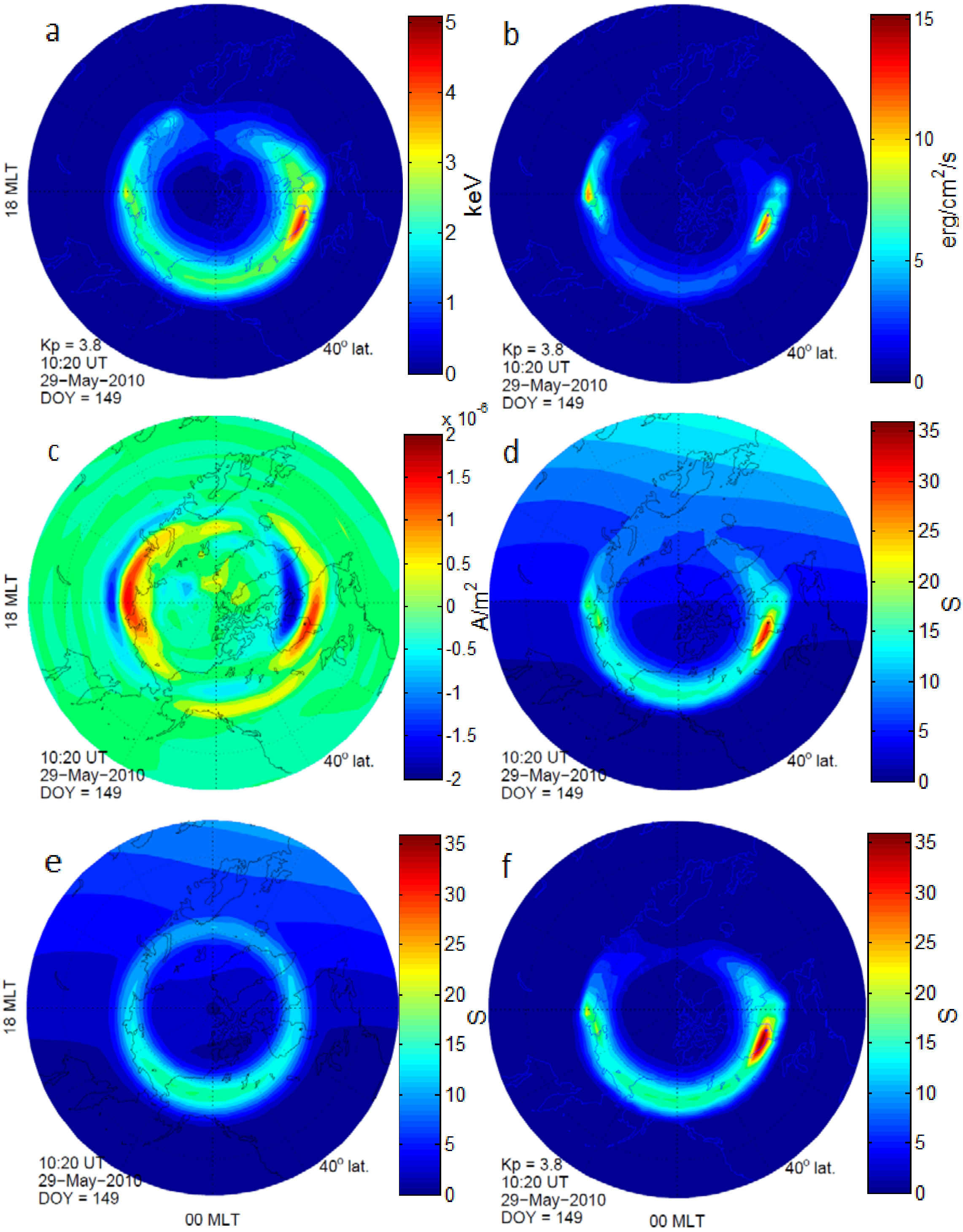

Figure 6.9. Set of electrodynamic quantities relative to the auroral zone during the moderately disturbed conditions occurring in May 29, 2010 at 10:20 UT. (*a*) characteristic energy α [keV] associated with auroral precipitating electrons; (*b*) associated energy flux Q [erg/cm^2/s]; (*c*) AMPERE field-aligned currents [A/m^2]; (*d*) Hall conductance [S] yielded by the TIE-GCM using conductivities consistent with field-aligned currents; (*e*) same quantity yielded by the standard TIE-GCM [S]; and (*f*) same quantity given by the *Robinson et al.* [1987] model [S]. QD coordinates are used.

Figure 6.9 presents a subset of maps showing electrodynamic quantities relative to the auroral zone during the disturbed conditions present in May 29, 2010 at 10:20 UT. Panels (*a*) and (*b*) have been obtained from the expressions summarized in Table 1 (section 5.3) using the AMPERE field-aligned currents shown in panel (*c*), and the Zhang & Paxton model for the given K_p. According to our model, enhanced energy deposition is observed in the dawn and dusk sectors of the auroral zone, connected to conspicuous upward currents (precipitating electrons; red areas). A maximum value of the characteristic energy α of the precipitating electrons circa 5 keV is obtained in the pre-dawn sector (panel (*a*)), corresponding to a mean energy above 9 keV. This is a considerably large value of the mean energy, though values of several ten keV have been reported during severe conditions [*Hargreaves*, 1992]. The corresponding value of the energy flux associated with particle precipitation is about 13 erg/cm^2/s (= 13 mW/m^2; panel (*b*)). Panels (*d*), (*e*) and (*f*) show the auroral zone Hall conductance distribution using different approaches. In particular, panel (*d*) is calculated using our full approach, i.e., conductivities consistent with AMPERE field-aligned currents; panel (*e*) is obtained by the standard TIE-GCM; and panel (*f*) is obtained using the model of *Robinson et al.* [1987]. Note the conductance enhancement of the AMPERE-consistent model (panel (*d*)) with respect to the standard model (panel (*e*)) in the dawn and dusk sectors of the auroral oval. The *Robinson et al.* [1987] semi-empirical model (panel (*f*)) shows results that are in good agreement with our model (panel (*d*)), though with slightly more prominent features.

We now turn to a systematic comparison of our conductance distributions with those yielded by the two independent models exposed above, i.e., *Marklund et al.* [1988] and *Robinson et al.* [1987]. To that aim, figures 6.10 through 6.13 present the following pattern: the upper left panel (*a*) shows the AMPERE currents used to drive the TIE-GCM; the upper right panel (*b*) shows the conductance enhancements following the method of *Marklund et al.* [1988]; the lower left panel (*c*) shows the same quantity following the method of *Robinson et al.* [1987]; and the lower right panel (*d*) shows the conductance distributions obtained with our full approach. Note, as mentioned above, that the *Robinson et al.* [1987] method is not completely independent from ours, since both of them start from the same values of the characteristic energy and energy flux of the precipitating electrons (by means of Table 1). We also note that we have displayed only the conductances meant to be consistent with magnetic field-aligned currents in the method of *Marklund et al.* [1988], leaving aside those conductivities arising from EUV radiation, as well as diffuse and background (e.g., GCR) precipitation; this explains the narrower appearance of the conductance distribution in this case. The method of *Robinson et al.* [1987] also ignores the EUV-induced conductance, though not the diffuse one.

Figure 6.10 presents results for the Hall conductances concerning the May 29, 2010 disturbed period, specifically at 10:20 UT. In this sense, panels (*a*), (*b*) and (*d*) are the same as those presented in Figure 6.9. Figures 6.11 and 6.12 show the results for August 04, 2010, at 13:20 UT, and October 24, 2011, at 19:00 UT, respectively. Finally, Figure 6.13 applies to the Pedersen (rather than Hall) conductance. We note in this context that the TIE-GCM does not give the height-(or field-line) integrated Pedersen conductivity as an output, but rather the east-east and north-north components of the ionospheric conductance tensor (see formulas 5.13 and 5.14 of *Richmond* [1995b]).

These expressions have a geometric factor multiplying the Pedersen conductivity, arising from the non-dipolar form of the Earth's magnetic field, which can deviate from unity by as much as 25 % in the auroral zone. Fortunately, however, the mean of the east-east and north-north Pedersen components is a good measure of the height-integrated Pedersen conductivity, and this is indeed the quantity that has been used for comparison purposes with the other two models.

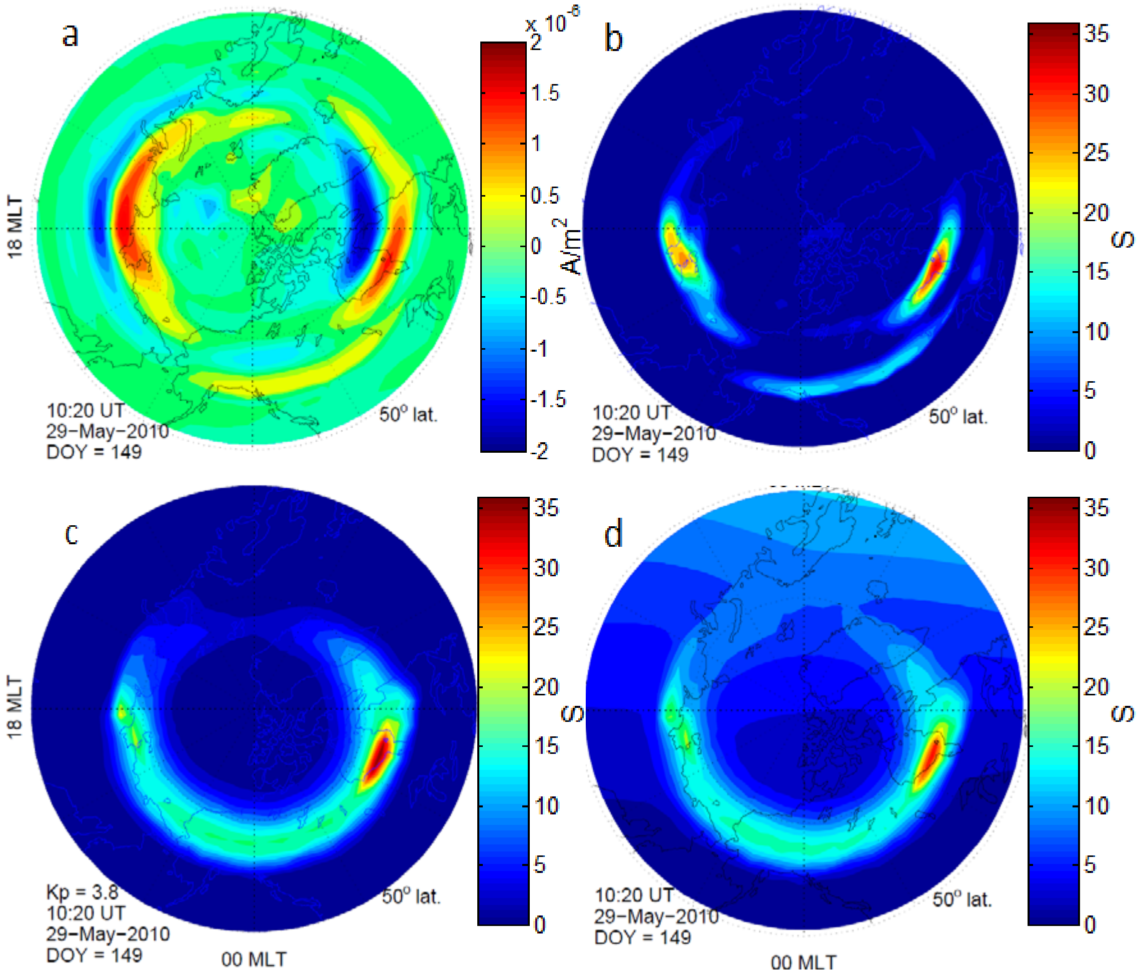

Figure 6.10. Set of electrodynamic quantities relative to the conditions occurring in May 29, 2010 at 10:20 UT. (*a*) AMPERE field-aligned currents [A/m^2]; (*b*) Hall conductance [S] associated with field-aligned currents yielded by the *Marklund et al.* [1988] model; (*c*) Hall conductance given by the *Robinson et al.* [1987] model [S]; (*d*) same quantity yielded by the TIE-GCM using conductivities consistent with field-aligned currents [S]. Note the conductance enhancement in the pre-dawn sector of the three models. QD coordinates are used.

Due to the fact that the TIE-GCM is a physical model, a number of quantities (e.g., temperatures, densities, electric potentials, currents, conductivities, …) are calculated from first principles in a self-consistent manner, allowing the corresponding outputs to be obtained, which in turn can be used to make a diagnosis of the modeled period, or used to validate the model if observations of those quantities are available. As an example, Figure 6.14 shows two other outputs related to the moderately disturbed conditions occurring on May 29, 2010 at 10:20 UT. Its panel (*a*) shows a map of the

TEC, which is the height-integrated electron density in the ionosphere over a given location. Panel (*b*) shows the height-integrated Joule heating power loss (see section 3.2) due to Pedersen currents flowing in the ionosphere in response to an established electric field. In both cases the model has been driven using our full approach. We observe enhanced features of these two quantities at the dawn and dusk sectors of the auroral oval, consistent with the enhanced ionization produced by electron precipitation in these zones (compare with Figure 6.9).

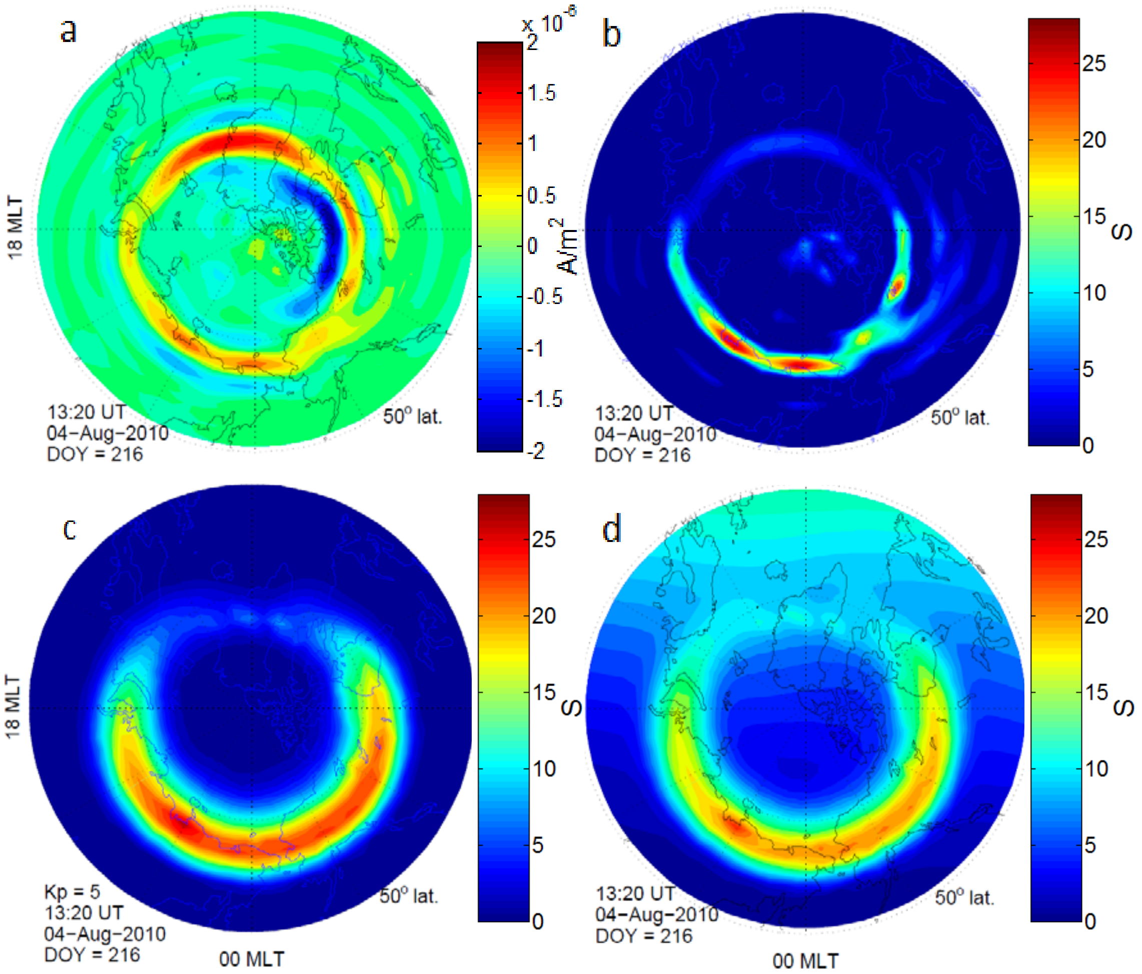

Figure 6.11. Set of electrodynamic quantities relative to the conditions occurring in August 04, 2010 at 13:20 UT. (*a*) AMPERE field-aligned currents [A/m^2]; (*b*) Hall conductance [S] associated with field-aligned currents yielded by the *Marklund et al.* [1988] model; (*c*) Hall conductance given by the *Robinson et al.* [1987] model [S]; (*d*) same quantity yielded by the TIE-GCM using conductivities consistent with field-aligned currents [S]. Note the conductance enhancement in the pre-midnight sector of the three models. QD coordinates are used.

Besides those presented throughout the current chapter, many other ionospheric parameters are available by the TIE-GCM. Some of the most important are enumerated here: electron, different species', and total 3-D density profiles; neutral, ion and electron temperatures; height of the electron density peak of the F2 layer (*hmF2*), including its peak density (*NmF2*) and critical frequency (*foF2*); 3-D electric field (in geographic and magnetic coordinates); 3-D horizontal current density; ion drag coefficient; molecular thermal conductivity and viscosity; pressure scale height; ion $\vec{E} \times \vec{B}$ drift and neutral velocities; total heating rate and cooling rate of different atmospheric species; diffusion coefficient; etc.

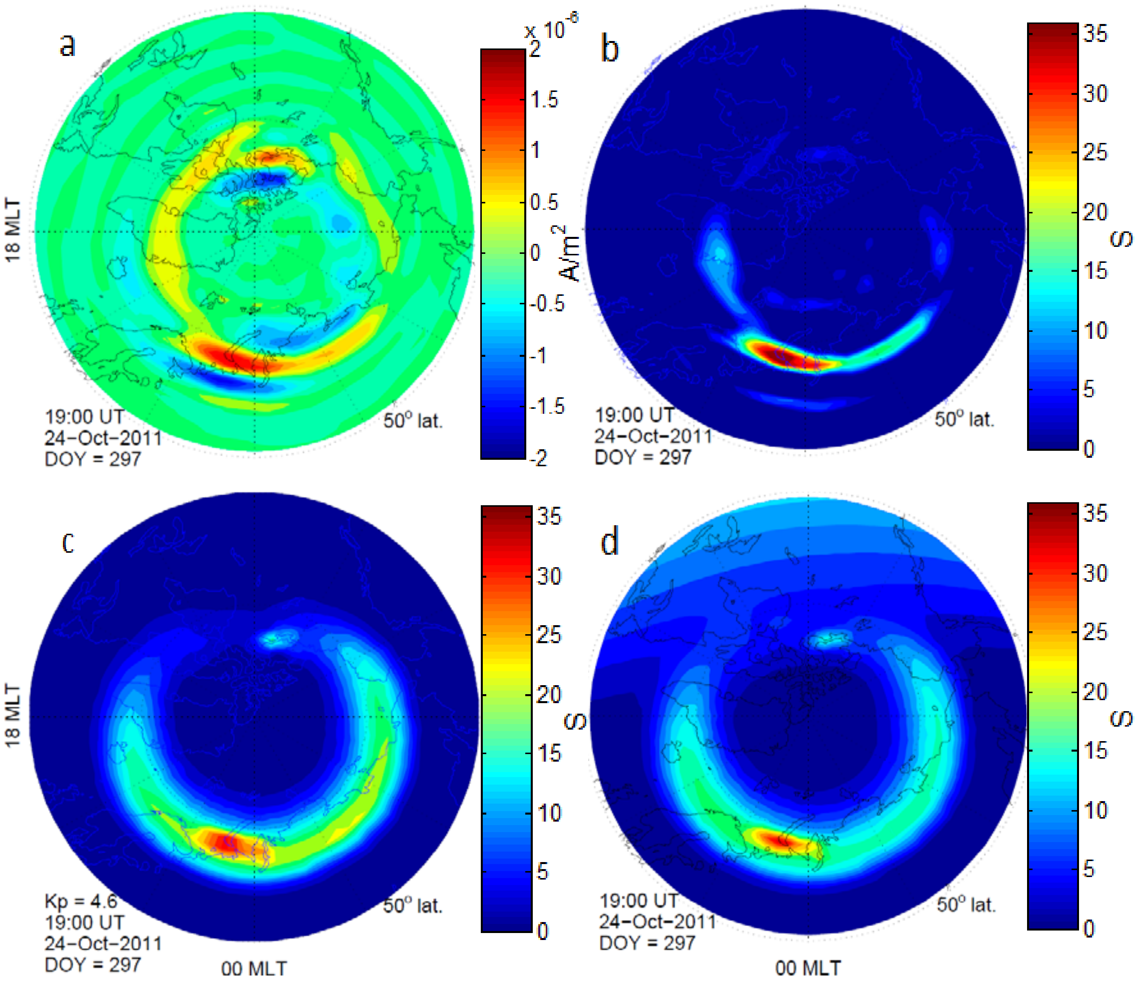

Figure 6.12. Set of electrodynamic quantities relative to the conditions occurring in October 24, 2011 at 19:00 UT. (*a*) AMPERE field-aligned currents [A/m^2]; (*b*) Hall conductance [S] associated with field-aligned currents yielded by the *Marklund et al.* [1988] model; (*c*) Hall conductance given by the *Robinson et al.* [1987] model [S]; (*d*) same quantity yielded by the TIE-GCM using conductivities consistent with field-aligned currents [S]. Note the conductance enhancement in the pre-midnight sector of the three models. QD coordinates are used.

6.3. DISCUSSION

In this section we thoroughly discuss and provide physical interpretations on the results presented in the previous section, especially regarding the methods of model validation. We start with the ground magnetic signatures presented in Figure 6.7 and the related Table 4, and continue with an analysis of the auroral quantities presented in figures 6.9 through 6.13, which are representative of the approach that has been applied for the first time in this work.

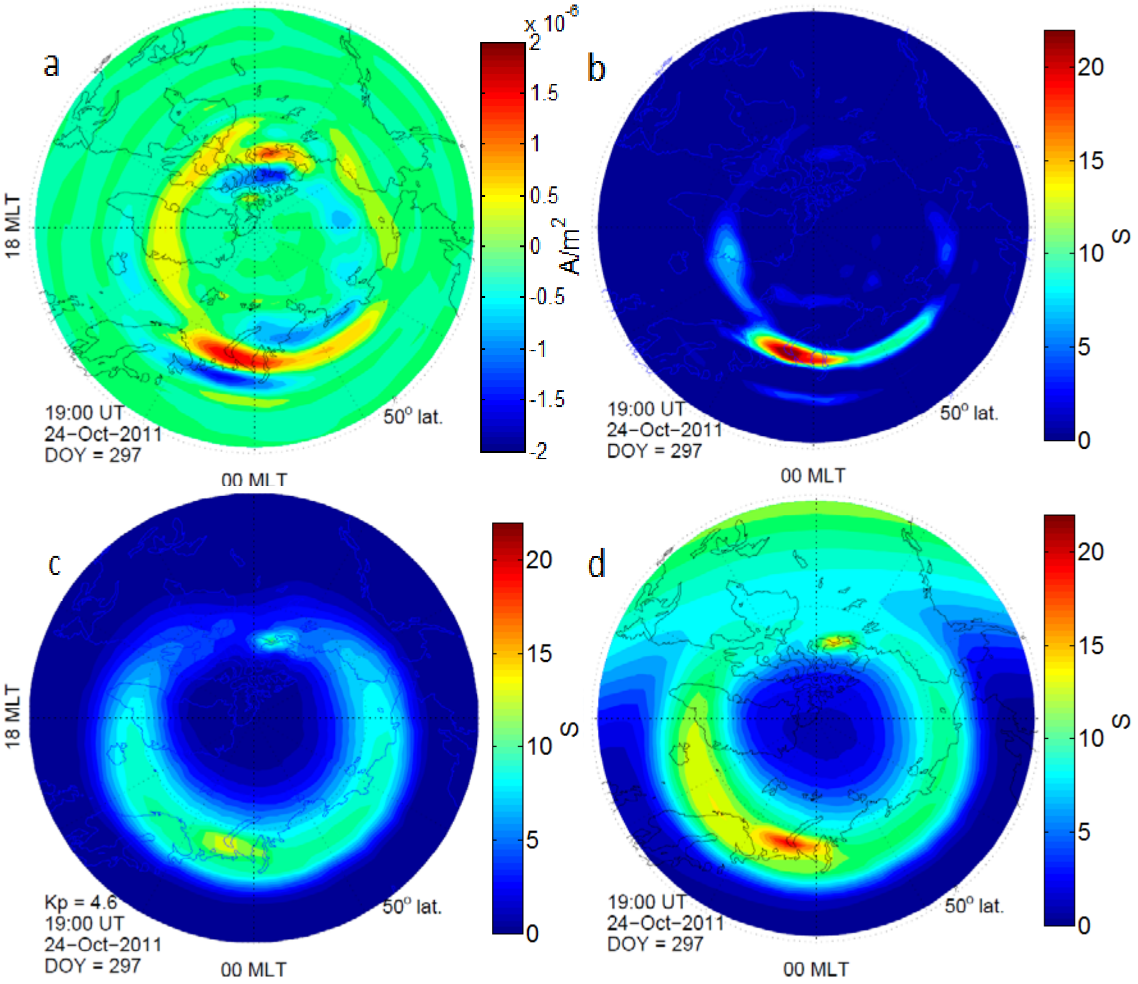

Figure 6.13. Set of electrodynamic quantities relative to the conditions occurring in October 24, 2011 at 19:00 UT. (*a*) AMPERE field-aligned currents [A/m^2]; (*b*) Pedersen conductance [S] associated with field-aligned currents yielded by the *Marklund et al.* [1988] model; (*c*) Pedersen conductance given by the *Robinson et al.* [1987] model [S]; (*d*) same quantity yielded by the TIE-GCM using conductivities consistent with field-aligned currents [S]. Note the conductance enhancement in the pre-midnight sector of the three models. QD coordinates are used.

The red line in the subplots of Figure 6.7 shows the modeled magnetic perturbations using the standard TIE-GCM. This is observed to reproduce, to a certain extent, the slow variations of the magnetic field, especially during the highly disturbed conditions of panel (*d*). However, magnetic variations with periods shorter than 6–8 h are not reproduced by the standard TIE-GCM. This is also the most notable difference between the AMPERE-driven and the standard TIE-GCM, and can be explained by the use of indices with a low temporal resolution in the standard version, like K_p or the $F_{10.7}$ solar flux, from which the magnetospheric conditions are updated with a maximum frequency of 3 h (at least for the Heelis mode, see section 4.2.2) compared with the 10-minute resolution of the AMPERE-driven version. As for quiet conditions, the ability of the standard model to reproduce the observed variations at EBR (panel (*f*)) is acceptable, though the amplitude of the horizontal components (i.e., *X* and *Y*) is underestimated.

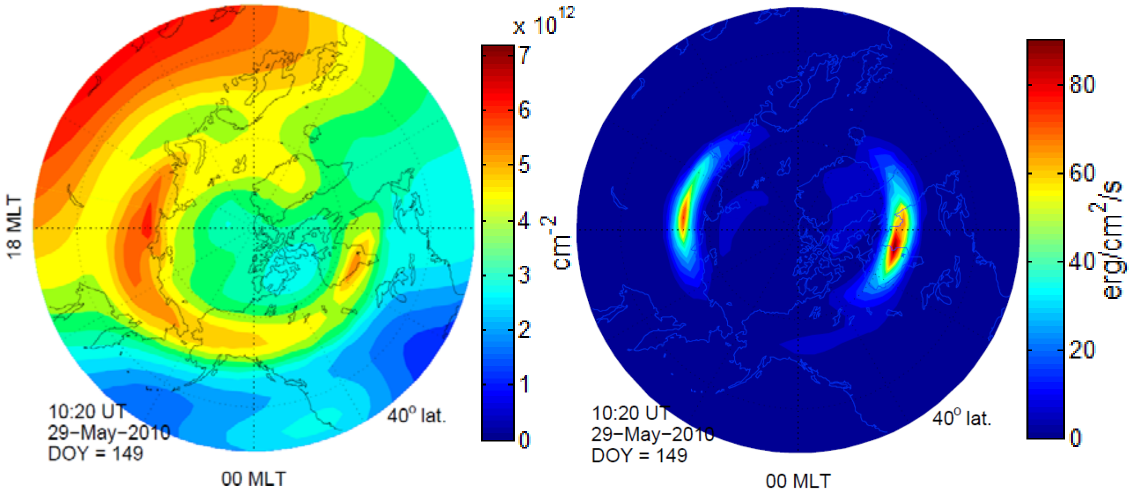

Figure 6.14. (Left) TEC [cm^{-2}]; (right) height-integrated Joule heating power loss [erg/cm^2/s] over the northern polar cap during the moderately disturbed conditions occurring in May 29, 2010 at 10:20 UT. QD coordinates are used.

A mean performance value P of 17 % is obtained by averaging the AMPERE-driven results of Table 4 (columns with header AMP only), compared to an 8 % for the standard model (columns with header Std). However, in general, and regarding the AMPERE-driven model, high latitudes and high disturbance levels exhibit better agreement with observations than midlatitudes and quiet periods. This can be observed in Table 4, where (considering only columns with header AMP) the figures tend to increase as we approach the upper left corner. If we only consider the two high-latitude observatories and the five disturbed periods instead, the model performance rises to 29 %, which we consider to be more meaningful, as these are the situations which we are more interested in (recall that we included a quiet period and two midlatitude stations for completeness purposes). Such a tendency, if any is observed at all, seems to be reversed in the case of the standard model, for which a mean performance of 5 % is attained in the same conditions. As a result, the improvement of the AMPERE-driven model (full approach) with respect to the standard model is generally higher for increasingly higher (absolute) latitudes and disturbance levels, amounting to 24 % (= $\bar{P}_{AMP} - \bar{P}_{Std}$, where the bar stands for the average of the three magnetic elements) if we again consider disturbed conditions and high latitudes. This can also be easily observed in Table 4, where *italic* characters, denoting improvement of our approach with respect to the standard version, dominate in the upper left corner. The reason of such a behavior is due to the fact that the AMPERE currents used to drive the model in our approach play a more important role under these conditions, i.e., auroral latitudes during disturbed periods.

The quality of our high-latitude modeling is also substantiated in panels (*a*) and (*b*) of Figure 6.7, where magnetic bays are reproduced to a great extent, and in panels (*c*) and (*d*) in a lesser degree. However, magnetic variations are clearly underestimated by our model even at high latitudes. The TIE-GCM conductivity distribution in *Marsal et al.* [2012] and *Blanch et al.* [2013], which represents a good approximation for many purposes, was modeled at high latitudes as in the standard model, i.e., from empirical relations like the one connecting the planetary K$_p$ index with HP. However, the introduction of real Birkeland current data from the AMPERE mission gives rise to higher space-time resolution structures of ionization that were not necessarily accounted for by those broader, mean empirical relations. Such fine structures should have a correspondence with localized ionization structures in the TIE-GCM, but that was not generally the case in the mentioned articles. This was indeed one of the conclusions of the paper of *Marsal et al.* [2012]. In this sense, it was pointed out that an underestimated Hall-to-Pedersen conductance ratio (Σ_H/Σ_P) caused by an overestimated Pedersen conductance in a given zone leads to reduced electric fields and Hall currents. This situation would eventually lead to an underestimated ground magnetic variation, for which Hall currents are held mostly responsible (see section 2.5). Conversely, high field-aligned current forcing in areas with a high Hall-to-Pedersen conductance ratio leads to relatively enhanced values of those quantities. The demand for an auroral particle precipitation pattern consistent with the field-aligned current forcing was claimed in the conclusion of the aforementioned article. And this is precisely what we have carried out in the approach presented for the first time in this work, as extensively detailed in section 5.3. The results, however, are rather modest. Comparison of the outcome of the modified TIE-GCM with and without conductivities consistent with field-aligned currents (not presented here) shows an improvement of the former method amounting to an overall 8 % increase in the performance parameter P; the associated standard deviation being 24 % as deduced from the statistics. In other words, the improvement of the present method with respect to the one from *Marsal et al.* [2012] is fairly small, and highly depends on the magnetic component (*X*, *Y* or *Z*) and the particular case being analyzed. Unexpectedly, if we restrict ourselves to disturbed periods and high latitudes, the improvement is even worse, reducing to just 3 %.

As for quiet-time currents, previous TIE-GCM modeling of the ionospheric wind dynamo [*Doumbia et al.,* 2007] has shown that the standard version of the model gives general agreement with observed magnetic perturbations, but is not accurate in detail. Uncertainties in model parameters and inputs like atmospheric tides prevent better agreement. On the other hand, the noisy appearance of the AMPERE-driven model (blue lines) in panel (*f*) of Figure 6.7 is a common feature of quiet periods and it probably reflects inherent errors in the AMPERE data, as this noise does not appear when the model is run in standard mode (red lines). Another possibility pointed out by *Marsal et al.* [2012] to explain such noise is the procedure that we have followed to filter the AMPERE currents for input to the TIE-GCM. As noted in section 5.1, in order to avoid unlikely high electric potentials, the AMPERE currents in *Marsal et al.* [2012] and *Blanch et al.* [2013] were suppressed where the hemispheric field-line integrated Pedersen conductivity is lower than 2 S. To discard the latter possibility, we have used a more progressive filter in the present approach (as suggested by B. J. Anderson, personal communication, 2012), though the noise is still appearing practically unchanged. Note, however, that this noise, typically about 5 nT in amplitude, is probably not restricted to quiet periods, and it probably goes unnoticed in the other panels of Figure 6.7, where the observed magnetic perturbations are much larger. It is also worth noting here that the right and bottom part of Table 4, which shows a worsening of the AMPERE-driven TIE-GCM with respect to the standard version, is mainly due to this noise.

The horizontal components of the magnetic variations, and in particular the *X* component, are better reproduced than the *Z* component. This is especially clear in panels (*c*), (*d*) and (*e*) of Figure 6.7, where practically no correlation exists between observed and modeled *Z* variations (this applies to both, the standard and the AMPERE-driven versions). Restricting ourselves to high latitudes and disturbed conditions, average values of the model performance P for the *X*, *Y* and *Z* components are 42 %, 31 % and 15 %, respectively (deduced from Table 4). The reasons for this defect in the vertical component may be diverse. On the one hand, this magnetic element is subjected to strong horizontal gradients, especially along the (magnetic) meridians under the auroral zone, peaking at nearly 1 nT/km (see Figure 6.5). If we combine this fact with inaccuracies arising from the limited resolution of AMPERE data, which is about 3° in magnetic latitude, we get an estimated inaccuracy of a few hundred nanoteslas, which could explain, at least partially, the discrepancies reflected in the high-latitude disturbed conditions of Figure 6.7. Another possible cause could be related to the approximations made to calculate the induced currents in the solid Earth. Unlike the horizontal magnetic field components, for which the induced currents reinforce the external variations, these currents partially cancel the external variations of the *Z* component, thus leaving greater percentage residuals derived from possible model inaccuracies. The fact that the *X* component gives better results than *Y* is somewhat surprising, since the magnetic effects of magnetospheric current systems like the ring current and the Chapman-Ferraro current, which should have the maximum repercussion on the *X* component, are not accounted for in the model. On a separate note, the neglect of such currents can explain some other features, like the Sudden Storm Commencement (SSC) reported by the international service on rapid magnetic variations (www.obsebre.es/en/rapid) and not modeled in the *X* component of LIV on March 17, 2013 at 05:59 UT (see panel (*e*) in Figure 6.7), corresponding to a compression of the magnetopause by the solar wind.

As mentioned above, the simplified treatment of induced Earth currents in the model, consisting of a perfect conductor below a certain depth and an insulator above, limits its diagnostic capability, as each frequency in the spectrum of natural magnetic variations should correspond to a different effective depth. *Marsal et al.* [2012] showed that the model is indeed quite sensitive to the selection of this parameter.

In some cases, as in the *Y* component of panel (*b*), the *Z* component of panel (*c*), the *Y* and *Z* components of panels (*d*) and (*e*), and the *Z* component of panel (*f*) in Figure 6.7, the variations given by the standard TIE-GCM are similar to the slowly varying component of the magnetic field given by the AMPERE-driven TIE-GCM, in such a way that the rapid variations contributed by the AMPERE data are superimposed to the slow variations provided by the standard model. Such slow variations generally underestimate the real variations.

Following *Knight*'s [1973] theory, intense field-aligned currents flowing upward above the auroral zone ionosphere, corresponding to energetic electrons precipitating from the magnetosphere, are linked to known electric potential drops between these two regions. Such accelerated electrons produce ionization when they hit the upper atmosphere, thus increasing the local conductivity. Panels (*a*) and (*b*) of Figure 6.9 show the characteristic energy and the energy flux, respectively, associated with these electrons during an event of relatively intense such currents, represented in panel (*c*). The associated Hall conductance distribution consistently calculated by the TIE-GCM using our full approach, which is depicted in panel (*d*), shows enhancements in the dawn and dusk sectors matching the highest upward current densities in panel (*c*). Such conductances show a good qualitative and quantitative agreement with those obtained by application of the expressions obtained by *Robinson et al.* [1987] (panel (*f*)), with relative differences below about 15 %. We note here, to be precise, that the *Robinson et al.* [1987] model is meant to provide the height-integrated conductivity distribution, whereas the TIE-GCM gives the hemispherical field-line integrated conductivity. However, the latter should not be more than 4 % higher than the former in the auroral zone (which results in less than 2 S in the present case). The origin of such a good agreement could probably be explained by the fact that both models seem to ultimately rely on energy deposition codes derived by M. H. Rees (among other authors), e.g., *Rees* [1963] for the *Vickrey et al.* [1981] model (which is closely related to that of *Robinson et al.* [1987]), and *Roble and Rees* [1977] for the TIE-GCM. Finally, the standard model (panel (*e*)) shows a more uniform auroral enhancement, which is insensitive to the AMPERE field-aligned current input by reason of the fact that it reflects average conditions for a given K_p.

Figures 6.10 through 6.12, referred to the Hall conductance, again show a notable agreement between the method of *Robinson et al.* [1987] and ours (corresponding to panels (*c*) and (*d*), respectively). The agreement is also satisfactory with the method of *Marklund et al.* [1988] (panel (*b*)), though in general the latter gives the highest values (10 % to 20 % higher). Figures 6.11 and 6.12 show conductivity enhancements in the pre-midnight sector, which is the zone where the discrete aurora dominates, as reported by *Newell et al.* [1996]. Figure 6.13, on the contrary, confirms that a significant difference exists between the methods of *Marklund et al.* [1988] and *Robinson et al.* [1987] as far as the Pedersen conductance is concerned. This controversy was indeed predicted in section 6.1.2 (see Figure 6.2 and associated text). Our method (i.e., our full approach, panel (*d*)), however, usually gives an intermediate value, as in the present case.

The fact that our full approach does not provide a qualitative step forward in terms of the ground magnetic signature with respect to the basic AMPERE-driven TIE-GCM (i.e., with conductivities *not* consistent with field-aligned currents) deeply concerns us. As stated above, an insignificant 3 % improvement is observed when high latitudes and disturbed conditions are considered. A possible reason for this weakness could be connected to the fact that the conductance enhancements introduced by our full approach, though they are in reasonably good agreement with the independent models of *Robinson et al.* [1987] and *Marklund et al.* [1988], are relatively local in nature, i.e., they affect localized regions of the auroral oval (see figures 6.9 through 6.13) and are usually limited in time to a few tens of minutes. Because we have used two auroral geomagnetic observatories to validate our model, the chance of coincidence of the conductivity enhancement crossing above any of the two observatories is relatively low.

A second possibility could be related to the neglect of protons (and heavier ions) in our approach of conductivities consistent with magnetic field-aligned currents. To evaluate their impact, *Galand and Richmond* [2001] analyzed the contribution of proton precipitation to ionization and electrical conductance with a proton transport code and showed that this component can be significant (or even more important than the electron component) at particular times and locations, mainly at the equatorward boundary of the auroral oval before midnight and at the cusp region. As in *Robinson et al.* [1987], they find expressions relating the mean energy $\bar{E}^p$ and energy flux Q^p of the precipitating protons with the associated ionospheric Pedersen, Σ_P^p, and Hall, Σ_H^p, conductances (compare with (6.3)):

$$\Sigma_P^p = 5.7{Q^p}^{1/2}; \qquad \frac{\Sigma_H^p}{\Sigma_P^p} = 0.45{\bar{E}^p}^{0.3}. \tag{6.5}$$

The typical range of proton mean energies is 2 keV to 40 keV; however, as stated by the authors, the total auroral energy flux of protons, Q^p, represents on the average about 15 % that of electrons. Assuming these average values and substituting them in (6.3) and (6.5), we obtain $\Sigma_P^p < 0.6\Sigma_P$ and $\Sigma_H^p < 0.4\Sigma_H$ (where Σ_P and Σ_H are the electron contributions). Considering that the total perpendicular conductances associated with particle precipitation, Σ_P^{tot} and Σ_H^{tot}, are approximately the root-mean-square of the different contributions, we get $\Sigma_P^{tot} = \sqrt{{\Sigma_P}^2 + {\Sigma_P^p}^2} < 1.16\Sigma_P$ and $\Sigma_H^{tot} = \sqrt{{\Sigma_H}^2 + {\Sigma_H^p}^2} < 1.08\Sigma_H$. This change in the conductances may have an effect on the solution for the electric potential, and thus on the rest of electrodynamic variables, especially where proton precipitation dominates. However, because the relative change in conductance is quite small in average, and because proton-induced changes in conductance are important in regions where the underlying conductances and currents are weak, the effect on magnetic perturbations may be small and our approach is expected to be sufficiently good.

A third possibility could be related to the fact that Zhang & Paxton's formulation of the energy flux is dependent on the K_p index solely, whereas *Korth et al.* [2014] show a dependence of that quantity on the IMF orientation. On the other hand, this latter paper points out that the *Knight*'s [1973] formulation is more suitable at the afternoon upward R1 sector, meaning that the relation of field-aligned currents to mean energy and energy flux in that zone would apply even below the Zhang & Paxton threshold.

A last possibility could again be connected with the limited resolution of both, AMPERE data and the TIE-GCM itself: unlike diffuse aurora, discrete auroral events are features with typical latitudinal thicknesses ranging from hundreds of meters to tens of kilometers (e.g. *Gurnett* [1972], based on satellite data, *Hargreaves* [1992], or *Prölss* [2004]), associated with characteristic energies up to several tens of keV. Furthermore, they undergo rapid temporal variations and appear to move at velocities up to a few ten km/s. Such small scales are far below the resolution not only of AMPERE satellites, but also of the TIE-GCM grid, and are thus likely to be smoothed out by the background surrounding conditions. Note, in connection with this fact, that we obtain typical values of the characteristic energy below about 5 keV, compared to reported values up to 40 keV for the highest energies [*Hargreaves*, 1992]. We suggest that bombardment of the auroral upper atmosphere by highly accelerated particles would eventually produce localized ionization enhancements and conducting filament structures invisible by the model but enabling Hall currents to flow, thus producing noticeable magnetic effects on the ground. This, along with the localized nature of the conductivity enhancements, could be a candidate responsible for the small sensitivity of the TIE-GCM in response to making ionospheric conductivities consistent with the AMPERE field-aligned current input.

7. SUMMARY, CONCLUSIONS AND FUTURE GUIDELINES

In this last chapter we offer a perspective view of the present work, including a summary and the most relevant conclusions. We also put it into a context and comment on its contribution to the knowledge of the upper atmosphere sciences. The chapter is closed with some future guidelines.

7.1. SUMMARY AND CONCLUSIONS

Marsal et al. [2012] and *Blanch et al.* [2013] used for the first time real field-aligned current data to drive the high-latitude electrodynamics in an upper-atmosphere general-circulation model. This forcing is external to this kind of models, and it must otherwise be modeled by other means, insofar as it plays an important role to the global ionospheric dynamics, and especially to the high latitudes. Modeling this input by use of different indices available to the space science community (e.g. K_p and/or IMF orientation), however, introduces additional uncertainties. The real currents used in the above articles prevent this shortcoming to occur, as these data are indeed used as an input to the model, subsequent quantities being consistently computed from it. The fact that the TIE-GCM is an upper atmosphere (rather than a magnetosphere) model justifies this election, allowing for a more direct, higher space-time resolution representation of the ionospheric electrodynamics. The approach used in our previous papers has been extended in this work to include a feedback between this input and the ionospheric conductivity which has been shown to be in reasonable agreement with two independent models accounting for particle precipitations. Field-aligned current data provided by the AMPERE satellite mission proves suitable for these purposes.

We have successfully used the radial component of field-aligned currents given by the AMPERE satellite mission to specify the high-latitude electrodynamic inputs to the TIE-GCM. We have presented results for twenty-four different scenarios (6 periods × 4 observatories) comparing our model results with real geomagnetic observatory data and with the standard version of the TIE-GCM (i.e., not driven with AMPERE data); these comprise different levels of magnetic disturbance, from highly disturbed to completely quiet; and four different locations, from middle to high latitudes, during the period comprised between May 2010 and March 2013, for which AMPERE data are available. We have also checked our conductivity model by comparing it with other two independent models. Our results show the following general conclusions:

1. Unlike the standard TIE-GCM, which may use two different empirical approaches to establish the electrostatic potential at high latitudes based on geophysical indices, our approach considers the dynamo effect of neutral winds even at these highest latitudes. The resultant electric potentials and ground magnetic perturbations are reasonable, even if they are imperfect representations of observations. The modeled magnetic variations can explain 29 % (parameter P) of the observed variations at high latitudes during disturbed conditions, versus a 5 % corresponding to the standard TIE-GCM. This implies that our approach is capable to explain circa 6 times more of the real variation than the standard TIE-GCM.

2. There exist, however, different reasons why our results differ from the observations; some are highlighted here:

    a) Firstly, and probably more importantly, because of their intrinsic limitations, models are inevitably imperfect representations of reality. This might appear an obvious and worthless statement; however, we recall in this context that the TIE-GCM is a model based on first principles, and a qualitative improvement, though it is not necessarily accompanied by an exact matching with real data in quantitative terms, implicitly involves an advance in our understanding of the physics of the underlying problem.

    b) Secondly, and regarding the ground magnetic signatures in particular, the TIE-GCM is mainly intended to account for the contribution of ionospheric currents to the overall magnetic perturbations. The field-aligned current contribution (which is magnetospheric in a strict sense), for example, is simplified in the model, as it assumes dipole field-lines.

    c) An even coarser approximation is used when it comes down to the currents induced in the Earth's surface, which has a finite and spatially varying conductivity in reality. Induced Earth currents significantly affect the modeled ground magnetic perturbations. The use of a perfectly conducting layer at a fixed depth is inadequate and a more complete model should account for the Earth's 3-D conductivity structure.

    d) No account is made of currents flowing in other parts of the magnetosphere (e.g., ring current, magnetopause and magnetotail), which are definitely important during the disturbed conditions that we are mainly concerned with in this work. We have made a crude estimation of the expected maximum performance attainable by the model because of the inaccuracies stated in the above points *b*, *c* and *d*, adding up to a (conservative) value around 75 - 80 % of the performance parameter P. Considering that the mean performance that we have attained at high latitudes during disturbed conditions is 29 %, we get a real performance of the purely ionospheric model amounting to 37 %, which reduces to about 23 % if we consider the whole range of latitudes and conditions.

   e) A less important reason could be related to the limited resolution of AMPERE data. The space and time coverage provided by the Iridium satellites is unprecedentedly good in this type of measurements, offering an effective picture of the global distribution of field-aligned currents every 10 minutes with a latitudinal resolution of 3˚ and a longitudinal resolution of 36˚. However, this is comparable to the size of the large-scale field-aligned structures during disturbed periods (i.e., the R1 and R2 rings); and the overall configuration of these currents could vary substantially during this time interval as well. As a result, the Birkeland currents available from the AMPERE database could be missing some valuable information, especially during disturbed conditions, which are the most important to us. On the other hand, *Knipp et al.* [2014] reported a limited knowledge of the AMPERE spacecraft-attitude, which propagates to the associated data. Finally, the ringing effect inherent to AMPERE data as a result of data processing could also be misleading. We have checked the consistency of the globally integrated upward and downward radial field-aligned currents, I_{AMP}^{up} and I_{AMP}^{dn} (which is negatively defined), respectively, given by AMPERE, and they are seen to agree reasonably well, i.e., their sum is nearly zero, as desirable, within a 3 % average error (i.e., $\left|\left(I_{AMP}^{up}+I_{AMP}^{dn}\right)/\left(I_{AMP}^{up}-I_{AMP}^{dn}\right)\right| \cong 0.03$). Concerning the TIE-GCM itself, in this work we have used a high resolution (varying with latitude) geomagnetic grid, a double resolution geodetic grid of 2.5° × 2.5°, and a model time step of 1 minute, i.e., all of them below the AMPERE resolution. This finite resolution is believed to play a minor role in our results; evidence of this is that our present outcome does not change substantially with respect to that of *Marsal et al.*, [2012], where a standard geodetic resolution of 5° × 5° and a time step of 2 minutes were used.

3. We have used an increased X-ray flux input in our model version with respect to the standard one. This is supported by other authors and introduces a modest improvement in our performance.

4. The introduction of AMPERE data has revealed some weaknesses of the TIE-GCM. In particular, the use of the IGRF as the base magnetic field model is acceptable at low and middle latitudes, but not so suitable for high-latitude field-lines extending far out into the magnetotail. This region of space distorts the magnetic field-lines, and mapping into the upper atmosphere turns out not to be trivial. The issue arises from the fact that the standard TIE-GCM makes a hemispherically symmetric treatment of some key electrodynamic quantities; in particular, the electrostatic potential is supposed to be symmetric about the (IGRF-derived) equator; however, some field-aligned current patches as recorded by the AMPERE satellites (and assuming that these data are exempt from errors) do not incise on the same precise conjugate latitudes of the two hemispheres. This results in a smoothed potential being output by the model, and a correspondingly biased electrodynamics. To avoid this, a modification was introduced in the code to solve the electrodynamo equation separately for each hemisphere, though this involves other approximations that are inexact at middle and low latitudes. These are referred to in the main text as NH and SH solutions of the electrodynamo. A more physically consistent treatment of

hemispherically asymmetric electrodynamics in the TIE-GCM would thus be encouraged.

5. Our treatment of hemispherically asymmetric electrostatic potentials inherent to the NH and SH solutions also allows for an electric potential drop along magnetic field-lines, which otherwise would be treated as equipotential. This is consistent with our latter (or full) approach, which considers conductivities resulting from electrons being accelerated by field-aligned electric fields.

6. The new TIE-GCM conductance model, which has extended the standard version to make it consistent with the AMPERE field-aligned currents, proves successful if we compare it with two well-known and independent models that account for the effects of particle precipitation in the upper atmosphere. The idea behind this approach lays on the generally accepted assumption that regions of the auroral ionosphere subjected to enhanced upward field-aligned currents (as measured by the AMPERE fleet) are affected by a correspondingly enhanced conductance, mainly due to ionization production by precipitating electrons.

7. In general terms, and regarding the ground magnetic field, our results improve those of the standard TIE-GCM by about 9 % (from 8 % to 17 %) attending to the mean performance parameter P. Such an improvement is more manifest as we approach high latitudes during disturbed conditions, for which a mean increase of 24 % in P is attained (from 5 % to 29 %). The latter is connected to the fact that the field-aligned currents introduced by the AMPERE driving are more relevant in these situations.

8. Most of the improvement mentioned in the previous point has its origin in the application of AMPERE data in the TIE-GCM, rather than making the auroral conductivities consistent with field-aligned currents. In this sense, although our conductivities compare well with those obtained from two independent models, improvement has proven practically insignificant in terms of the ground magnetic signature, especially at high latitudes during disturbed conditions, where the results were expected to improve more clearly. The idea behind this attempt has been exposed above, though the details of the process are more controversial; in particular: what the relationships are between the geomagnetic field-aligned currents and the energy and number flux of precipitating electrons; how are these particles distributed in terms of their energy; or to what extent auroral conductivity enhancements are necessarily linked to field-aligned currents, among others. The response of the ionosphere, and therefore the ground magnetic signatures output by the model, will generally depend on what these constraints are, and how they are specified in the code. We have carried out a number of tests, e.g., playing with the energy of the incoming electrons, or varying the threshold responsible of the diffuse aurora. Surprisingly, however, the TIE-GCM output shows a great momentum, which makes it reluctant, at some extent, to reflect the changes introduced in the code, though they are indeed perceived as important by the user.

9. Some physical reasons, however, could help explain the ineffectual results of the conductivity enhancements in terms of the ground magnetic variations:

a) Because the conductance enhancements in our approach require electron mean energies and fluxes above the diffuse threshold, they appear as spatially localized and temporally limited patches in the perturbed auroral zone. On the other hand, the altered ionospheric currents flowing in and around these areas of enhanced conductivity mainly affect the ground surface below them. Thus, a reason why our modeled ground magnetic field is apparently insensitive to these conductivity enhancements is probably connected with the relatively low chance of coincidence of such patches with the ionosphere above (or near) the two auroral geomagnetic observatories (TRO and CMO) used for validation purposes.

b) The discrete aurora, the main protagonist of our latter approach, is often a relatively thin and rapidly moving characteristic of the auroral upper atmosphere, with latitudinal scales down to hundreds of meters which cannot be captured by the AMPERE ensemble (nor by the TIE-GCM). Such characteristics would be provoked by highly localized precipitation events, presumably (though perhaps not necessarily) associated with field-aligned currents limited to a small area. The conductivity enhancement produced by these events could give rise to relatively narrow but considerably intense currents which would eventually produce a non-negligible magnetic signature on the ground. The AMPERE satellites would thus average out, or completely lose track of this effect, especially in case that such localized currents turn up in opposite pairs (i.e., upward and downward), since the magnetic effects of each counterpart would then be partially cancelled at heights above the ionosphere.

c) The Hall conductance in our approach is in good agreement with other two models accounting for particle precipitation [*Robinson et al.,* 1987; *Marklund et al.*, 1988]. However, the discrepancy is not minor with respect to the Pedersen conductance, for which these two models themselves yield substantial differences. We have found that the *Marklund et al.* [1988] model gives values systematically higher for the Pedersen conductance than those of *Robinson et al.* [1987], our method giving intermediate values. Although Hall currents are known to be the main responsible of the magnetic signature on the ground, these are determined by the Hall-to-Pedersen conductance ratio in the ionosphere. In consequence, the importance of an accurate Pedersen conductance is not less valuable than an accurate Hall conductance. If the *Robinson et al.* [1987] model turns out to be more realistic than the one by *Marklund et al.* [1988], which seems plausible, our Pedersen conductances would be overestimated, which would lead to underestimated values of both, the Hall-to-Pedersen conductance ratio and the ground magnetic variation, as observed.

d) We have assumed an accelerated Maxwellian distribution function for the incoming electrons, though some authors have postulated other shapes, such as the power law, the exponential, or the monoenergetic distributions. Although some differences could arise from each assumption, the electrodynamics is not expected to depend on this election provided that the correct values of the mean energy and number flux of precipitating electrons is considered.

e) Protons (and other heavier ions) have not been considered at all in our conductivity approach. Though some authors have stressed the role of proton precipitation in producing localized ionization and conductivity enhancements in the auroral ionosphere, the weight of this component, averaged over the total auroral zone, is believed to be less than 40 % with respect to the electron component as far as Hall conductance is concerned, implying a maximum of 8 % increase in the total Hall conductance. A 16 % increase is expected in correspondence with the Pedersen conductance. Although this may have an effect on the resultant potential distribution and ultimately on the ground magnetic perturbations, the inclusion of proton precipitation is not expected to change our results significantly, especially during disturbed conditions, when the electron component dominates. Our treatment of auroral protons in terms of conductivity is relegated to that made by the standard TIE-GCM.

10. The use of AMPERE data, fed into the model every 10 minutes, improves the temporal resolution of the TIE-GCM output. This results in a better representation of magnetic signatures at high latitudes and for increasing disturbance levels. For quiet conditions, the AMPERE-driven model introduces a significant level of noise. Concerning the slow magnetic field variations, there is a tendency of the AMPERE-driven TIE-GCM to show the same weaknesses as the standard TIE-GCM.

11. The AMPERE-driven TIE-GCM has a diagnostic, rather than a prognostic value. The fact that the AMPERE currents are measured close to the Earth (when their effects are practically occurring) prevents a forecasting analysis of the events, which would be highly valuable for warning purposes related to severe space weather episodes. Both the AMPERE data availability, together with the time needed for the TIE-GCM to execute, also impose temporal limitations for the nowcasting benefits of our approach. The last data available from the AMPERE website corresponds to May 2013, when the associated project expired, although the Iridium satellite mission is still in service. The so-called Iridium-NEXT, a subsequent generation of the Iridium satellites, is expected to begin in 2015, and the entire constellation will be refreshed in 2017. The new spacecraft are planned to carry improved magnetometer systems and will measure the magnetic field associated with field-aligned currents with a higher space-time resolution (see presentation by *Anderson et al.* [2013]).

7.2. FUTURE GUIDELINES

Future efforts will be focused on improving several aspects pointed out in the previous points. In particular, a qualitative leap forward in the quality of the ground magnetic signature would consist in the introduction of a finite, at least 1-D Earth conductivity model. Still related to the geomagnetic field modeling, it seems quite feasible to implement the effects of a magnetospheric partial ring current closing the symmetric field-aligned current in the TIE-GCM, instead of having it flow radially to or from infinity. This could be effected by the ionospheric equivalent of a complementary current system restricted to the equatorial plane, also flowing from or to infinity but in the opposite sense. Inclusion of protons in the conductivity enhancement consistent with AMPERE field-aligned currents could also be considered, though effective relationships between such currents and the mean energy and flux of these particles should be known.

We have implemented our method to just two auroral observatories: CMO and TRO. For our conclusions to be more significant, however, we need to extend our study to a greater number of auroral geomagnetic observatories or even magnetometer arrays, e.g., the International Monitor for Auroral Geomagnetic Effects (IMAGE; http://www.ava.fmi.fi/image/) or the Canadian Array for Real-time Investigations of Magnetic Activity (CARISMA; http://www.carisma.ca/).

An immediate exercise that will be carried out is the comparison of our conductance distributions with observations. The most accurate estimates correspond to incoherent-scatter-radar measurements of the E-region electron densities, which can be combined with a neutral-atmosphere model to get conductivities. We are especially interested in facilities that are located in the auroral zone or nearby, like Poker Flat (Alaska) and Sondrestrom Fjord (Greenland), whose data are available in the Madrigal database (http://cedar.openmadrigal.org/). Conductances can also be inferred from observations of auroral particle precipitation, either direct (e.g., DMSP satellites) or indirect (e.g., inferences from TIMED/GUVI data). This will allow a real validation of our conductance model, since the comparison presented in this work is indeed made with respect to two alternative models.

SuperDARN (e.g., http://vt.superdarn.org/tiki-index.php) also offers new perspectives for a natural continuation of the present work. Among other datasets, SuperDARN data has already been used for assimilation purposes to obtain the high-latitude electrodynamics by use of the AMIE or similar procedures [*Cousins et al.,* 2013], which in turn has been used to drive the TIE-GCM [e.g., *Shiokawa et al.,* 2007]. In fact, the electrostatic potential deduced from this radar network allows other electrodynamic quantities to follow in an immediate and highly reliable fashion. These data are also valuable for our work, especially from the validation point of view; in particular, the mentioned electrostatic potential distribution yielded by the SuperDARN dataset can be used to check the same quantity as output by the AMPERE-driven TIE-GCM. As in the case of the incoherent scatter radars, this would allow a more direct means to verify our model, since the electric potential is obtained from the AMPERE currents in the very first steps of the electrodynamic algorithm, once in possession of the conductivity and neutral wind distributions (see equation 4.1 or 4.2). The ground magnetic signatures principally used in this work, on the contrary, are not so useful to this end, since numerous intermediate steps and approximations are made in between.

The utility of the geomagnetic field data provided by the newly operational Swarm satellite mission (http://www.esa.int/Our_Activities/Observing_the_Earth/Swarm) for purposes of driving the TIE-GCM model has also been scrutinized; previous analyses on the resolution of Swarm-derived data to yield field-aligned currents show relatively valuable from a local point of view, resolving scales down to 150 km, or equivalently

1.3° in latitude [*Ritter et al.,* 2013]; however, the constellation's limited space coverage, taking circa 1.6 h to wrap the Earth, makes it more suitable for the static internal sources of the magnetic field, rather than for time-varying sources. The fact that it does not offer a snapshot of the global configuration of the field-aligned current system thus limits its value for our purposes. In any case, the joint analysis of Swarm-derived field-aligned current data and ground-based ionospheric characteristics might help refine our auroral conductivity model.

Continuation of the AMPERE mission is important to the upper atmosphere scientific community. 'AMPERE-NEXT', the new generation of data based on the renewed Iridium constellation, is planned to offer an improved dataset through an increased resolution of its measurements and a better knowledge of the spacecraft attitude. This will surely give rise to new implementations and opportunities for future research on space science. Specifically, the limited resolution of the current AMPERE data, which has been identified as a possible weak point in the present work, will hopefully be exceeded by the new generation, and makes it worth a new attempt concerning assimilation into the TIE-GCM.

Finally, we want to stress a fact that has already been pointed out above in this text: the TIE-GCM is an eminently physical, or first-principles model, meaning that it has the merit that the output diagnostic quantities are self-consistently calculated using most of our current knowledge of the upper atmospheric sciences in form of relationships among them. This comprehensiveness, however, is often obtained at the cost of reduced accuracy with respect to empirical models. The practical utility of its output is thus probably lessened at some extent by this fact. However, the TIE-GCM has a huge theoretical value, inasmuch as it makes clear that our current understanding of the upper atmosphere is still incomplete. Evidence of this is the improved, though still far from complete matching of model outputs and observations. Further development of the diverse theoretical aspects of this branch of science is thus required, which must inescapably go hand in hand with an observational basis. The justification of this need, however, is not purely theoretical. We are known to be more vulnerable now (and presumably yet more in the next future) than in previous decades due to space weather phenomena, which poses a serious threat to our continuously developing technology. Understanding of this fact by the funding institutions is thus critical if our society (at least as it is currently understood) is expected to face the future with minimal guarantees of success.

APPENDIX A

Flowcharts of the TIE-GCM electrodynamics:

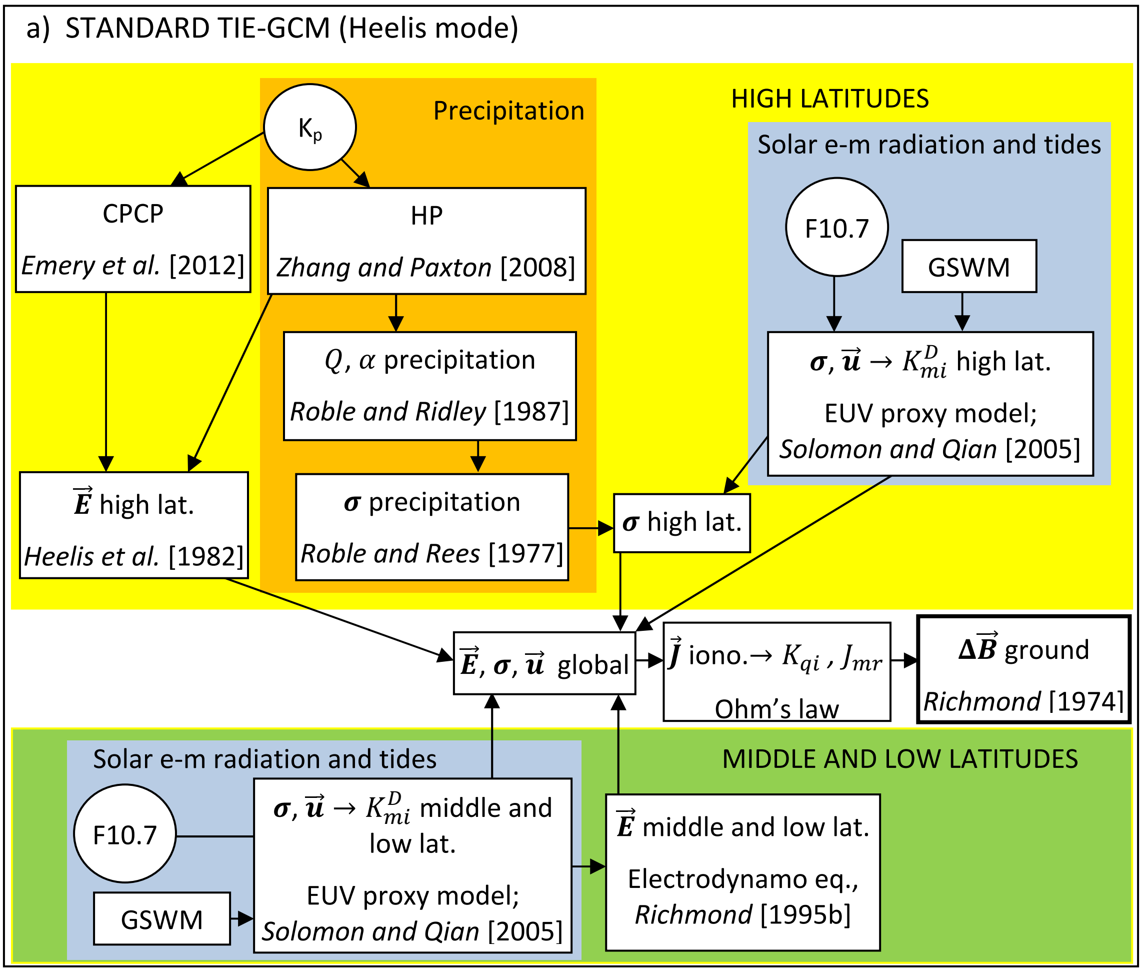

a) STANDARD TIE-GCM (Heelis mode)

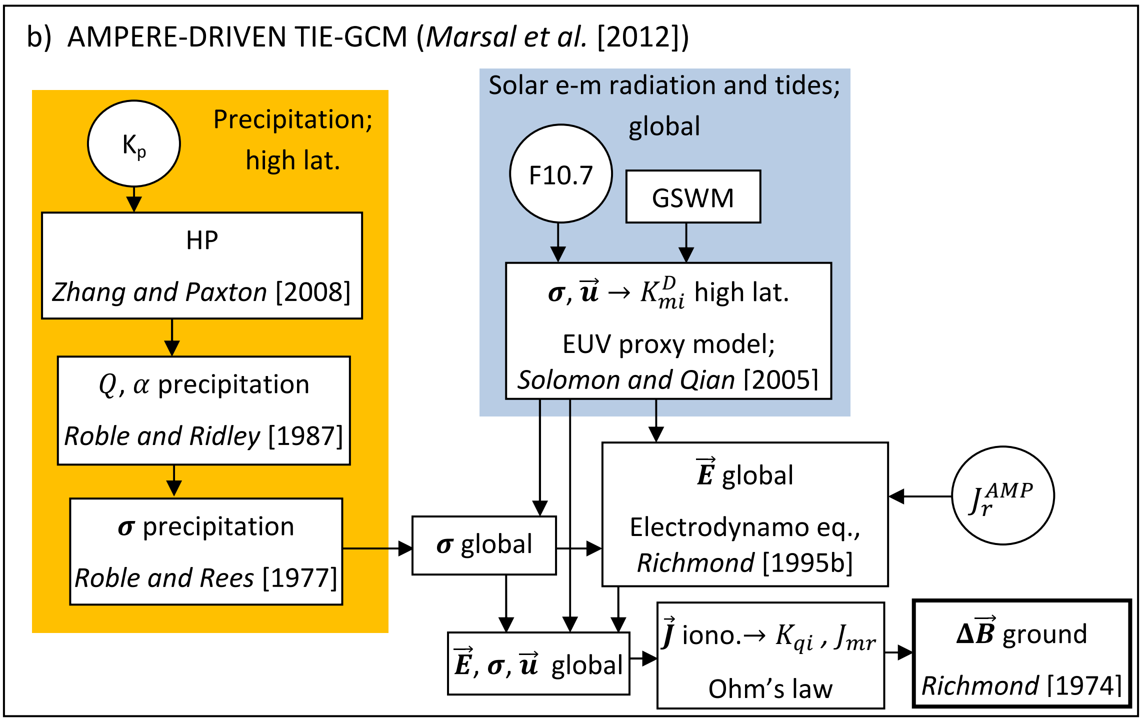

b) AMPERE-DRIVEN TIE-GCM (*Marsal et al.* [2012])

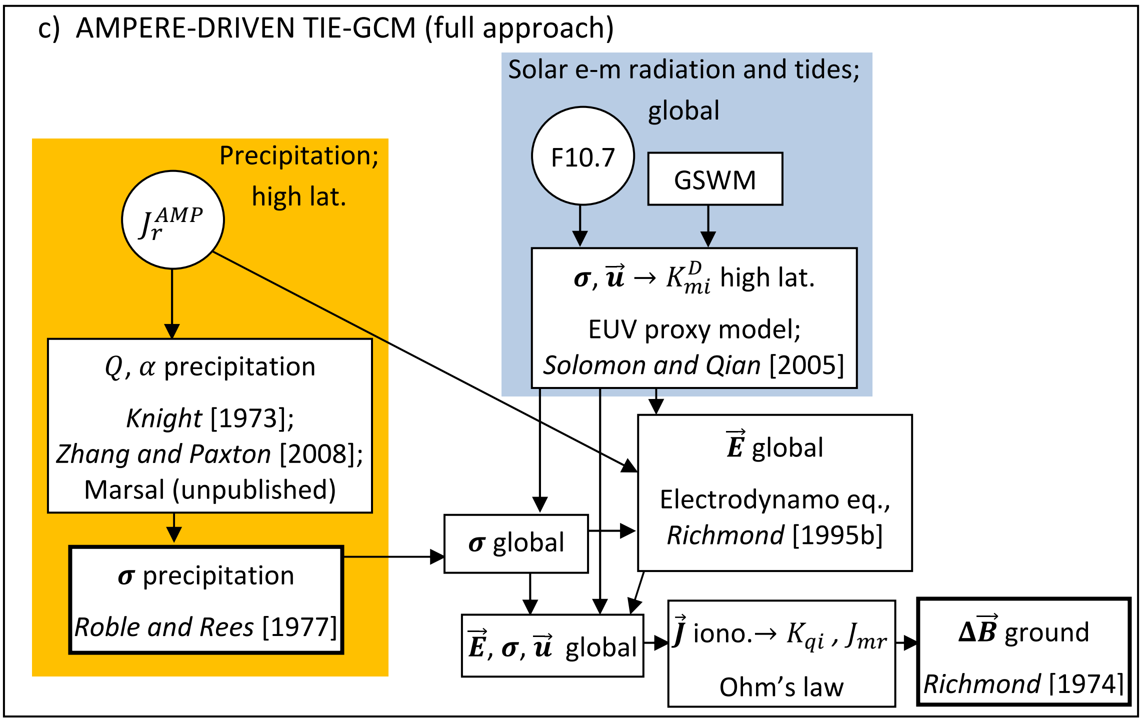

Figure A.1. Diagrams presenting the main flow and computations related to the electrodynamics of the different versions of the TIE-GCM dealt with in this work. Flowchart (*a*) is referred to the standard TIE-GCM; (*b*) makes reference to the AMPERE-driven TIE-GCM with conductivities not consistent with Birkeland currents (*Marsal et al.* [2012]); and finally, (*c*) is related to our full approach of the AMPERE-driven TIE-GCM. Inputs are identified with circles, and outputs for validation purposes with thick-edge boxes. The acronym e-m stands for electromagnetic; the variables are defined somewhere in the main text.

APPENDIX B

Physical constants:

Elementary charge	$e \approx 1.602177 \times 10^{-19}$ A s
Electron mass	$m_e \approx 9.109382 \times 10^{-31}$ kg
Boltzmann constant	$k \approx 1.38065 \times 10^{-23}$ J K^{-1} $\approx 0.86173 \times 10^{-4}$ eV K^{-1}
Speed of light	$c = 2.99792458 \times 10^{8}$ m s^{-1}
Permeability of free space	$\mu_0 = 4\pi \times 10^{-7}$ V s A^{-1} m^{-1}
Permittivity of free space	$\varepsilon_0 = (\mu_0 c^2)^{-1} \approx 8.854188 \times 10^{-12}$ A s V^{-1} m^{-1}
Mean radius of the Earth	$R_E \approx 6.371 \times 10^{6}$ m

Conversion of energy units:

1 erg = 10^{-7} J

1 keV $\approx 1.602177 \times 10^{-16}$ J $= 1.602177 \times 10^{-9}$ erg

APPENDIX C

Number flux, energy flux and mean energy of an accelerated Maxwellian distribution:

The flux of electrons in the ionosphere precipitating from the magnetosphere base is expressed in terms of the number flux density f_s as

$$F_S = \int_{E_k=0}^{\infty} f_s(E_k) dE_k. \tag{C.1}$$

Likewise, the energy flux and mean energy are, respectively,

$$Q = \int_{E_k=0}^{\infty} E_k f_s(E_k) dE_k, \tag{C.2}$$

$$\bar{E} = \frac{Q}{F_S},$$

where the different terms are properly defined in chapter 5, and the integrals are evaluated in the ionosphere base.

Unlike a pure Maxwellian, however, the form of the flux density function f_s of a Maxwellian accelerated by a potential drop $V\ (= \Phi_I - \Phi_S \geq 0)$ and submitted to a varying magnetic field is not straightforward. Energies below eV, for example, are forbidden, so that $f_S(E_k < eV) = 0$. Let $v_\parallel$ be the component of the electron velocity along the ambient magnetic field, taken positive downward, i.e., $v_\parallel = \vec{\boldsymbol{v}} \cdot \vec{\boldsymbol{b}}$ (in the northern hemisphere; $-\vec{\boldsymbol{v}} \cdot \vec{\boldsymbol{b}}$ in the southern), and $v_\perp = \left|\vec{\boldsymbol{v}} \times \vec{\boldsymbol{b}}\right|$ its perpendicular component. It is convenient to write the number flux density in the velocity space as the product of the parallel velocity and the Maxwellian distribution function, $d_s(\vec{v})$ [*Knight,* 1973]:

$$f_s(\vec{v}) = v_\parallel d_s(\vec{v}) = v_\parallel N_S \left(\frac{m_e}{2\pi k T_S}\right)^{3/2} \mathrm{e}^{\frac{eV}{kT_S} - \frac{m_e\left(v_\parallel^2 + v_\perp^2\right)}{2kT_S}}, \tag{C.3}$$

and restrict the domain of integration of (C.1) and (C.2) to S_v (Figure C.1), so that the electron flux, for example, is

$$F_S = \iiint_{S_v} f_s(\vec{v}) d^3 v,$$

where $d^3 v$ is the 3-D volume in velocity space, and S_v accounts for only those ionospheric electrons originating in the magnetosphere base. This excludes the mentioned forbidden velocities, which can be deduced from the principle of conservation of energy and the first adiabatic invariant as discussed below:

The total energy of an electron in the magnetosphere base must be conserved in its way to the ionosphere base. Expressing the total energy, E_T, as the sum of its kinetic and potential components, E_k and E_p, we get

$$E_T^S = E_k^S + E_p^S = E_k^S - e\Phi_S = E_k^I - e\Phi_I = E_k^I + E_p^I = E_T^I, \tag{C.4}$$

where S and I refer to the magnetosphere and ionosphere bases, respectively. On the other hand, from the first adiabatic invariant we know that

$$\frac{(v_\perp^S)^2}{B_S} = \frac{(v_\perp^I)^2}{B_I}. \tag{C.5}$$

Now we express the electron velocity components in terms of its energy and direction, $\frac{1}{2}m_e v_\perp^2 = \frac{1}{2}m_e(v\cos\theta)^2 = E_k\cos^2\theta$; $\frac{1}{2}m_e v_\parallel^2 = \frac{1}{2}m_e(v\sin\theta)^2 = E_k\sin^2\theta$, where θ is the complementary of the pitch angle, or angle that forms the electron velocity with the magnetic field line at each base, so that $\theta = 0$ in the direction perpendicular to the magnetic field, and $\theta = \pi/2$ for a field-aligned velocity facing the ionosphere. Thus (C.5) yields

$$\frac{E_k^S\cos^2\theta_S}{B_S} = \frac{E_k^I\cos^2\theta_I}{B_I}. \tag{C.6}$$

Making use of (C.6), (C.4) can be written as

$$-eV + E_k^I = E_k^S(\sin^2\theta_S + \cos^2\theta_S) = E_k^S\sin^2\theta_S + \frac{E_k^I\cos^2\theta_I}{\beta},$$

or equivalently,

$$-eV + E_k^I\left(1 - \frac{\cos^2\theta_I}{\beta}\right) = E_k^S\sin^2\theta_S. \tag{C.7}$$

The right hand side of (C.7) is a positively defined quantity, so a given value of E_k^I will be possible in the ionosphere if, and only if, it is originated by a corresponding non-negative value of E_k^S. In other words, the possible kinetic energies of ionospheric electrons which have precipitated from the magnetosphere base are those that fulfill:

$$E_k^I \geq eV\frac{\beta}{\beta - \cos^2\theta_I}. \tag{C.8}$$

Likewise, for an electron to plunge from the magnetosphere base, its velocity must necessarily face the ionosphere, which implies $\theta_I \geq 0$, thus defining the domain S_v. Hereafter, we drop the sub- (and super-) script I, though it is implicit in the following instances of v, E_k, and θ, since these quantities are evaluated in the ionosphere base.

From (C.3), the number of electrons in a volume $d^3\vec{v}$ of the velocity space is

$$d_S(\vec{v})d^3\vec{v} = N_S\left(\frac{m_e}{2\pi kT_S}\right)^{3/2} \mathrm{e}^{\frac{eV}{kT_S} - \frac{m_e v^2}{2kT_S}} d^3\vec{v},$$

which, expressed in cylindrical coordinates, yields

$$d_s(\vec{v})d^3\vec{v} = N_S\left(\frac{m_e}{2\pi kT_S}\right)^{3/2} \mathrm{e}^{\frac{eV}{kT_S}-\frac{m_e v^2}{2kT_S}} v^2 \cos\theta \, dv d\theta d\varphi$$

$$= \frac{N_S}{2}\left(\frac{1}{\pi kT_S}\right)^{3/2} \mathrm{e}^{\frac{eV-E_k}{kT_S}} E_k^{1/2} \cos\theta \, dE_k d\theta d\varphi.$$

The differential flux of electrons from the source region is thus

$$f_s(\vec{v})d^3\vec{v} = \frac{N_S}{\sqrt{2m_e}}\left(\frac{1}{\pi kT_S}\right)^{3/2} \mathrm{e}^{\frac{eV-E_k}{kT_S}} E_k \sin\theta\cos\theta \, dE_k d\theta d\varphi,$$

which yields a total number flux

$$F_S = \iiint_{S_v} f_s(\vec{v})d^3v = \frac{N_S}{\sqrt{2m_e}}\left(\frac{1}{\pi kT_S}\right)^{3/2} \mathrm{e}^{\frac{eV}{kT_S}} \iiint_{S_{E\theta}} \mathrm{e}^{-\frac{E_k}{kT_S}} E_k \sin\theta\cos\theta \, dE_k d\theta d\varphi$$

$$= -N_S\sqrt{\frac{kT_S}{2\pi m_e}}\,\mathrm{e}^{\frac{eV}{kT_S}} \iint_{S_{xy}} x\mathrm{e}^{-x} dx dy, \qquad (\mathrm{C}.9)$$

where we have defined $x = E_k/kT_S$, $y = \cos^2\theta$ in the last step, and $S_{E\theta}$ and S_{xy} are the respective domains expressed in terms of the pairs of variables E_k, θ and x, y.

From (C.8) we see that kinetic energies above $eV\frac{\beta}{\beta-1}$ are possible for any incidence angle θ; between eV and $eV\frac{\beta}{\beta-1}$, however, valid energies depend on the angle θ. In the latter interval, for a given E_k the lower limit of the incidence angle, θ_l, fulfills

$$\cos^2\theta_l = \beta\left(1-\frac{eV}{E_k}\right), \qquad (\mathrm{C}.10)$$

which defines an ellipsoid in the velocity space, with semi-major axes $\sqrt{\frac{2eV}{m_e}\frac{\beta}{\beta-1}}$ in the directions perpendicular to the magnetic field, and semi-minor axis $\sqrt{\frac{2eV}{m_e}}$ along the magnetic field (Figure C.1). This and the fact that $\theta \geq 0$ define the limits of integration in the last term of (C.9):

$$\iint_{S_{xy}} x\mathrm{e}^{-x} dx dy = \int_{x=\frac{eV}{kT_S}}^{\frac{eV}{kT_S}\frac{\beta}{\beta-1}} x\mathrm{e}^{-x} dx \int_{y=\beta\left(1-\frac{eV}{xkT_S}\right)}^{0} dy + \int_{x=\frac{eV}{kT_S}\frac{\beta}{\beta-1}}^{\infty} x\mathrm{e}^{-x} dx \int_{y=1}^{0} dy$$

$$= -\beta\int_{x=\frac{eV}{kT_S}}^{\frac{eV}{kT_S}\frac{\beta}{\beta-1}} x\mathrm{e}^{-x}\left(1-\frac{eV}{xkT_S}\right) dx - \int_{x=\frac{eV}{kT_S}\frac{\beta}{\beta-1}}^{\infty} x\mathrm{e}^{-x} dx =$$

$$\begin{aligned}
&= -\beta \int_{x=\frac{eV}{kT_S}}^{\frac{eV}{kT_S}\frac{\beta}{\beta-1}} x\mathrm{e}^{-x}dx + \beta\frac{eV}{kT_S}\int_{x=\frac{eV}{kT_S}}^{\frac{eV}{kT_S}\frac{\beta}{\beta-1}} \mathrm{e}^{-x}dx - \int_{x=\frac{eV}{kT_S}\frac{\beta}{\beta-1}}^{\infty} x\mathrm{e}^{-x}dx \\
&= \beta\frac{eV}{kT_S}\left(\mathrm{e}^{-\frac{eV}{kT_S}} - \mathrm{e}^{-\frac{eV}{kT_S}\frac{\beta}{\beta-1}}\right) \\
&- \beta\left[\left(1+\frac{eV}{kT_S}\right)\mathrm{e}^{-\frac{eV}{kT_S}} - \left(1+\frac{eV}{kT_S}\frac{\beta}{\beta-1}\right)\mathrm{e}^{-\frac{eV}{kT_S}\frac{\beta}{\beta-1}}\right] \\
&\qquad - \left(1+\frac{eV}{kT_S}\frac{\beta}{\beta-1}\right)\mathrm{e}^{-\frac{eV}{kT_S}\frac{\beta}{\beta-1}}, \qquad (\mathrm{C.11})
\end{aligned}$$

where the integrals in the last step have been evaluated with the help of (C.12) and (C.13):

$$\int_{x=a}^{b} \mathrm{e}^{-x}dx = \mathrm{e}^{-a} - \mathrm{e}^{-b}, \qquad (\mathrm{C.12})$$

$$\int_{x=a}^{b} x\mathrm{e}^{-x}dx = (1+a)\mathrm{e}^{-a} - (1+b)\mathrm{e}^{-b}, \qquad (\mathrm{C.13})$$

$$\int_{x=a}^{b} x^2\mathrm{e}^{-x}dx = (2+2a+a^2)\mathrm{e}^{-a} - (2+2b+b^2)\mathrm{e}^{-b}. \qquad (\mathrm{C.14})$$

Simplifying (C.11), we get

$$\begin{aligned}
F_S &= -N_S\sqrt{\frac{kT_S}{2\pi m_e}}\,\mathrm{e}^{\frac{eV}{kT_S}}\iint_{S_{xy}} x\mathrm{e}^{-x}dxdy \\
&= N_S\sqrt{\frac{kT_S}{2\pi m_e}}\left[\beta - (\beta-1)\mathrm{e}^{-\frac{eV}{kT_S}\frac{1}{\beta-1}}\right]. \qquad (\mathrm{C.15})
\end{aligned}$$

The energy flux is evaluated in a similar manner:

$$\begin{aligned}
Q &= \iiint_{S_v} E_k f_S(\vec{v})d^3v = \frac{N_S E_k^2}{\sqrt{2m_e}}\left(\frac{1}{\pi kT_S}\right)^{3/2}\mathrm{e}^{\frac{eV}{kT_S}}\iiint_{S_{E\theta}} \mathrm{e}^{-\frac{E_k}{kT_S}}E_k^2\sin\theta\cos\theta\,dE_k d\theta d\varphi \\
&= -N_S kT_S\sqrt{\frac{kT_S}{2\pi m_e}}\,\mathrm{e}^{\frac{eV}{kT_S}}\iint_{S_{xy}} x^2\mathrm{e}^{-x}dxdy. \qquad (\mathrm{C.16})
\end{aligned}$$

The integral in the last term of (C.16) is

$$\iint_{S_{xy}} x^2\mathrm{e}^{-x}dxdy =$$

$$\begin{aligned}
&= \int_{x=\frac{eV}{kT_S}}^{\frac{eV}{kT_S}\frac{\beta}{\beta-1}} x^2 \mathrm{e}^{-x} dx \int_{y=\beta\left(1-\frac{eV}{xkT_S}\right)}^{0} dy + \int_{x=\frac{eV}{kT_S}\frac{\beta}{\beta-1}}^{\infty} x^2 \mathrm{e}^{-x} dx \int_{y=1}^{0} dy \\
&\qquad = -\beta \int_{x=\frac{eV}{kT_S}}^{\frac{eV}{kT_S}\frac{\beta}{\beta-1}} x^2 \mathrm{e}^{-x} dx + \frac{\beta eV}{kT_S} \int_{x=\frac{eV}{kT_S}}^{\frac{eV}{kT_S}\frac{\beta}{\beta-1}} x \mathrm{e}^{-x} dx - \int_{x=\frac{eV}{kT_S}\frac{\beta}{\beta-1}}^{\infty} x^2 \mathrm{e}^{-x} dx \\
&\qquad = -\beta \frac{eV}{kT_S}\left[\left(1+\frac{eV}{kT_S}\frac{\beta}{\beta-1}\right)\mathrm{e}^{-\frac{eV}{kT_S}\frac{\beta}{\beta-1}} - \left(1+\frac{eV}{kT_S}\right)\mathrm{e}^{-\frac{eV}{kT_S}}\right] \\
&\qquad - \beta\left\{\left[2+\frac{2eV}{kT_S}+\left(\frac{eV}{kT_S}\right)^2\right]\mathrm{e}^{-\frac{eV}{kT_S}} \right. \\
&\qquad \left. - \left[2+2\frac{eV}{kT_S}\frac{\beta}{\beta-1}+\left(\frac{eV}{kT_S}\frac{\beta}{\beta-1}\right)^2\right]\mathrm{e}^{-\frac{eV}{kT_S}\frac{\beta}{\beta-1}}\right\} \\
&\qquad - \left[2+2\frac{eV}{kT_S}\frac{\beta}{\beta-1}+\left(\frac{eV}{kT_S}\frac{\beta}{\beta-1}\right)^2\right]\mathrm{e}^{-\frac{eV}{kT_S}\frac{\beta}{\beta-1}} \\
&\qquad = -\mathrm{e}^{-\frac{eV}{kT_S}}\left\{\beta\left(2+\frac{eV}{kT_S}\right)+\left[2-\beta\left(2+\frac{eV}{kT_S}\right)\right]\mathrm{e}^{-\frac{eV}{kT_S}\frac{1}{\beta-1}}\right\},
\end{aligned}$$

where use has been made of (C.13) and (C.14). The energy flux is thus:

$$\begin{aligned}
Q &= -kT_S N_S \sqrt{\frac{kT_S}{2\pi m_e}}\,\mathrm{e}^{\frac{eV}{kT_S}} \iint_{S_{xy}} x^2 \mathrm{e}^{-x} dx dy \\
&= kT_S N_S \sqrt{\frac{kT_S}{2\pi m_e}}\left\{\beta\left(2+\frac{eV}{kT_S}\right)+\left[2-\beta\left(2+\frac{eV}{kT_S}\right)\right]\mathrm{e}^{-\frac{eV}{kT_S}\frac{1}{\beta-1}}\right\}, \qquad (\mathrm{C}.17)
\end{aligned}$$

and the mean energy,

$$\begin{aligned}
\bar{E} &= \frac{Q}{F_S} = kT_S \frac{\beta\left(2+\frac{eV}{kT_S}\right)+\left[2-\beta\left(2+\frac{eV}{kT_S}\right)\right]\mathrm{e}^{-\frac{eV}{kT_S}\frac{1}{\beta-1}}}{\beta-(\beta-1)\mathrm{e}^{-\frac{eV}{kT_S}\frac{1}{\beta-1}}} \\
&= kT_S \frac{2\left[\beta-(\beta-1)\mathrm{e}^{-\frac{eV}{kT_S}\frac{1}{\beta-1}}\right]+\beta\frac{eV}{kT_S}\left(1-\mathrm{e}^{-\frac{eV}{kT_S}\frac{1}{\beta-1}}\right)}{\beta-(\beta-1)\mathrm{e}^{-\frac{eV}{kT_S}\frac{1}{\beta-1}}} \\
&= 2kT_S + \frac{eV}{1+\frac{1}{\beta}\left(\mathrm{e}^{\frac{eV}{kT_S}\frac{1}{\beta-1}}-1\right)^{-1}}, \qquad (\mathrm{C}.18)
\end{aligned}$$

which corresponds to equation (5.5) and reduces to $2kT_S$ when $V=0$.

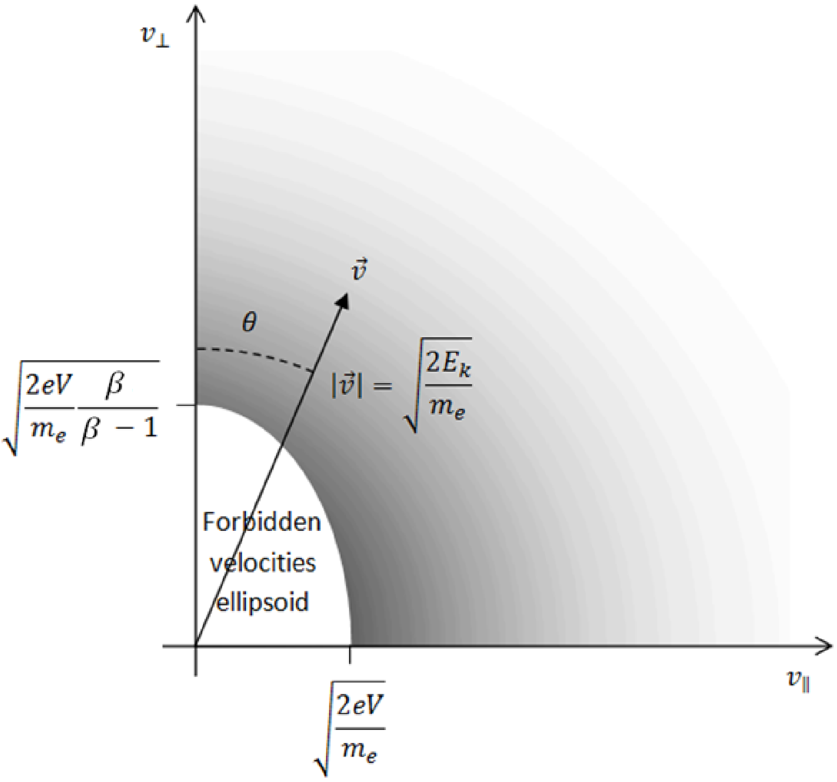

Figure C.1. Representation of the distribution function $d_s(\vec{v})$ corresponding to an accelerated Maxwellian in the velocity space. Strictly speaking, a 3-D space should be considered with rotational symmetry around the $v_\parallel$ axis. Dark grey corresponds to higher electron densities. Note the semi-ellipsoid of forbidden velocities centered on the origin, where $d_s(\vec{v}) = 0$. The domain S_v is the semi-volume $(v_\parallel > 0)$ outside the ellipsoid.

APPENDIX D

Correction of fluxes and mean energy for conductivity purposes:

The corrected values of the flux F_0^{cor}, energy flux Q_{ZP}^{cor}, and mean energy $\bar{E}_{ZP}^{cor}$, of precipitating electrons for a purely (non-accelerated) Maxwellian distribution when the lower limit of integration is E_k^{min} (≅ 0.5 keV [*Robinson et al.,* 1987]) are:

$$F_0^{cor} = \int_{E_k^{min}}^{\infty} f(E_k)dE_k = \int_{E_k^{min}}^{\infty} E_k \mathrm{e}^{\frac{-E_k}{kT_s}} dE_k = F_0 \mathrm{e}^{-2\frac{E_k^{min}}{\bar{E}_{ZP}}} \left(1 + 2\frac{E_k^{min}}{\bar{E}_{ZP}}\right), \quad (\mathrm{D.1})$$

$$\begin{aligned} Q_{ZP}^{cor} &= \int_{E_k^{min}}^{\infty} E_k f(E_k)dE_k = \int_{E_k^{min}}^{\infty} E_k^2 \mathrm{e}^{\frac{-E_k}{kT_s}} dE_k \\ &= Q_{ZP} \mathrm{e}^{-2\frac{E_k^{min}}{\bar{E}_{ZP}}} \left[1 + 2\frac{E_k^{min}}{\bar{E}_{ZP}} + 2\left(\frac{E_k^{min}}{\bar{E}_{ZP}}\right)^2\right], \qquad (\mathrm{D.2}) \end{aligned}$$

$$\bar{E}_{ZP}^{cor} = \frac{Q_{ZP}^{cor}}{F_0^{cor}} = \bar{E}_{ZP} \left[1 + \frac{\left(\frac{E_k^{min}}{\bar{E}_{ZP}}\right)^2}{\frac{1}{2} + \frac{E_k^{min}}{\bar{E}_{ZP}}}\right], \qquad (\mathrm{D.3})$$

where, as defined in the main text, F_0, Q_{ZP}, and $\bar{E}_{ZP}$ represent the original or uncorrected values. This is equivalent to removing the contribution of a semi-sphere of radius $\sqrt{\frac{2E_k^{min}}{m_e}}$ centered in the origin of the velocity space. Such corrections are small for mean energies $\bar{E}_{ZP}$ above about 2 keV. For accelerated Maxwellian distributions, however, the above quantities remain unchanged with respect to (C.15), (C.17) and (C.18) when $eV \geq E_k^{min}$, and the corrections are proportionally less than those applied to (D.1), (D.2) and (D.3) when $eV < E_k^{min}$. This is immediately seen if we consider that in the first case the mentioned semi-sphere lays completely within the semi-ellipsoid (C.10) in the velocity space (see Figure C.1), whereas in the latter case the space to be removed is simply the one existing between the inner semi-ellipsoid and the outer semi-sphere.

APPENDIX E

World map of geomagnetic observatories used for validation purposes:

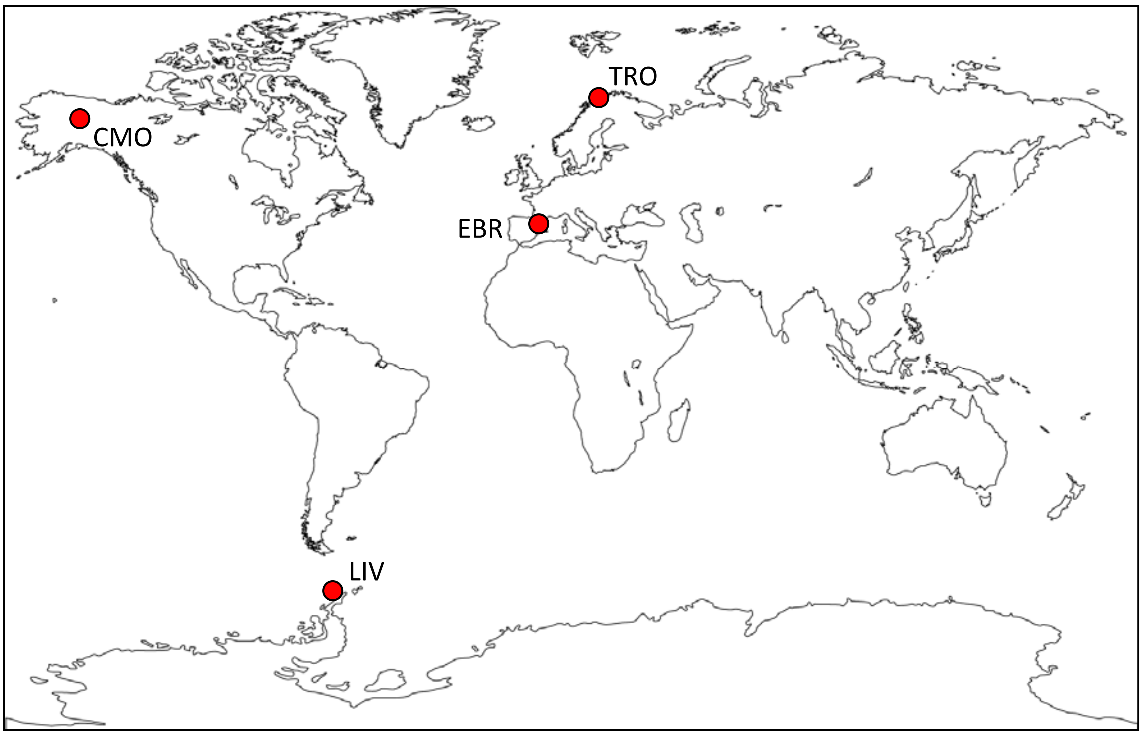

Figure E.1. World map showing the location of the four geomagnetic observatories used in this work to validate the model.

REFERENCES

Anderson, B. J., H. Korth, C. L. Waters, D. L. Green, and P. Stauning (2008), Statistical Birkeland current distributions from magnetic field observations by the Iridium constellation, *Annales Geophys.*, *26*, 671-687, doi:10.5194/angeo-26-671-2008.

Araki, T. (1977), Global structure of geomagnetic sudden commencements, *Planet. Space Sci., 25,* 73–384, doi:10.1016/0032-0633(77)90053-8.

Atkinson, G. (1967), An approximate flow equation for geomagnetic flux tubes and its application to polar substorms, *J. Geophys. Res., 72,* 5373-5382, doi:10.1029/JZ072i021p05373.

Axford, W. I., and Hines, C. O. (1961), A unifying theory of high-latitude geophysical phenomena and geomagnetic storms, *Canadian Journal of Physics, 39*, 1433. doi:10.1139/p61-172.

Baker, K. B., and S. Wing (1989), A new magnetic coordinate system for conjugate studies at high latitudes, *J. Geophys. Res.*, *94*(A7), 9139–9143, doi:10.1029/JA094iA07p09139.

Birkeland, K. (1908), *The Norwegian Aurora Polaris Expedition, 1902-1903,* Vol. 1, H. Aschehoug & Co., Christiania, Norway.

Blanch, E., S. Marsal, A. Segarra, J. M. Torta, D. Altadill, and J. J. Curto (2013), Space weather effects on Earth's environment associated to the 24–25 October 2011 geomagnetic storm, *Space Weather, 11*, 153–168, doi:10.1002/swe.20035.

Blomberg, L. G., and G. T. Marklund (1988), The influence of conductivities consistent with field-aligned currents on high-latitude convection patterns, *J. Geophys. Res.*, *93*, 14493, doi:10.1029/JA093iA12p14493.

Blomberg, L. G., and G. T. Marklund (1991), A numerical model of ionospheric convection derived from field-aligned currents and the corresponding conductivity, *Rep. TRITA-EPP-91-03*, Royal Inst. of Technol, Sweden.

Campbell, W. H. (2001), *Earth Magnetism: A Guided Tour through Magnetic Fields,* Complementary Science Series, Harcourt/Academic Press, San Diego, CA.

Cattell, C., J. Dombeck, W. Yusof, C. Carlson, and J. McFadden (2004), FAST observations of the solar illumination dependence of upflowing electron beams in the auroral zone, *J. Geophys. Res.*, *109*, A02209, doi:10.1029/2003JA010075.

Chaston, C. C., J. W. Bonnell, C. W. Carlson, J. P. McFadden, R. E. Ergun, and R. J. Strangeway (2003), Properties of small-scale Alfvén waves and accelerated electrons from FAST, *J. Geophys. Res.*, *108*, 8003, doi:10.1029/2002JA009420*, A4.*

Clauer, C. R., and Y. Kamide (1985), DP 1 and DP 2 current systems for the March 22, 1979 substorms, *J. Geophys. Res., 90,* 1343-1354, doi:10.1029/JA090iA02p01343.

Clausen, L. B. N., J. B. H. Baker, J. M. Ruohoniemi, S. E. Milan, and B. J. Anderson (2012), Dynamics of the region 1 Birkeland current oval derived from the Active Magnetosphere and Planetary Electrodynamics Response Experiment (AMPERE), *J. Geophys. Res.*, *117*, A06233, doi:10.1029/2012JA017666.

Cnossen, I. (2014), The importance of geomagnetic field changes versus rising CO_2 levels for long-term change in the upper atmosphere, *J. Space Weather Space Clim., 4*, A18, doi:http://dx.doi.org/10.1051/swsc/2014016.

Connors, M., R. L. McPherron, B. J. Anderson, H. Korth, C. T. Russell, and X. Chu (2014), Electric currents of a substorm current wedge on 24 February 2010, *Geophys. Res. Lett.*, *41*, doi:10.1002/2014GL060604.

Cornélissen, G., F. Halberg, T. Breus, E. V. Syutkina, R. Baevsky, A. Weydahl, Y. Watanabe, K. Otsuka, J. Siegelová, B. Fiser, and E. E. Bakken (2002), Non-photic solar associations of heart rate variability and myocardial infarction, *J. Atmos. Solar-Terr. Phys., 64,* 707–720, doi:10.1016/S1364-6826(02)00032-9.

Cousins, E. D. P., T. Matsuo, and A. D. Richmond (2013), SuperDARN assimilative mapping*, J. Geophys. Res. Space Physics, 118,* 7954–7962, doi:10.1002/2013JA019321.

Cowley, S. W. H. (2000), Ionosphere-magnetosphere interactions: A tutorial review, in *Magnetospheric Current Systems*, edited by S. Ohtani, R. Fujii, M. Hesse, and R. L. Lysak, Geophys. Monogr. Ser., vol. 118, 91-106, American Geophysical Union, Washington D. C., doi:10.1029/GM118.

Cummings, W. D., and A. J. Dessler (1967), Field-aligned currents in the magnetosphere, *J. Geophys. Res.*, *72*(3), 1007–1013, doi:10.1029/JZ072i003p01007.

Daglis, I. A. (2004), *Effects of Space Weather on Technology Infrastructure,* vol. 176 NATO Science Series II, Kluwer Academic Publishers, Dordrecht, The Netherlands.

Doumbia, V., A. Maute, and A. D. Richmond (2007), Simulation of equatorial electrojet magnetic effects with the Thermosphere-Ionosphere-Electrodynamics General Circulation Model, *J. Geophys. Res., 112*(A09309), doi:10.1029/2007JA012308.

Dungey, J. W. (1961), Interplanetary magnetic fields and the auroral zones, *Phys. Rev. Let., 6*(1), 47-49, doi:10.1103/PhysRevLett.6.47.

Emery, B. A., et al. (1996), Assimilative mapping of ionospheric electrodynamics in the thermosphere-ionosphere general circulation model, comparisons with global ionospheric and thermospheric observations during the GEM/SUNDIAL period of March 28–29, 1992, *J. Geophys. Res.*, *101*(A12), 26681–26696, doi:10.1029/96JA01285.

Emery, B. A., R. G. Roble, E. C. Ridley, A. D. Richmond, D. J. Knipp, G. Crowley, D. S. Evans, F. J. Rich, and S. Maeda (2012), Parameterization of the ion convection and the auroral oval in the NCAR thermospheric general circulation models, NCAR Tech. Note NCAR/TN-491+STR, ISSN Electronic Edition 2153-2400, http://nldr.library.ucar.edu/repository/collections/TECH-NOTE-000-000-000-856.

Fang, T. W., A. D. Richmond, J. Y. Liu, A. Maute, C. H. Lin, C. H. Chen, and B. Harper (2008), Model simulation of the equatorial electrojet in the Peruvian and Philippine sectors, *J. Atmos. Sol. Terr. Phys., 70*(17), 2203-2211, doi:10.1016/j.jastp.2008.04.021.

Fathy, I., C. Amory-Mazaudier, A. Fathy, A. M. Mahrous, K. Yumoto, and E. Ghamry (2014), Ionospheric disturbance dynamo associated to a coronal hole: Case study 5-10 April 2010, *J. Geophys. Res. Space Physics, 119,* 4120–4133, doi:10.1002/2013JAO19510.

Feigin, V. L., Parmar, P. G., Barker-Collo, S., Bennett, D. A., Anderson, C. S., Thrift, A. G., Stegmayr, B., Rothwell, P. M., Giroud, M., Bejot, Y., Carvil, P., Krishnamurthi, R., Kasabov, N. (2014), Geomagnetic storms can trigger stroke: Evidence from 6 large population-based studies in Europe and Australasia, *Stroke*, 45, 1639-1645, doi:10.1161/STROKEAHA.113.004577.

Finlay, C. C. et al. (2010), International Geomagnetic Reference Field: the eleventh generation. *Geophysical Journal International*, *183*, 1216–1230. doi: 10.1111/j.1365-246X.2010.04804.x.

Fridman, M., and J. Lemaire (1980), Relationship between auroral electrons fluxes and field aligned electric potential difference, *J. Geophys. Res., 85*(A2), 664–670*,* doi*:*10.1029/JA085iA02p00664.

Fukushima, N. (1969), Equivalence in ground geomagnetic effect of Chapman-Vestine's and Birkeland-Alfven's current systems for polar magnetic storms, *Rep. Ionos. Space Res. Jap., 23*, 219-227.

Fukushima, N. (1976), Generalized theorem for no ground magnetic effect of vertical currents connected with Pedersen currents in the uniform-conductivity ionosphere, *Rep. Ionos. Space Res. Jap., 30*, 35-50.

Fuller-Rowell, T. J., D. Rees (1980), A three-dimensional time-dependent global model of the thermosphere, *J. Atmos. Sci.*, *37,* 2545–2567, doi:10.1175/1520-0469(1980)037.

Galand, M., and A. D. Richmond (2001), Ionospheric electrical conductances produced by auroral proton precipitation, *J. Geophys. Res.*, *106*(A1), 117-125, doi:10.1029/1999JA002001.

Gallet, Y., A. Genevey, F. Fluteau (2005), Does Earth's magnetic field secular variation control centennial climate change? *Earth Planet. Sci. Lett., 236,* 339-347, doi:10.1016/j.epsl.2005.04.045.

Gurnett, D. A. (1972), in *Critical Problems of Magnetospheric Physics*, edited by E. R. Dyer (National Academy of Sciences), p. 123, Washington D. C.

Hagan, M. E., and J. M. Forbes (2002), Migrating and nonmigrating diurnal tides in the middle and upper atmosphere excited by tropospheric latent heat release, *J. Geophys. Res.*, *107*(D24), 4754, doi:10.1029/2001JD001236.

Hagan, M. E., and J. M. Forbes (2003), Migrating and nonmigrating semidiurnal tides in the upper atmosphere excited by tropospheric latent heat release, *J. Geophys. Res.*, *108*(A2), 1062, doi:10.1029/2002JA009466.

Hapgood, M. (2012), Astrophysics: Prepare for the coming space weather storm, *Nature*, *484*, 311-313, doi:10.1038/484311a.

Harel, M., R. A. Wolf, R. W. Spiro, P. H. Reiff, C.-K. Chen, W. J. Burke, F. J. Rich, and M. Smiddy (1981), Quantitative simulation of a magnetospheric substorm 2.

Comparison with observations, *J. Geophys. Res.*, *86*(A4), 2242–2260, doi:10.1029/JA086iA04p02242.

Hargreaves, J. K. (1992), *The Solar-Terrestrial Environment: an Introduction to Geospace - the Science of the Terrestrial Upper Atmosphere, Ionosphere and Magnetosphere*, Cambridge Atmospheric and Space Science Series 7, Cambridge University Press, UK.

Heelis, R. A., J. K. Lowell, and R. W. Spiro (1982), A model of the high-latitude ionospheric convection pattern, *J. Geophys. Res.*, *87*(A8), 6339–6345, doi:10.1029/JA087iA08p06339.

Heelis, R. A., P. H. Reiff, J. D. Winningham, and W. B. Hanson (1986), Ionospheric convection signatures observed by DE-2 during northward interplanetary magnetic field, *J. Geophys. Res.*, *91*(A5), 5817–5830, doi:10.1029/JA091iA05p05817.

Heppner, J. P. (1972), Polar cap electric field distributions related to the interplanetary magnetic field direction, *J. Geophys. Res.,* *77*(25), 4877–4887, doi:10.1029/JA077i025p04877.

Heppner, J. P., and N. C. Maynard (1987), Empirical high-latitude electric field models, *J. Geophys. Res.*, *92*(A5), 4467–4489, doi:10.1029/JA092iA05p04467.

Iijima, T., and T. A. Potemra (1976), The amplitude distribution of field-aligned currents at northern high latitudes observed by Triad, *J. Geophys. Res.*, *81*(13), 2165–2174, doi:10.1029/JA081i013p02165.

Jankowski, J., and C. Sucksdorff (1996), *IAGA Guide for Magnetic Measurements and Observatory Practice,* International Association of Geomagnetism and Aeronomy, Warsaw, Poland.

Jin, H., Y. Miyoshi, H. Fujiwara, H. Shinagawa, K. Terada, N. Terada, M. Ishii, Y. Otsuka, and A. Saito (2011), Vertical connection from the tropospheric activities to the ionospheric longitudinal structure simulated by a new Earth's whole atmosphere-ionosphere coupled model, *J. Geophys. Res., 116* (A01316), doi:10.1029/2010JA015925.

Kamide, Y. (1978), On current continuity at the Harang discontinuity, *Planet. Space. Sci.*, *26*, 237-244, doi:10.1016/0032-0633(78)90089-2.

Kamide, Y. (1988), *Electrodynamic processes in the Earth's ionosphere and magnetosphere*, Kyoto Sangyo University Press, Kyoto, Japan.

Kamide, Y., and S. Matsushita (1979a), Simulation studies of ionospheric electric fields and currents in relation to field-aligned currents, 1, quiet periods, *J. Geophys. Res., 84*(A8), 4083–4098, doi:10.1029/JA084iA08p04083.

Kamide, Y., and S. Matsushita (1979b), Simulation studies of ionospheric electric fields and currents in relation to field-aligned currents, 2, substorms, *J. Geophys. Res.*, *84*(A8), 4099–4115, doi:10.1029/JA084iA08p04099.

Kamide, Y., A. D. Richmond, and S. Matsushita (1981), Estimation of ionospheric electric fields, ionospheric currents, and field-aligned currents from ground magnetic records, *J. Geophys. Res.*, *86*(A2), 801–813, doi:10.1029/JA086iA02p00801.

Kappenman, J. G., L. J. Zanetti, and W. A. Radasky (1997), Geomagnetic storms can threaten electric power grid, *Earth in Space*, *9*(7), 9−11.

Kelley, M. C. (2009), *The Earth's Ionosphere: Plasma Physics and Electrodynamics*, Academic Press, San Diego, CA.

Kikuchi, T., H. Lühr, K. Schlegel, H. Tachihara, M. Shinohara, and T.-I. Kitamura (2000), Penetration of auroral electric fields to the equator during a substorm*, J. Geophys. Res.*, *105(A10)*, 23251–23261, doi:10.1029/2000JA900016.

Klimenko, M., V. Klimenko, and V. Bryukhanov (2006), Numerical simulation of the electric field and zonal current in the Earth's ionosphere: The dynamo field and equatorial electrojet, *J. Geomag. Aeron.,* *46*(4), 457–466, doi:10.1134/S0016793206040074.

Knight, S. (1973), Parallel electric fields, *Planet. Space Sci., 21*, 5, 741–750, doi:10.1016/0032-0633(73)90093-7.

Knipp, D. J., T. Matsuo, L. Kilcommons, A. Richmond, B. Anderson, H. Korth, R. Redmon, B. Mero, and N. Parrish (2014), Comparison of magnetic perturbation data from LEO satellite constellations: Statistics of DMSP and AMPERE*, Space Weather*, *12,* 2–23, doi:10.1002/2013SW000987.

Kobea, A. T., A. D. Richmond, B. A. Emery, C. Peymirat, H. Lühr, T. Moretto, M. Hairston, and C. Amory-Mazaudier (2000), Electrodynamic coupling of high and low latitudes: Observations on May 27, 1993, *J. Geophys. Res.*, *105(A10),* 22979–22989, doi:10.1029/2000JA000058.

Korth, H., B. J. Anderson, and C. L. Waters (2010a), Statistical analysis of the dependence of large-scale Birkeland currents on solar wind parameters, *Annales Geophys.*, *28*, 515-530, doi:10.5194/angeo-28-515-2010.

Korth, H., L. Dyrud, B. J. Anderson, C. L. Waters, and R. J. Barnes (2010b), AMPERE science data reduction and processing, paper presented at AGU Fall Meeting 2010, 2010AGUFMSM11A1692K.

Korth, H., Y. Zhang, B. J. Anderson, T. Sotirelis, and C. L. Waters (2014), Statistical relationship between large-scale upward field-aligned currents and electron precipitation*, J. Geophys. Res. Space Physics*, *119*, 6715–6731, doi:10.1002/2014JA019961.

Koskinen, H., E. Tanskanen, R. Pirjola, A. Pulkkinen, C. Dyer, D. Rodgers, P. Cannon, J. C. Mandeville, and D. Boscher (2001), Space weather effects catalogue, in *ESA Space Weather Studies*, FMI, Finland.

Kuvshinov, A., and H. Utada (2010), Anomaly of the geomagnetic Sq variation in Japan: Effect from 3-D subterranean structure or the ocean effect?, *Geophys. J. Int., 183*, 1239–1247, doi:10.1111/j.1365-246X.2010.04809.x.

Lauridsen, K. E. (1985), Experiences with the DI-fluxgate magnetometer inclusive theory of the instrument and comparison with other methods, *Danish Meteorological Institute Geophysical Papers, R-71,* Denmark.

Le, G., J. A. Slavin, and R. J. Strangeway (2010), Space Technology 5 observations of the imbalance of regions 1 and 2 field-aligned currents and its implication to the cross-polar cap Pedersen currents, *J. Geophys. Res., 115,* A07202, doi:10.1029/2009JA014979.

Legrand J. P., M. Le Goff, and C. Mazaudier (1990), On the climatic changes and the sunspot activity during the XVIIth century, *Annales Geophys., 8(10),* 637-644.

Lu, G., X. Pi, A. D. Richmond, R. G. Roble (1998), Variations of total electron content during geomagnetic disturbances: A model/observation comparison, *Geophys. Res. Lett., 25*(3), 253-256, doi:10.1029/98GL02387.

Lu, G., A. D. Richmond, J. M. Ruohoniemi, R. A. Greenwald, M. Hairston, F. J. Rich, and D. S. Evans (2001), An investigation of the influence of data and model inputs on Assimilative Mapping of Ionospheric Electrodynamics, *J. Geophys. Res., 106*(A11), 417-433, doi:10.1029/2001JA000003.

Lühr, H., M. Korte and M. Mandea (2009), The recent geomagnetic field and its variations, in *Geomagnetic Field Variations, Advances in Geophysical and Environmental Mechanics and Mathematics,* edited by K.-H. Glassmeier, H. Soffel, and J. Negendank, Springer-Verlag, 25-63, Berlin-Heidelberg, Germany.

Macmillan, S. (2007), Observatories, Overview, in *Encyclopedia of Geomagnetism and Paleomagnetism*, edited by D. Gubbins, and E. Herrero-Bervera, *Encyclopedia of Earth Sciences Series*, 708-711, Springer, Dordrecht, The Netherlands.

Marklund, G. T., L. G. Blomberg, T. A. Potemra, J. S. Murphree, F. J. Rich, and K. Stasiewicz (1987), A new method to derive “instantaneous” high-latitude potential distributions from satellite measurements including auroral imager data, *Geophys. Res. Lett.*, *14*, 439, doi:10.1029/GL014i004p00439.

Marklund, G. T., L. G. Blomberg, K. Stasiewicz, J. S. Murphree, R. Pottelette, L. J. Zanetti, T. A. Potemra, D. A. Hardy, and F. J. Rich (1988), Snapshots of high-latitude electrodynamics using Viking and DMSP F7 observations, *J. Geophys. Res*, *93*(A12), 14479–14492, doi:10.1029/JA093iA12p14479.

Marsal, S., and J. M. Torta (2007), An evaluation of the uncertainty associated with the measurement of the geomagnetic field with a D/I fluxgate theodolite, *Meas. Sci. Technol.*, *18*(7), 2143, doi:10.1088/0957-0233/18/7/046.

Marsal, S., A. D. Richmond, A. Maute, and B. J. Anderson (2012), Forcing the TIEGCM model with Birkeland currents from the Active Magnetosphere and Planetary Electrodynamics Response Experiment, *J. Geophys. Res.*, *117*, A06308, doi:10.1029/2011JA017416.

Maus, S., C. Manoj, J. Rauberg, I. Michaelis, and H. Lühr (2010), NOAA/NGDC candidate models for the 11th generation International Geomagnetic Reference Field and the concurrent release of the 6th generation POMME magnetic model, *Earth Planets and Space*, *62*(10), 729-735, doi:10.5047/eps.2010.07.006.

McPherron, R. L. (1972), Substorm related changes in the geomagnetic tail: the growth phase, *Planet. Space Sci.*, *20*, 1521, doi:10.1016/0032-0633(72)90054-2.

McPherron, R. L., C. T. Russell, and M. Aubry (1973), Satellite studies of magnetospheric substorms on August 15, 1978: 9. Phenomenological model for substorms, *J. Geophys. Res., 78,* 3131-3149*,* doi:10.1029/JA078i016p03131.

Merkin, V. G., and J. G. Lyon (2010), Effects of the low-latitude ionospheric boundary condition on the global magnetosphere, *J. Geophys. Res.*, *115*, A10202, doi:10.1029/2010JA015461.

Merkin, V. G., B. J. Anderson, J. G. Lyon, H. Korth, M. Wiltberger, and T. Motoba (2013), Global evolution of Birkeland currents on 10 min timescales: MHD simulations and observations, *J. Geophys. Res. Space Physics*, *118*, 4977–4997, doi:10.1002/jgra.50466*.*

Millward, G. H., I. C. F. Müller-Wodarg, A. D. Aylward, T. J. Fuller-Rowell, A. D. Richmond, and R. J. Moffett (2001), An investigation into the influence of tidal forcing on F region equatorial vertical ion drift using a global ionosphere-thermosphere model with coupled electrodynamics, *J. Geophys. Res.*, *106*(A11), 24733–24744, doi:10.1029/2000JA000342*.*

Mishin, V. M., S. B. Lunyushkin, D. Sh. Shirapov, and W. Baumjohann (1986), A new method for generating instantaneous ionospheric conductivity models using ground-based magnetic data, *Planet. Space Sci.*, *34*, 713, doi:10.1016/0032-0633(86)90125-X.

Murphy, K. R., I. R. Mann, I. J. Rae, C. L. Waters, B. J. Anderson, D. K. Milling, H. J. Singer, and H. Korth (2012), Reduction in field-aligned currents preceding and local to auroral substorm onset, *Geophys. Res. Lett., 39*, L15106, doi:10.1029/2012GL052798.

Namgaladze, A. A., Yu. N. Korenkov, V. V. Klimenko, I. V. Karpov, F. S. Bessarab, V. A. Surotkin, T. A. Glushchenko, and N. M. Naumova (1990), A global numerical model of the thermosphere, ionosphere, and protonosphere of the earth, Geomag. Aeron., 30, 515-521 (Engl. Trans.).

Newell, P. T., C. I. Meng, and K. M. Lyons (1996), Suppression of discrete aurora by sunlight, *Nature, 381*, 766-767, doi:10.1038/381766a0.

Newell, P. T., T. Sotirelis, and S. Wing (2009), Diffuse, monoenergetic, and broadband aurora: The global precipitation budget, *J. Geophys. Res., 114*, A09207, doi:10.1029/2009JA014326.

Nguyen, V., and S. E. Palo (2014), Transmission of planetary effect events to the upper atmosphere through eddy diffusion modulation, *J. Atmos. Sol.-Terr. Phys., 117*, 1-6, doi:10.1016/j.jastp.2014.04.008.

Ni, B., R. M. Thorne, R. B. Horne, N. P. Meredith, Y. Y. Shprits, L. J. Chen, and W. Li (2011a), Resonant scattering of plasma sheet electrons leading to diffuse auroral precipitation: 1. Evaluation for electrostatic electron cyclotron harmonic waves*, J. Geophys. Res.*, *116*, A04218, doi:10.1029/2010JA016232.

Ni, B., R. M. Thorne, N. P. Meredith, R. B. Horne, and Y. Y. Shprits (2011b), Resonant scattering of plasma sheet electrons leading to diffuse auroral precipitation: 2. Evaluation for whistler mode chorus waves*, J. Geophys. Res.*, *116*, A04219, doi:10.1029/2010JA016233.

Nishida, A., N. Iwasaki, and T. Nagata (1966), The origin of fluctuations in the equatorial electrojet; A new type of geomagnetic variation, *Annales Geophys., 22*, 478-484.

Nosé, M., T. Iyemori, L. Wang, A. Hitchman, J. Matzka, M. Feller, S. Egdorf, S. Gilder, N. Kumasaka, K. Koga, H. Matsumoto, H. Koshiishi, G. Cifuentes-Nava, J. J. Curto, A. Segarra, and C. Çelik (2012), Wp index: A new substorm index derived from high-resolution geomagnetic field data at low latitude, *Space Weather*, *10*, S08002, doi:10.1029/2012SW000785.

Olsen, N. (1996), Magnetospheric contributions to geomagnetic daily variations, *Annales Geophys.*, *14*, 538-544, doi:10.1007/s00585-996-0538-0.

Olsen, N. (1997), Geomagnetic tides and related phenomena, in *Tidal Phenomena*, edited by W. H. Zuern, and H. G. Wenzel, *Lecture Notes in Earth Sciences,* vol. 66, 261-274, Springer, Berlin, Germany, doi:10.1007/BFb0011466.

Papailiou, M., H. Mavromichalaki, K. Kudela, J. Stetiarova, and S. Dimitrova (2011), Effect of geomagnetic disturbances on physiological parameters: an investigation on aviators, *Adv. Space Res.*, *48*, 1545–1550, doi:10.1016/j.asr.2011.07.004.

Parkinson, W. D (1983), *Introduction to Geomagnetism*, Scottish Academic Press, Edinburgh, UK.

Pembroke, A., F. Toffoletto, S. Sazykin, M. Wiltberger, J. Lyon, V. Merkin, and P. Schmitt (2012), Initial results from a dynamic coupled magnetosphere-ionosphere-ring current model, *J. Geophys. Res., 117*(A02211), doi:10.1029/2011JA016979.

Peymirat, C., A. D. Richmond, B. A. Emery, and R. G. Roble (1998), A magnetosphere-thermosphere-ionosphere electrodynamics general circulation model, *J. Geophys. Res.*, *103*(A8), 17467–17477, doi:10.1029/98JA01235.

Phillips, N. (1956), The general circulation of the atmosphere: A numerical experiment. *Q. J. R. Meteorol. Soc., 82*, 123–164, doi: 10.1002/qj.49708235202.

Prölss, G. W. (2004), *Physics of the Earth's Space Environment. An Introduction*, Springer, Berlin, Germany.

Ptitsyna, N. G., V. V. Kasinskii, G. Villoresi, N. N. Lyahov, L. I. Dorman, and N. Iucci (2008), Geomagnetic effects on mid-latitude railways: a statistical study of anomalies in the operation of signaling and train control equipment on the East-Siberian Railway, *Adv. Space Res.*, *42*(9), 1510-1514, doi:10.1016/j.asr.2007.10.015.

Pulkkinen, A., M. Hesse, M. Kuznetsova, and L. Rastätter (2007), First-principles modeling of geomagnetically induced electromagnetic fields and currents from upstream solar wind to the surface of the Earth, *Annales Geophys., 25*, 881–893, doi:10.5194/angeo-25-881-2007.

Pulkkinen, A., et al. (2011), Geospace environment modeling 2008-2009 challenge: Ground magnetic field Perturbations, *Space Weather, 9*, S02004, doi:10.1029/2010SW000600.

Qian, L., A. G. Burns, B. Emery, B. Foster, G. Lu, A. Maute, A. D. Richmond, R. G. Roble, S. C. Solomon, and W. Wang (2014), The NCAR TIE-GCM: A community model of the coupled thermosphere/ionosphere system, in *Modeling the Ionosphere-Thermosphere System*, Geophys. Monogr. Ser., vol. 201, edited by J. Huba, R. Schunk, and G. Khazanov, 73-84, American Geophysical Union, Washington D. C.

Raeder, J., Y. Wang, and T. J. Fuller-Rowell (2001a), Geomagnetic storm simulation with a coupled magnetosphere-ionosphere-thermosphere model, in *Space Weather,* Geophys. Monogr. Ser., vol. 125, edited by P. Song, H. J. Singer, and G. L. Siscoe, 377-384, American Geophysical Union, Washington D. C., doi:10.1029/GM125p0377.

Raeder, J., R. L. McPherron, L. A. Frank, S. Kokubun, G. Lu, T. Mukai, W. R. Paterson, J. B. Sigwarth, H. J. Singer, and J. A. Slavin (2001b), Global simulation of the geospace environment modeling substorm challenge event, *J. Geophys. Res., 106*, 381-395, doi:10.1029/2000JA000605.

Rasson, J. L. (2007), Observatories, Instrumentation, in *Encyclopedia of Geomagnetism and Paleomagnetism*, edited by D. Gubbins, and E. Herrero-Bervera, *Encyclopedia of Earth Sciences Series*, 711-713, Springer, Dordrecht, The Netherlands.

Rees, M. H. (1963), Auroral ionization and excitation by incident energetic electrons, *Planet. Space Sci., 11*, 10, 1209-1218, doi:10.1016/0032-0633(63)90252-6.

Reitz, J. R., F. J. Milford, and R. W. Christy (2008), *Foundations of Electromagnetic Theory*, 4th edition, Addison-Wesley Pub. Co., Reading, MA.

Ren, Z., W. Wan, and L. Liu (2009), ITEM-IGGCAS: A new global coupled ionosphere thermosphere-electrodynamics model, *J. Atmos. Sol.-Terr. Phys., 71*, 2064–2076, doi:10.1016/j.jastp.2009.09.015.

Rich, F. J., M. S. Gussenhoven, and M. E. Greenspan (1987), Using simultaneous particle and field observations on a low altitude satellite to estimate Joule heat energy flow into the high latitude ionosphere, *Annales Geophys., 5A*(6), 527-534.

Richmond, A. D. (1974), The computation of magnetic effects of field-aligned magnetospheric currents, *J. Atmos. Terr. Phys.*, *36*, 245-252, doi:10.1016/0021-9169(74)90044-0.

Richmond, A. D. (1992), Assimilative Mapping of Ionospheric Electrodynamics, *Adv. Space Res.*, *12*(6), 59-68. doi:10.1016/0273-1177(92)90040-5.

Richmond, A. D. (1995a), Ionospheric electrodynamics, in *Handbook of atmospheric electrodynamics*, vol. II, edited by H. Volland, 249-290, CRC Press, Boca Raton, FL.

Richmond, A. D. (1995b), Ionospheric electrodynamics using magnetic apex coordinates, *J. Geomag. Geoelectr.*, *47*, 191-212.

Richmond, A. D. (1996), Space weather research prompts study of ionosphere and upper atmospheric electrodynamics, *Eos Trans., AGU*, *77*(11), 101, doi:10.1029/96EO00066.

Richmond, A. D., and W. Baumjohann (1984), Three-dimensional analysis of magnetometer array data, *J. Geophys., 54*, 138-156.

Richmond, A. D., and Y. Kamide (1988), Mapping electrodynamic features of the high-latitude ionosphere from localized observations: Technique, *J. Geophys. Res. 93*, 5741–5759, doi:10.1029/JA093iA06p05741.

Richmond, A. D., and A. Maute (2014), Ionospheric electrodynamics modeling, in *Modeling the Ionosphere-Thermosphere System*, Geophys. Monogr. Ser., vol. 201, edited by J. Huba, R. Schunk, and G. Khazanov, 57-71, American Geophysical Union, Washington D. C, doi:10.1002/9781118704417.ch6.

Richmond, A. D., and J. P. Thayer (2000), Ionospheric electrodynamics: a tutorial, in *Magnetospheric Current Systems*, Geophys. Monogr. Ser., vol. 118, edited by S. Ohtani, R. Fujii, M. Hesse, R. L. Lysak, 131-146, American Geophysical Union, Washington D. C., doi:10.1029/GM118.

Richmond, A. D., E. C. Ridley, and R. G. Roble (1992), A Thermosphere/Ionosphere General Circulation Model with coupled electrodynamics, *Geophys. Res. Lett.*, *19*(6), 601-604, doi:10.1029/92GL00401.

Ridley, A. J., A. D. Richmond, T. I. Gombosi, D. L. De Zeeuw, and C. R. Clauer (2003), Ionospheric control of the magnetospheric configuration: Thermospheric neutral winds, *J. Geophys. Res.*, *108*, 1328, doi:10.1029/2002JA009464*,* A8.

Ripka, P. (2000), New directions in fluxgate sensors, *Journal of Magnetism and Magnetic Materials*, *215-216*, 735-739, doi:10.1016/S0304-8853(00)00273-0.

Ritter, P., H. Lühr, and J. Rauberg (2013), Determining field-aligned currents with the Swarm constellation mission, *Earth Planets and Space*, *65*, 1285-1294, doi:10.5047/eps.2013.09.006.

Robinson, R. M., R. R. Vondrak, K. Miller, T. Dabbs, and D. Hardy (1987), On calculating ionospheric conductances from the flux and energy of precipitating electrons, *J. Geophys. Res., 92*(A3), 2565–2569, doi:10.1029/JA092iA03p02565.

Roble, R. G., and M. H. Rees (1977), Time-dependent studies of the aurora: Effects of particle precipitation on the dynamic morphology of ionospheric and atmospheric properties, *Planetary and Space Science*, *25*, 991-1010, doi:10.1016/0032-0633(77)90146-5.

Roble, R. G., and E. C. Ridley (1987), An auroral model for the NCAR thermospheric general circulation model (TGCM), *Annales Geophys.*, *5A*(6), 369–382.

Roble, R. G., R. E. Dickinson, and E. C. Ridley (1977), Seasonal and solar cycle variations of the zonal mean circulation in the thermosphere, *J. Geophys. Res.*, *82*(35), 5493–5504, doi:10.1029/JA082i035p05493.

Roble, R. G., E. C. Ridley, A. D. Richmond, and R. E. Dickinson (1988), A coupled Thermosphere/Ionosphere General Circulation Model, *Geophys. Res. Lett.*, *15*(12), 1325–1328, doi:10.1029/GL015i012p01325.

Rokityansky, I. I. (1982), *Geoelectromagnetic Investigation of the Earth's Crust and Mantle*, Springer, Berlin, Germany, doi:10.1007/978-3-642-61801-7.

Sabaka, T. J., N. Olsen, and M. Purucker (2004), Extending comprehensive models of the Earth's magnetic field with Oersted and CHAMP data, *Geophys. J. Int.*, *159*, 521-547, doi:10.1111/j.1365-246X.2004.02421.x.

Schuster, A. (1889), The Diurnal Variations of Terrestrial Magnetism, in *Philosophical Transactions of the Royal Society of London*, Series A, 180, 467-518.

Serebriakov, B. E. (1982), Investigation of processes in the thermosphere during magnetic disturbances, *Geomag. i Aeron.*, *22*, 776-781.

Shao, X., P. N. Guzdar, G. M. Milikh, K. Papadopoulos, C. C. Goodrich, A. Sharma, M. J. Wiltberger, and J. G. Lyon (2002), Comparing ground magnetic field perturbations from global MHD simulations with magnetometer data for the 10 January 1997 magnetic storm event, *J. Geophys. Res., 107*(A8), 1177, doi:10.1029/2000JA000445.

Shiokawa, K., G. Lu, Y. Otsuka, T. Ogawa, M. Yamamoto, N. Nishitani, and N. Sato (2007), Ground observation and AMIE-TIEGCM modeling of a storm-time traveling ionospheric disturbance, *J. Geophys. Res.*, *112*, A05308, doi:10.1029/2006JA011772.

Siscoe, G. L., G. M. Erickson, B. U. Ö. Sonnerup, N. C. Maynard, K. D. Siebert, D. R. Weimer, and W. W. White (2001), Global role of E|| in magnetopause reconnection: An explicit demonstration, *J. Geophys. Res., 106*(A7), 13,015–13,022, doi:10.1029/2000JA000062.

Smagorinsky, J. (1963), General circulation experiments with the primitive equations, *Mon. Wea. Rev., 91*, 3, 99-164, doi:10.1175/1520-0493(1963)091.

Solomon S. C., and L. Qian (2005), Solar extreme-ultraviolet irradiance for general circulation models*, J. Geophys. Res., 110,* A10306, doi:10.1029/2005JA011160.

Stewart, B. (1883), Hypothetical views concerning the connexion between the state of the Sun and terrestrial magnetism, in *Encyclopedia Britannica*, Edinburgh, 16, 181-184.

Strangeway, R. J., R. C. Elphic, W. J. Peria, and C. W. Carlson (2000), FAST observations of electromagnetic stress applied to the polar ionoshere, in *Magnetospheric Current Systems*, Geophys. Monogr. Ser., vol. 118, edited by S. Ohtani, R. Fujii, M. Hesse, R. L. Lysak, 131-146, American Geophysical Union, Washington D. C., doi:10.1029/GM118.

Svensmark, H., and N. Calder (2007), *The Chilling Stars: A New Theory of Climate Change,* Icon Books, Cambridge, UK.

Torta, J. M., S. Marsal, and M. Quintana (2014), Assessing the hazard from geomagnetically induced currents to the entire high-voltage power network in Spain, *Earth Planets and Space*, *66*: 87, doi:10.1186/1880-5981-66-87.

Tsyganenko, N. A. (2014), Data-based modeling of the geomagnetosphere with an IMF-dependent magnetopause, *J. Geophys. Res. Space Physics*, *119*, 335–354, doi:10.1002/2013JA019346.

van Sabben, D. (1966), Magnetospheric currents, associated with the N-S asymmetry of Sq, *J. Atmos. Terr. Phys., 28*, 965-981.

Vázquez, M. (1998), *La Historia del Sol y el Cambio Climático,* McGraw Hill Interamericana de España, Madrid, Spain.

Vickrey, J. F., R. R. Vondrak, and S. J. Matthews (1981), The diurnal and latitudinal variations of auroral zone ionospheric conductivity, *J. Geophys. Res.*, *86*(A1), 65-75, doi:10.1029/JA086iA01p00065.

Vondrak, R., and R. Robinson (1985), Inference of high-latitude ionization and conductivity from AE-C measurements of auroral electron fluxes, *J. Geophys. Res.*, *90*(A8), 7505-7512, doi:10.1029/JA090iA08p07505.

Waters, C. L., B. J. Anderson, and K. Liou (2001), Estimation of global field aligned currents using the Iridium System magnetometer data, *Geophys. Res. Lett., 28*, 2165-2168, doi:10.1029/2000GL012725.

Wang, W., M. Wiltberger, A. G. Burns, S. Solomon, T. L. Killeen, N. Maruyama, and J. Lyon (2004), Initial results from the CISM coupled magnetosphere-ionosphere-thermosphere (CMIT) model: Thermosphere ionosphere responses, *J. Atmos. Sol.-Terr. Phys.*, *66*, 1425-1442, doi:10.1016/j.jastp.2004.04.008.

Weimer, D. R. (2005), Improved ionospheric electrodynamic models and application to calculating Joule heating rates, *J. Geophy. Res.*, *110*(A05306), doi:10.1029/2004JA010884.

Weimer, D. R., C. R. Clauer, M. J. Engebretson, T. L. Hansen, H. Gleisner, I. Mann, and K. Yumoto (2010), Statistical maps of geomagnetic perturbations as a function of the interplanetary magnetic field, *J. Geophys. Res., 115*(A10320), doi:10.1029/2010JA015540.

Wilder, F. D., G. Crowley, B. J. Anderson, and A. D. Richmond (2012), Intense dayside Joule heating during the April 5, 2010 geomagnetic storm recovery phase observed by AMIE and AMPERE, *J. Geophys. Res., 117*, A05207, doi:10.1029/2011JA017262.

Wilder, F. D., S. Eriksson, H. Korth, J. B. H. Baker, M. R. Hairston, C. Heinselman, and B. J. Anderson (2013), Field-aligned current reconfiguration and magnetospheric response to an impulse in the interplanetary magnetic field B_Y component, *Geophys. Res. Lett., 40,* 2489–2494, doi:10.1002/grl.50505.

Wiltberger, M., W. Wang, A. Burns, S. Solomon, J. Lyon, and C. Goodrich (2004), Initial results from the Coupled Magnetosphere-Ionosphere-Thermosphere model: magnetospheric and ionospheric responses, *J. Atmos. Solar-Terr. Phys., 66*, 1411, doi:10.1016/j.jastp.2004.04.026.

Wiltberger, M., R. S. Weigel, W. Lotko, and J. A. Fedder (2009), Modeling seasonal variations of auroral particle precipitation in a global-scale magnetosphere-ionosphere simulation*, J. Geophys. Res.*, *114,* A01204, doi:10.1029/2008JA013108.

Wolf, R. A., R. W. Spiro, S. Sazykin, F. R. Toffoletto (2007), How the Earth's inner magnetosphere works: An evolving picture, *J. Atmos. Solar-Terr. Phys., 69*, 288-302, doi:10.1016/j.jastp.2006.07.026.

Yamazaki, Y., K. Yumoto, T. Uozumi, and M. G. Cardinal (2011), Intensity variations of the equivalent S_q current system along the 210° magnetic meridian, *J. Geophys. Res., 116*(A10308), doi:10.1029/2011JA016632.

Yamazaki, Y., A. D. Richmond, A. Maute, Q. Wu, D. A. Ortland, A. Yoshikawa, I. A. Adimula, B. Rabiu, M. Kunitake, and T. Tsugawa (2014), Ground magnetic effects of the equatorial electrojet simulated by the TIE-GCM driven by TIMED satellite data, *J. Geophys. Res. Space Physics*, *119*, 3150–3161, doi:10.1002/2013JA019487.

Yu, Y., and A. J. Ridley (2008), Validation of the space weather modeling framework using ground-based magnetometers, *Space Weather, 6*, S05002, doi:10.1029/2007SW000345.

Zaka, K. Z., A. T. Kobéa, V. Doumbia, A. D. Richmond, A. Maute, N. M. Mene, O. K. Obrou, J-P. Adohi, P. Assamoi, K. Boka, and C. Amory-Mazaudier (2010), Simulation of electric field and current during the 11 June 1993 disturbance dynamo event: Comparison with the observations, *J. Geophys. Res.*, *115*(A11307), doi:10.1029/2010JA015417.

Zhang, Y., and L. J. Paxton (2008), An empirical Kp-dependent global auroral model based on TIMED/GUVI FUV data, *J. Atmos. Solar-Terr. Phys., 70*(8), 1231-1242, doi:10.1016/j.jastp.2008.03.008.

Zmuda, A. J., J. H. Martin, and F. T. Heuring (1966), Transverse magnetic disturbances at 1100 kilometers in the auroral region, *J. Geophys. Res.*, *71*(21), 5033–5045, doi:10.1029/JZ071i021p05033.

Unpublished Material

Altadill, D., S. Marsal, and E. Blanch (2014), Results of the TIE-GCM and the peak height disturbance models on the occasion of selected magnetically disturbed periods, presented at the *COSPAR Scientific Assembly* held in Moscow, Russia, on August 2-10, 2014, unpublished, available online at: http://www.obsebre.es/images/oeb/pdfs/en/COSPAR-2014-DA-et-al.pdf (accessed on November 13, 2014).

Anderson, B. J., H. Korth, R. J. Barnes, and V. G. Merkin (2013), Active Magnetosphere and Planetary Electrodynamics Response Experiment development status, presented at the *2013 space weather workshop* held in Boulder, CO, USA, on April 16-19, 2013, unpublished, available online at: http://www.swpc.noaa.gov/sww/SWW_2013_Presentations/Tuesday_Afternoon/AMPERE_BrianAnderson_JHUAPL.pptx (accessed on November 13, 2014).

Marsal, S., A. D. Richmond, and A. Maute (2013), Conductivities consistent with FACs in the AMPERE-driven TIE-GCM, presented at the *GEM Mini-Workshop* held in San Francisco, CA, USA, on December 8, 2013, unpublished, available online at: http://ccmc.gsfc.nasa.gov/RoR_WWW/presentations/GEM-CEDAR-2013-mini-GEM-workshop/7_A.Richmond_GEM_Mini-Workshop_Marsal_etal.pdf (accessed on November 13, 2014).

Richmond, A. D., L. Qian, Y. Deng, Y. Huang, E. Cousins, S. Marsal, and B. Emery (2014), Quantification of transient changes of thermospheric neutral density, presented at *AFOSR Space Science Review* held in Albuquerque, NM, USA, on January 13-14, 2014, unpublished, available online at:

https://community.apan.org/afosr/m/kathy/131848/download.aspx (accessed on November 13, 2014).

Cover photo by Joshua Strang (source: US Air Force). Northern Lights above Bear Lake, Alaska